Evaluation of Positron Emission Mammography using plastic scintillator and wavelength shifters

Supervisor:
Prof. Paweł Moskal

Author:
Shivani Shivani

Co-supervisor:
Prof. Elżbieta Łuczyńska

A thesis submitted in fulfilment of the requirements for the degree of Doctor of Philosophy at the Faculty of Physics, Astronomy, and Applied Computer Science

Dedicated to my parents and beloved brother

Wydział Fizyki, Astronomii
i Informatyki Stosowanej
Uniwersytet Jagielloński

Oświadczenie

Ja niżej podpisana Shivani Shivani (nr indeksu: 1142029) doktorantka Wydziału Fizyki, Astronomii i Informatyki Stosowanej Uniwersytetu Jagiellońskiego oświadczam, że przedłożona przeze mnie rozprawa doktorska pt. „Evaluation of Positron Emission Mammography using plastic scintillator and wavelength shifters " jest oryginalna i przedstawia wyniki badań wykonanych przeze mnie osobiście, pod kierunkiem prof. dr hab. Pawła Moskala. Pracę napisałam samodzielnie.

Oświadczam, że moja rozprawa doktorska została opracowana zgodnie z Ustawą o prawie autorskim i prawach pokrewnych z dnia 4 lutego 1994 r. (Dziennik Ustaw 1994 nr 24 poz. 83 wraz z późniejszymi zmianami).

Jestem świadoma, że niezgodność niniejszego oświadczenia z prawdą ujawniona w dowolnym czasie, niezależnie od skutków prawnych wynikających z ww. ustawy, może spowodować unieważnienie stopnia nabytego na podstawie tej rozprawy.

Kraków, dnia ....

....
podpis doktorantki

Abstract

Marian Smoluchowski Institute of Physics

Doctor of Philosophy

Evaluation of Positron Emission Mammography using plastic scintillator and wavelength shifters

by Shivani SHIVANI

Breast cancer remains a significant health concern globally, necessitating continuous advancements in diagnostic technologies to improve early detection and treatment outcomes. This thesis focuses on developing a new detector for breast cancer diagnosis based on Positron Emission Mammography (PEM) technology. This research is driven by the shortcomings observed in conventional imaging modalities such as mammography, ultrasound, and MRI, which may demonstrate inadequate sensitivity, specificity, or imaging speed. These limitations can result in missed detections, false positives, or delays in diagnosis, which can significantly impact patient outcomes and lead to unnecessary biopsies. The aim is to address the existing limitations in current breast imaging modalities by leveraging the unique capabilities offered by PEM.

The thesis involves a study to analyze the data from hospitals to compare the sensitivity, specificity, and AUC (Area under the curve) values for mammography, ultrasound, and MRI to evaluate the performance of each imaging modality in detecting breast cancer. Higher sensitivity and specificity values indicate better performance, while a higher AUC indicates a better overall classifier performance. This information provided a baseline for understanding the current state-of-the-art and the room for improvement in developing a new detector called Jagiellonian Positron emission mammography (J-PEM).

The thesis aims to design and construct a specialized J-PEM detector system optimized for breast imaging, which includes advancements in detector materials, plastic scintillators, wavelength shifters, and photodetectors. This prototype system consists of a single module, built from two layers of plastic scintillators (6x24x500 mm^3) and one layer of wavelength shifters (3x10x100 mm^3) placed orthogonally between them. Each scintillator bar is connected at both ends to Silicon Photomultipliers for the signal readout. This 3D system is based on the novel idea of applying plastic scintillators to detect annihilation photons and improve spatial resolution by utilization of wavelength shifters (WLS).

The research findings presented in this thesis highlight the achievement of a spatial resolution (FWHM) of approximately 5 mm validated by both GATE simulation

studies and experimental analyses. Significantly, the achieved spatial resolution is equivalent to that of other established imaging modalities, despite the utilization of the single-head J-PEM module. These results demonstrate the effectiveness and cost-efficiency of the J-PEM system as a tool for breast cancer detection, offering enhanced spatial resolution and operational efficiency. The reconstructed images presented in this study were generated exclusively through simulation using two module detectors. However, it should be noted that in the actual experimental setup, only a single module was constructed, and the acquisition of images will be part of future development and investigation. An additional study for opting for WLS with and without optical separation suggests that employing WLS without optical separation yields superior resolution compared to the alternative. The J-PEM has also been developed with an innovative addition known as DOI sensitivity, which reveals that despite its relatively modest sensitivity, introducing narrower WLS in future advancements has the potential to enhance its performance.

While the outcomes of this research are promising, further investigations and advancements are necessary to evaluate the clinical utility and potential impact of the J-PEM system on breast cancer diagnosis and treatment.

Streszczenie

Rak piersi pozostaje poważnym problemem zdrowotnym na całym świecie, wymagającym ciągłego rozwoju technologii diagnostycznych w celu poprawy jego wczesnego wykrywania i skutków leczenia. Przedstawiona praca dyplomowa koncentruje się na opracowaniu nowego detektora do diagnostyki raka piersi w oparciu o technologię pozytonowej mammografii emisyjnej (PEM).

Badania te są motywowane ograniczeniami obserwowanymi w konwencjonalnych metodach obrazowania, takich jak mammografia, USG i MRI, które mogą wykazywać niewystarczającą czułość, swoistość lub szybkość obrazowania. Ograniczenia te mogą powodować nierozpoznanie guza, fałszywie dodatnie wyniki lub opóźnienia w diagnozie, co może znacząco wpłynąć na wynik leczenia pacjentów i prowadzić do niepotrzebnych biopsji. Celem badań jest wyeliminowanie istniejących ograniczeń w obecnych metodach obrazowania piersi poprzez wykorzystanie unikalnych możliwości oferowanych przez PEM. Praca obejmuje badanie mające na celu analizę danych ze szpitali w celu porównania czułości, swoistości i wartości AUC (pole pod krzywą) dla mammografii, ultrasonografii i MRI celem oceny wydajności każdej metody obrazowania w wykrywaniu raka piersi. Wyższe wartości czułości i specyficzności wskazują na lepszą wydajność, podczas gdy wyższa wartość AUC wskazuje na lepszą ogólną wydajność klasyfikatora. Informacje te zapewniły punkt odniesienia dla zrozumienia aktualnego stanu wiedzy i możliwości ulepszeń przy opracowaniu nowego detektora o nazwie Jagielloński Pozytonowy Mammograf Emisyjny (J-PEM).

Prezentowana rozprawa opisuje również projektowanie oraz wykonanie specjalistycznego systemu detektorów J-PEM zoptymalizowanego do obrazowania piersi, który bazuje na plastikowych scyntylatorach, przesuwaczach długości fal i fotodetektorach. Ten prototypowy system składa się z pojedynczego modułu, zbudowanego z dwóch warstw plastikowych scyntylatorów (6x24x500 mm^3) i jednej warstwy przesuwaczy długości fali (3x10x100 mm^3) umieszczonych ortogonalnie pomiędzy nimi. Do każdego paska scyntylacyjnego, na obu jego końcach, są przymocowane fotopowielacze krzemowe w celu odczytu sygnału. Ten system 3D opiera się na nowatorskim pomyśle zastosowania plastikowych scyntylatorów do wykrywania fotonów anihilacji i poprawy rozdzielczości przestrzennej poprzez wykorzystanie przesuwaczy długości fal (WLS). Wyniki badań przedstawione w pracy wykazały osiągnięcie rozdzielczości przestrzennej (FWHM) równej około 5 mm, potwierdzonej zarówno badaniami symulacyjnymi oprogramowaniem GATE, jak i analizami eksperymentalnymi. Co istotne, osiągnięta rozdzielczość przestrzenna jest porównywalna z pozostałymi metodami obrazowania, pomimo wykorzystania jednogłowicowego modułu J-PEM. Wyniki te pokazują skuteczność i opłacalność systemu J-PEM jako narzędzia do wykrywania raka piersi, oferującego zwiększoną rozdzielczość przestrzenną i wydajność detekcji. Zrekonstruowane obrazy przedstawione w tej rozprawie zostały

wygenerowane wyłącznie poprzez symulacje przy użyciu dwóch detektorów modułowych. Należy jednak zauważyć, że w rzeczywistej konfiguracji eksperymentalnej skonstruowano tylko jeden moduł, a pozyskiwanie obrazów będzie częścią przyszłego rozwoju i badań. Dodatkowe badanie dotyczące wyboru WLS z separacją optyczną i bez separacji optycznej sugeruje, że zastosowanie WLS bez separacji optycznej zapewnia lepszą rozdzielczość w porównaniu z alternatywą. J-PEM został również skonstruowany z innowacyjnym dodatkiem znanym jako czułość DOI, który pokazuje, że pomimo jego stosunkowo skromnej czułości, wprowadzenie w kolejnych modyfikacjach węższych WLS może potencjalnie poprawić jego wydajność.

Chociaż wyniki tych badań są obiecujące, konieczne są dalsze badania i rozwój, aby ocenić użyteczność kliniczną i potencjalny wpływ systemu J-PEM na diagnostykę i leczenie raka piersi.

Acknowledgments

Contents

List of Figures

List of Tables

Chapter 1

Introduction

A recent demonstration has showcased the potential utilization of plastic scintillators in the development of cost-effective positron emission tomography (PET) scanners [1, 2, 3, 4, 5, 6, 7]. The main focus of this thesis is to prove the hypothesis that the use of plastic scintillators in positron emission mammography (PEM) is a viable approach. The aim is to develop a system that can offer both cost-effectiveness and high specificity in detecting breast cancer.

Breast cancer is the most commonly diagnosed cancer in women in a vast majority of countries (140 out of 184), comprising one-quarter of all cancers diagnosed in women [8]. It is also the leading cause of cancer-related deaths in women [9]. Although breast cancer was once believed to be prevalent mainly in Western women, it now affects more than half of new cases (52%) and 62% of deaths in developing countries [10]. Breast cancer is a form of cancer that arises in the tissue of the breast, frequently beginning in the cells lining the milk ducts or in the glandular tissue that makes milk. While breast cancer is relatively rare in men, it remains one of the most prevalent forms of cancer among women. The exact cause of breast cancer is yet to be fully understood, but it is widely believed to be influenced by a combination of genetic, environmental, and lifestyle factors. Age, family history, hormonal fluctuations, exposure to radiation or harmful substances, and various other factors can significantly increase an individual's susceptibility to developing breast cancer. However, only 5-10% of cancers are caused by an inherited abnormality from the parents. At the same time, genetic abnormalities cause 85-90% of breast cancers due to ageing. A lump or thickening in the breast or underarm, changes in breast size or form, skin dimpling, nipple discharge, or a nipple that bends inward are all symptoms of breast cancer. However, some breast cancer patients may not exhibit any symptoms at all. Therefore, it is recommended to have regular mammograms, as recommended to become familiar with the typical appearance of one's breasts. Therefore, medical imaging holds significant importance in the screening of breast cancer, as it aids in the classification and evaluation of ambiguous breast abnormalities and provides valuable information regarding tumor size. Furthermore, medical imaging plays a crucial role in assessing the effectiveness of treatment interventions. As a result, imaging via various methods, including mammography, ultrasound, MRI, and biopsy, is a critical, life-long component for patients with breast cancer, from initial diagnosis to disease progression. The timely detection and prompt treatment of breast cancer play a vital role in enhancing survival rates and reducing the likelihood of adverse outcomes.

These screening tests are evaluated based on their interpreting performance, determined by various measures such as sensitivity, specificity, positive predictive value, and cancer stage at diagnosis [11]. Sensitivity and specificity are key terms that describe a test's strengths and limitations [12]. Sensitivity refers to the likelihood of a positive test result in individuals with the disease, indicating the test's ability to detect the condition [12]. On the other hand, specificity describes the likelihood of a negative test result in healthy individuals, showing the test's capacity to rule out the disease. The positive predictive value is the risk of developing invasive cancer when a patient is recalled for evaluation, calculated by dividing true positive cases by the sum of true positive and false positive cases [12]. A highly sensitive test for breast cancer detection can accurately identify a large proportion of individuals with the disease, minimizing the number of false negatives and ensuring that fewer cases go undetected. On the other hand, a highly specific test can accurately identify an individual who does not have a disease, reducing the number of false positives and preventing unnecessary treatments or interventions. Depending on the detection technique, 20-25% of women may be incorrectly diagnosed with cancer, resulting in unnecessary biopsies [13, 14]. Since breast lesions can be microscopic, measuring only a few millimetres in diameter, a detection system with high sensitivity and spatial resolution is essential.

Mammography, ultrasound, and MRI are widely used imaging techniques for breast cancer detection. Mammography is the most commonly used method, which involves low-dose X-rays to produce images of the breast tissue. However, mammography has limited sensitivity in women with dense breast tissue, making distinguishing between cancerous and normal tissue difficult. Furthermore, mammography may lead to false positive results, resulting in unnecessary biopsies and anxiety for the patient. In such cases, it requires a patient to go for another imaging technology that employs ultrasound waves to produce images of breast tissue. Ultrasound helps distinguish between solid and fluid-filled lumps in the breast. However, ultrasound has limited sensitivity in detecting small cancers and is operator-dependent, meaning that the quality of the images can vary based on the technician's skill. Therefore, to generate precise images of breast tissue, MRI is used as its highly sensitive imaging technique that utilizes magnetic fields and radio waves. MRI is beneficial in detecting small tumors and in patients with dense breast tissue. However, MRI is expensive, time-consuming, and requires the use of contrast agents, which can be harmful to some patients. Nonetheless, the sensitivity of current imaging modalities such as Mammography, ultrasound, and MRI are compromised when detecting breast cancer in thick breasts, making it difficult to distinguish between the tumor and normal tissues.

In addition to these methods, PET technology is emerging as a promising tool for breast cancer imaging, capable of detecting small lesions and providing information on cancerous tissue's metabolic activity. It's a functional imaging method that maps the distribution of a radio-labelled tracer in the body to visualize cellular metabolism and identify malignant tissues. FDG (fluorodeoxyglucose), a glucose analogue that highly metabolic cancer cells absorb, is commonly used as the radio-labelled tracer in PET imaging for breast cancer detection. PET imaging, compared to mammography, ultrasound, and MRI, can detect small breast lesions that may not be visible with these methods and provide information on cancer's metabolic activity, which can aid in determining its stage and aggressiveness. However, PET scanners

are primarily designed for whole-torso and brain imaging, and their detectors are positioned farther away from the breasts [15]. This can lead to decreased sensitivity and compromised image quality, specifically for breast imaging. It also has limited spatial resolution, which can reduce accuracy in identifying small lesions or precisely localizing their positions within the breast tissue. Because of these given reasons, a specialized breast imaging modality called Positron Emission Mammography (PEM) is specifically designed for breast cancer detection using PET technology. PEM has higher spatial resolution [16] and sensitivity than PET and higher specificity than MRI, reducing the number of unnecessary biopsies. PEM's increased sensitivity may be due to its superior spatial resolution, allowing it to detect small lesions [17]. Table 1.1 provides a comprehensive comparison of the sensitivity and specificity values for Positron Emission Mammography (PEM) and other imaging modalities.

Table 1.1: Comparison between the sensitivity and specificity of Mammography, Ultrasound, MRI, PET/CT or PET/MR and PEM. [18, 19, 20, 21, 22, 16, 23]

Parameter	Mammography	Ultrasound	MRI	PET/CT or PET/MR	PEM
Sensitivity	72% to 83%	61% to 89%	79% to 93%	88% to 96 %	90% to 91%
Specificity	47% to 96%	49% to 87%	85% to 92%	83% to 91%	86% to 93%

The limited availability and accessibility of PEM technology compared to established imaging modalities such as mammography and MRI, along with the associated high costs of equipment acquisition and maintenance, as well as the need for specialized training and expertise, hinder its widespread adoption in healthcare facilities. Mammography, with its long-standing history, established protocols, and proven effectiveness, remains the standard imaging technique for breast cancer screening. Additionally, other modalities like MRI and ultrasound have well-defined roles in breast cancer diagnosis and monitoring. These prevailing practices present challenges to the integration and acceptance of PEM as a routine clinical tool. PEM technology is relatively new compared to other imaging modalities, necessitating ongoing research and development efforts to enhance its capabilities, optimize imaging protocols, and establish its clinical value. As an emerging technology, it requires time for research studies to accumulate and provide evidence regarding the effectiveness and utility of PEM in detecting breast cancer.

The primary goal of this thesis is to investigate and fabricate a novel Positron Emission Mammography (PEM) detector that mitigates the limitations found in current scanning systems. To achieve this objective, a prototype called J-PEM was developed, which utilizes plastic scintillators and wavelength-shifting (WLS) technology for the detection and diagnosis of breast cancer. Plastic scintillators serve as the fundamental component in the development of the cost-effective Jagiellonian positron emission tomography (J-PET) system [1, 2, 3, 4, 5, 6]. Similarly, in line with this analogy, the abbreviation J-PEM refers to the Jagiellonian positron emission mammography, which utilizes plastic scintillators for the efficient detection of breast cancer.

J-PEM is a positron emission tomography (PET) technology-based prototype designed specifically to detect photons resulting from electron-positron annihilation, with an energy of approximately 511 keV [1, 2]. The prototype consists of two

parallel photon detectors arranged in a configuration similar to mammography compressors. Each detector module comprises two layers of plastic scintillator material, with WLS strips positioned orthogonally between them. Silicon photo-multipliers are connected to both ends of each scintillator bar to facilitate signal readout [1]. By combining plastic scintillators with superior timing properties and WLS strips, the prototype offers a precise and cost-effective scanner with enhanced spatial resolution and efficiency for the detection of breast cancer [24, 25]. The localization of photon interaction is determined by measuring the arrival time of signals at the ends of the elongated scintillator strips. Notably, J-PEM enables simultaneous imaging of the density distribution of annihilation points and positron annihilation lifetime spectroscopy [26, 27].

The main objectives of constructing the J-PEM detector for detecting breast cancer are as follows:

- To improve the specificity and sensitivity of the detection process, thereby enabling quicker and more precise diagnosis of the disease. This new detector is built using innovative design concepts and scintillating materials that offer the potential for improved spatial resolution and image quality compared to current PEM detectors.

- Moreover, the new detector is expected to be more economical and simpler to operate in clinical settings. Ultimately, this research aims to enhance the likelihood of successful treatment and improved patient outcomes for individuals diagnosed with breast cancer and reduce biopsies.

To accomplish this objective, the following steps need to be undertaken:

- Investigate the parameters of currently employed methods, including specificity and sensitivity, using patient data obtained from the hospital. This analysis aims to examine and evaluate the performance of the existing techniques based on real patient data.

- Develop a novel J-PEM detector design: Utilizing insights obtained from the literature review, design a new and innovative Positron Emission Mammography (PEM) detector. Consider various aspects such as the choice of detector materials, configuration, photon detection techniques, and methods for signal readout.

- Simulation studies were conducted to optimize the detector geometry and reconstruct images for the double-head J-PEM module. The purpose of these simulations was to refine the configuration of the detector in order to improve its performance and achieve optimal image quality.

- Construct a functional prototype: Once the design is finalized, proceed with constructing a single module prototype for the PEM detector. This stage involves procuring the necessary materials, components, and equipment required for the assembly process. Ensure the incorporation of plastic scintillators and wavelength-shifting (WLS) technology within the detector design to enhance spatial resolution, efficiency, and cost-effectiveness in breast cancer detection.

- Data taken to establish the characteristic performance and development of methods for calibrating, reconstructing hit positions and depth of interaction sensitivity of J-PEM.

- Perform comprehensive testing and validation: Conduct rigorous testing and validation procedures for the constructed J-PEM detector prototype. This includes evaluating its spatial resolution (hit positions) and overall performance in detecting and diagnosing breast cancer.

- Two possibilities were tested in the evaluation: using wavelength shifting (WLS) with optical separation and WLS without optical separation.

It is important to acknowledge that the reconstructed images showcased in this study were generated solely through simulation using two module detectors. However, it is crucial to recognize that the practical implementation of the experimental setup involved the construction of only a single module. The acquisition of actual images using this setup will be a part of forthcoming development and further investigation.

The study on the predetermined objectives is described, and the findings are provided in the chapters, which are organized as follows. In **Chapter 2**, a comprehensive review of previous research on breast cancer diagnosis and screening methods is presented. The significance of breast cancer diagnosis and screening methods is emphasized, and their limitations are discussed. In **Chapter 3**, the methods and materials used for the analysis of medical data from the hospital are presented. The aim was to extract the sensitivity and specificity values of commercially available scanners used for breast cancer detection. The methods used for the analysis are described in detail, including the selection criteria for the patients, the imaging techniques used, and the statistical methods applied to extract the required values. **Chapter 4** presents an in-depth explanation of the construction and design process of a single-head J-PEM module that incorporates a unique concept employing a plastic scintillator and WLS. This chapter also provides a comprehensive overview of the J-PEM prototype and its constituent components. **Chapter 5** of the thesis focuses on using Monte Carlo simulations to optimize the detector's performance and reconstruction of images for a double-head J-PEM module. The chapter provides a detailed description of the simulation methods and materials used in the study, as well as the results obtained from the simulations. **Chapter 6** provides a detailed account of the experimental setup used for data acquisition, including calibration methods and the measurements performed. The chapter also presents the spatial resolution results obtained from the prototype and concludes with an overview of the findings. **Chapter 7** comprises the conclusion of the thesis and perspective.

Author Contribution:

The author played a crucial role in the study, starting from the conception and design phase. I have actively contributed to formulating research questions and objectives. Additionally, the author conducted an extensive literature review to gather relevant information.

The author undertook the construction and testing of the complete detector system. With the assistance of a technician, we successfully assembled the detector, which featured three layers. These layers included a 32-layer plastic scintillator with dimension $6 \times 24 \times 500$ mm^3 and a 40-layer wavelength shifter with size $3 \times 10 \times 100$ mm^3. For readout mounting and testing, SiPMs (Silicon Photo-multipliers) measuring 6,6 mm were employed. A total of 272 SiPMs were meticulously tested and utilized for the readout process from both the plastic scintillator and the wavelength shifter layers.

The author played a crucial role in developing and implementing the research methodology, which involved designing data collection procedures and selecting appropriate data analysis techniques. The author took charge of the data collection process and conducted a careful analysis of the collected data. Additionally, the author took the responsibility of interpreting the findings and drawing meaningful conclusions based on the results obtained.

In addition to these responsibilities, the author independently conducted GATE simulations using the pre-existing Castor software. The author was responsible for designing and setting up the simulation parameters and input conditions based on the specific requirements of the study. And also ensure the accuracy and validity of the simulation model by incorporating relevant physics models, materials, and geometry. Moreover, the author utilized the Castor software to analyze the output generated from the Gate simulation for image reconstruction. The author meticulously examined various output parameters obtained from the simulation and compared them with experimental data.

The author's extensive engagement throughout all stages of the research, including the design phase and data analysis, underscores their notable contribution and commitment to the study. Their comprehensive involvement exemplifies their substantial role in the research project.

Chapter 2

State of the art in Breast Cancer Diagnosis

2.1 Breast Cancer epidemology

According to statistics provided by reference, [28], female breast cancer is the leading form of cancer globally, accounting for 11.7% of all cases. It is followed by lung cancer (11.4%), colorectal cancer (10.0%), prostate cancer (7.3%), and stomach cancer (5.6%). In 2020, breast cancer affected approximately 2.3 million women worldwide, resulting in 685,000 fatalities. It is worth noting that breast cancer was the most frequently diagnosed disease, with 7.8 million women diagnosed within the previous five years [29]. Breast cancer causes a significant burden in terms of disability-adjusted life years (DALYs) among women worldwide, surpassing all other types of cancer. It can affect women at any age following puberty, and the incidence rates tend to increase with age. Figure 2.1 and Figure 2.2 illustrate the top ten cancer types worldwide for women, considering both estimated cases and deaths.

Approximately half of all breast cancer cases occur in women who do not exhibit any known risk factors other than being female and over 40. However, several factors can increase the risk of developing breast cancer, including age, obesity, excessive alcohol consumption, family history of breast cancer, history of radiation exposure, reproductive history (such as age at first menstrual period and age at first pregnancy), cigarette use, and postmenopausal hormone treatment. Despite addressing all potentially modifiable risk factors, the reduction in the likelihood of developing breast cancer would only be around 30% [29]. However, it is important to note that most women diagnosed with breast cancer do not have a known family history. The absence of a family history does not necessarily indicate a lower risk. Certain hereditary "high penetrance" gene mutations, such as mutations in the BRCA1, BRCA2, and PALB-2 genes, significantly increase the risk of breast cancer. Women with these mutations may consider risk-reduction strategies, including prophylactic bilateral mastectomy. However, the decision to undergo such an invasive procedure should be carefully evaluated and weighed against other available options, as it only applies to a small percentage of women [29]. Hence, efforts are being made to reduce breast cancer mortality rates by emphasizing early detection. It is widely recognized that the survival rate of cancer patients is closely linked to the stage at which the disease is detected. Therefore, early detection is crucial, as it allows for more effective treatment options compared to later stages of the disease, which are often
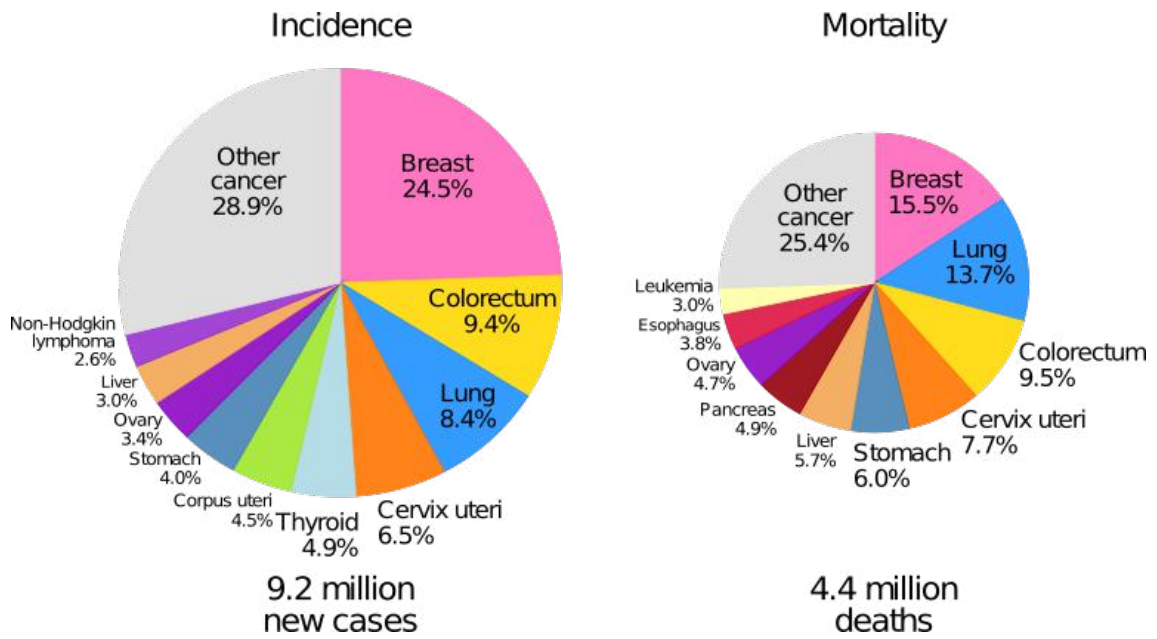
Figure 2.1: Distribution of Cases and Deaths for the Top 10 Most Common Cancers in 2020 for Women. For women, the area of the pie chart reflects the proportion of the total number of cases or deaths; nonmelanoma skin cancers (excluding basal cell carcinoma for incidence) are included in the "other" category. Source: GLOBOCAN 2020 [28].
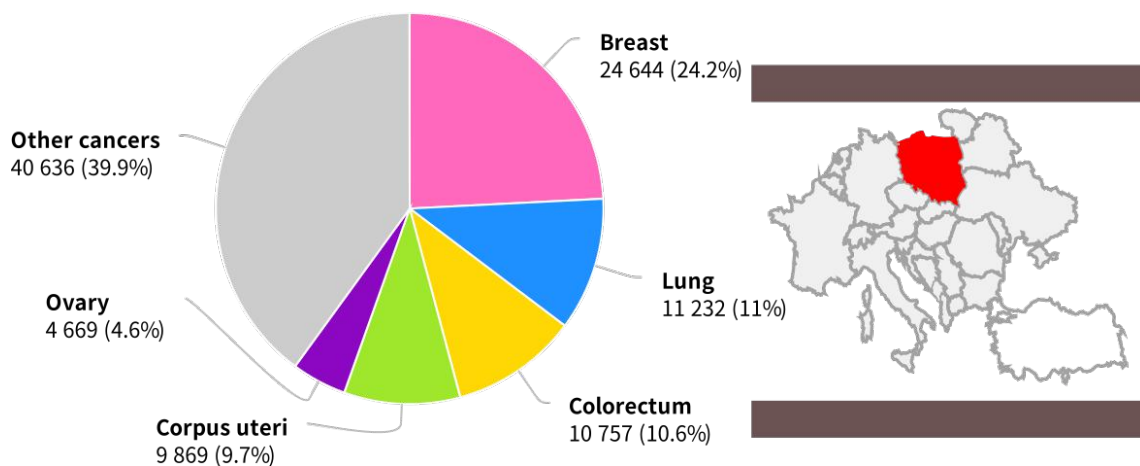
Figure 2.2: Number of new cases in 2020 in Poland, females, all ages. Country-specific data source: Cracow City and District Cancer Registry, Greater Poland Cancer Registry, Kielce Regional Cancer Registry, Lower Silesian Cancer Registry, Lublin Cancer Registry, Podkarpackie Cancer Registry. Method estimated from national mortality estimates by modelling, using mortality: incidence ratios derived from country-specific cancer registry data. Source: GLOBOCAN 2020 [30].

more challenging to treat [29]. There was a study which shows that from the 1930s to the 1970s, breast cancer mortality rates remained relatively stable [29]. However, in the 1980s, improvements in survival rates were observed in countries where early detection programs were implemented alongside diverse treatment options to combat advanced stages of the disease.

2.2 Diagnostic Imaging Modalities for Breast Cancer

Breast cancer screening refers to the process of assessing a woman's breasts for cancer before any signs or symptoms of the disease become apparent. The primary objective of breast cancer screening is to reduce mortality associated with breast cancer [31]. It is essential for a woman to consult her healthcare provider to determine the most suitable screening options for her. While breast cancer screening cannot prevent the disease, it plays a crucial role in early detection when the disease is more manageable. Mammography is a fundamental imaging technique employed for breast cancer detection. It can be used both as a screening tool and as a diagnostic examination for individuals presenting clinical symptoms. Screening mammography aims to detect clinically asymptomatic breast cancer and is typically recommended for women aged 50 to 69 years every two years in Poland. However, the age range and frequency of screening mammography may vary across countries based on individual financial considerations and healthcare policies. In some countries, screening mammography is conducted among women aged 40 or 50 years, and the upper age limit may vary, extending to 74 or 75 years. Screening mammography allows for detecting tumors before they can be felt during a physical examination, including intraductal cancer [32], which can manifest as microcalcifications that may not be visible on other imaging modalities such as ultrasound or breast MRI. However, mammography has certain limitations. One of these limitations is related to dense glandular breast tissue, where both tumors and dense breast tissue appear as white areas on a mammogram. The sensitivity of mammography is influenced by breast tissue anatomy, the expertise of the interpreting physician, and the proper positioning of the patient during the examination. To mitigate the challenges associated with evaluating screening mammography, many countries employ two independent readers to interpret each case. The sensitivity of mammography varies between 80% and 96%, while specificity ranges from 15% to 51.8% [33].

Clinical mammography, on the other hand, is performed in symptomatic women who present with palpable breast lesions or nipple discharge. It may be conducted in women over the age of 25.

As a consequence of mammography limitations, new diagnostic methods based on mammography, such as tomosynthesis or contrast-enhanced mammography (CEM), have been developed. In Poland, CEM after iodine contrast medium administration has been performed since 2010. A dedicated dual-energy device needs to be employed to perform this examination. Two minutes before the mammography examination, a contrast medium in the amount of 1.5 ml/kg of body weight is administered at the speed of 3 ml/s. After contrast injection, a regular mammography examination is started. Low-energy images, which are comparable with digital mammography 2D images and subtraction images, appear on diagnostic monitors. They show pathological foci of contrast enhancement. This examination enables local staging of the neoplastic process and assessment of multifocality, multicentricity and intraductal components. It also allows for tumor presence exclusion. Currently, its diagnostic efficiency is comparable to breast MRI. CEM limitation is the lack of possibility to be performed in women with breast implants, as an implant may overlap a contrast enhancement focus or lesions localized deep and close to the chest wall may be overlooked. It is also important to remember that the radiation dose per patient is 15%–
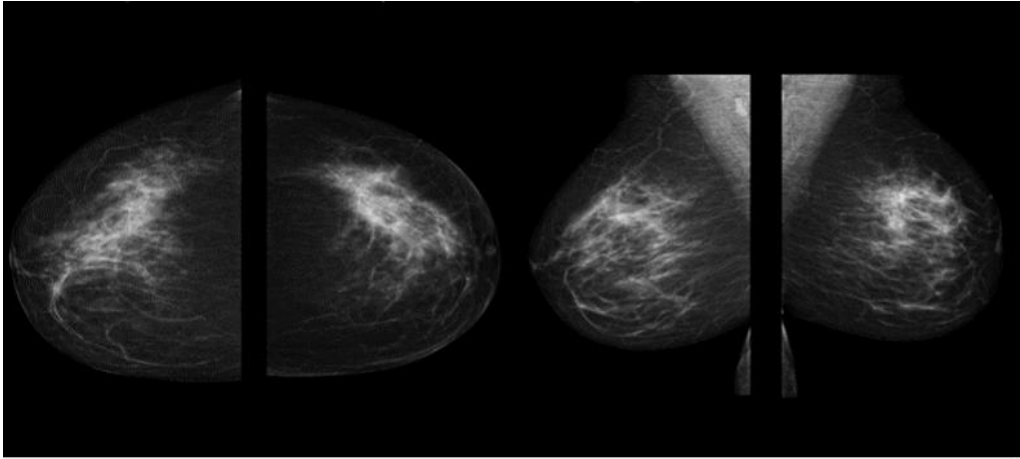
Figure 2.3: Example of mammography images. Patient 42 y.o. Heterogenous fatty-glandular breast anatomy type. In the left breast in the upper outer quadrant, architectural distortion of parenchyma in the area of about 7 cm. On mammography Breast Imaging-Reporting and Data System (BI-RADS) V. Examination performed in Breast Diagnostic Imaging Unit, Diagnostic Imaging Department, University Hospital in Cracow (Pracownia Diagnostyki Obrazowej Piersi Zakładu Diagnostyki Obrazowej Nowego szpitala Uniwersyteckiego w Krakowie).

20% higher than in digital mammography. Figure 2.4 presents subtraction images in spectral mammography.
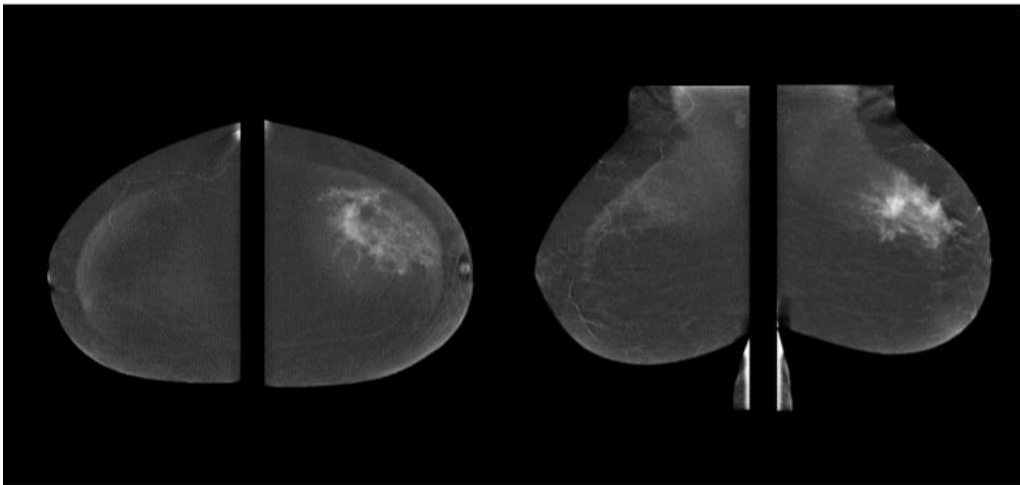
Figure 2.4: Patient 42 y.o., the same patient whose digital mammography images are presented Figure 2.3. On CEM, it is possible to evaluate the neoplastic process extent. In the left breast extended area of contrast and enhancement covers almost the entire upper outer quadrant. No suspicious lesions in the right breast. Breast Imaging-Reporting and Data System (BI-RADS) V. Examination performed in Breast Diagnostic Imaging Unit, Diagnostic Imaging Department, University Hospital in Cracow (Pracownia Diagnostyki Obrazowej Piersi Zakładu Diagnostyki Obrazowej Nowego szpitala Uniwersyteckiego w Krakowie).

Ultrasound is another diagnostic method in breast cancer diagnostics. It is widely accepted as the most useful adjunct to mammography for diagnosing breast abnormalities. Ultrasound is most often used to assess palpable masses and is excellent

for the evaluation of non-palpable masses that have been detected during screening mammography [34, 35]. In some cases, ultrasound may demonstrate malignancies and other masses that are mammographically not visible [36].

Figure 2.5: Breast cancer on ultrasound. Patient 67 y.o. Poorly circumscribed hypoechogenic area in the left breast in the retro areolar region. The lesion is poorly visible on mammography. In the left breast increased saturation of glandular tissue in the retroareolar area. Examination performed in Breast Diagnostic Imaging Unit, Diagnostic Imaging Department, University Hospital in Cracow (Pracownia Diagnostyki Obrazowej Piersi Zakładu Diagnostyki Obrazowej Nowego szpitala Uniwersyteckiego w Krakowie.

It may be applied in women of any age; however, in women after 40 years of life, ultrasound should be performed as a complementary examination to mammography. In young women 35-40 years old, ultrasound is a primary diagnostic method. Ultrasound is beneficial to guide all types of biopsies due to easy access to the patient. Nevertheless, ultrasound also has its limitations. Firstly, it is a time-consuming examination. Secondly, in women with fatty breast anatomy, cancer may be overlooked, as well as lesions situated deep, close to the chest wall. Also, in women with heterogenous glandular-fatty breasts, suspicious lesions may be overlooked. Assessment of microcalcifications is difficult, particularly for small clusters of microcalcifications. Another limitation is the lack of an unequivocal sharp border between normal and pathological conditions, resulting in the detection of a large number of benign lesions which require further histopathological verification. Ultrasound had an overall pooled sensitivity and specificity of 80.1% and 88.4%, respectively [33]. An example of an ultrasound image is shown in Figure 2.5.

Magnetic resonance imaging (MRI) has been used as an adjunctive screening tool, mainly for women who may be at increased risk of developing breast cancer. Contrary to mammography and ultrasound, diagnosis on MRI does not depend on breast anatomy type. The sensitivity of MRI in invasive cancer diagnostics is 94 – 99% and 50-80% in non-invasive cancer diagnostics. Specificity ranges from 65-79%. Primary indications for MRI in breast diagnostics are searching for a primary focus in women with enlarged lymph nodes who did not have focal lesions detected on mammography or ultrasound; neoplastic process extent evaluation, particularly in women with verified lobular breast cancer; screening examination in women with BRCA1 and BRCA2 gene mutation; implants assessment and monitoring of neoad-
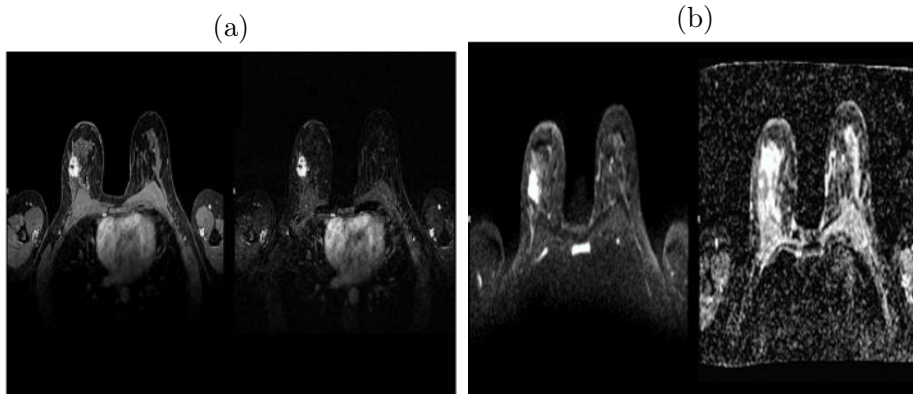
Figure 2.6: Example of MRI image of a patient 50 y.o. T1 and T1-weighted images after dynamics contrast administration ((a)left and (a) right), Diffusion-weighted imaging (DWI) and apparent diffusion coefficient (ADC) ((b)left and (b) right). In the right breast, poorly circumscribed contrast enhancement focus with limited diffusion features confirms the malignancy of the lesion. On histopathology invasive ductal cancer G3 and DCIS. Examination performed in Breast Diagnostic Imaging Unit, Diagnostic Imaging Department, University Hospital in Cracow (Pracownia Diagnostyki Obrazowej Piersi Zakładu Diagnostyki Obrazowej Nowego szpitala Uniwersyteckiego w Krakowie).

juvant therapy. It is necessary to administer a gadolinium contrast medium with an automatic syringe in order to detect cancer. MRI without contrast administration has no diagnostic value. The examination lasts longer than mammography or ultrasound. Another limitation is the fact that on MRI, not only malignant lesions enhance, but also benign ones. To increase the sensitivity and specificity of the method, diffusion maps are created. An of MRI image example is shown in Figure 2.6.

Positron emission mammography PEM is a new technology that is designed for the PET imaging of specific small body parts. To achieve high resolution, it uses short-lived positron-emitting isotopes to generate images of cancer within the breast [16, 17]. At present, this examination is performed if metastasis is suspected in patients with diagnosed breast cancer or in patients with metastasis who are suspicious of having a primary focus localized in their breast. Due to the fact that PET is an expensive procedure, it is only performed in special cases of patients diagnosed with breast cancer. The case presented in Figure 2.7 illustrates such a situation. A patient 42 y.o. examined due to a palpable mass presence in her right breast. On clinical examination in the right breast at the 3 o'clock position a palpable, slightly painful, quite well-circumscribed resistance about 3 cm in diameter. On ultrasound at the above location is a visible irregular hypoechogenic area of about 30x11x18 mm^3 with fluid patches and microcalcifications. In the right axilla, lymph nodes up to 16 mm, as shown in Figure 2.7. On mammography, on the border between upper quadrants, a poorly circumscribed tumor with a diameter of approximately 40 mm and spicules extending from the tumor to the nipple are visible. In the projection of the spicules, microcalcifications within the area of about 7 cm are also visible. Moreover, a marked skin thickening up to 7 – 8 mm of the right breast and enhanced parenchyma pattern in the whole breast proves a highly advanced neoplastic
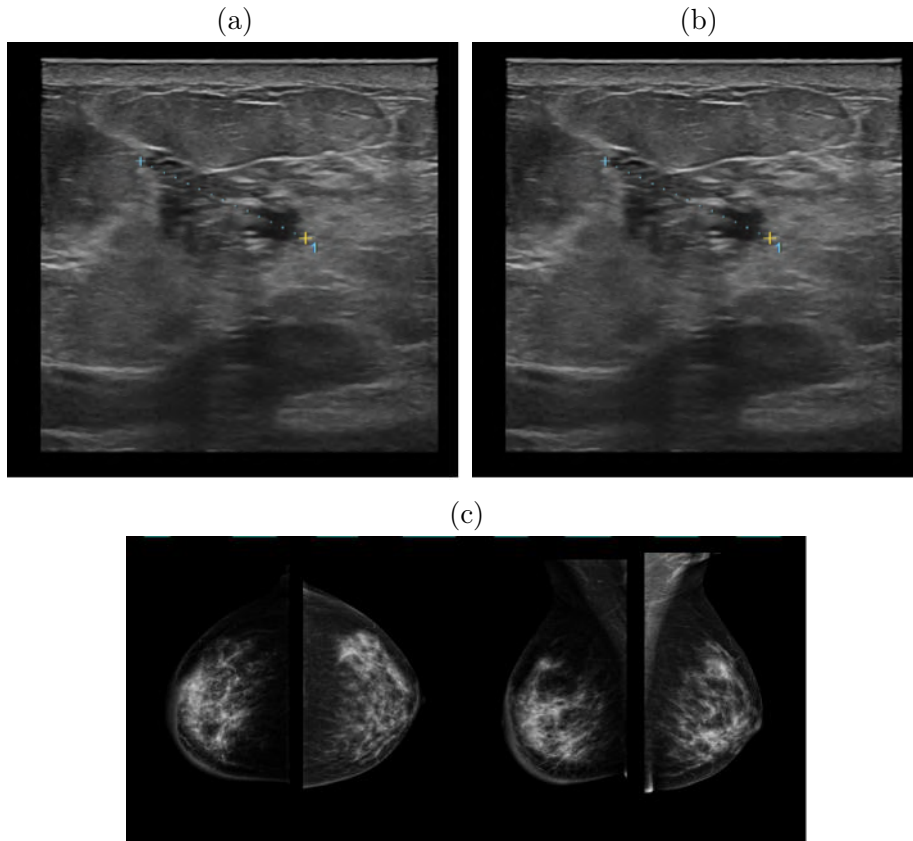
Figure 2.7: (a) Ultrasound image of a patient with a breast tumor at the 12 o'clock position, a solid-liquid lesion. (b) suspicious lymph node in the right axilla. (c) on mammography glandular-fatty breast with the predominance of glandular tissue (ACR C). There is a significant finding of a large tumor with microcalcifications, measuring approximately 11 cm in size. The affected breast also shows thickening of the skin and an increased enhancement of the parenchymal pattern. A notable difference in tumor size is observed between the mammography and ultrasound examinations. The histopathology report confirms the presence of invasive ductal cancer G2 and ductal carcinoma in situ (DCIS). Examination performed in Breast Diagnostic Imaging Unit, Diagnostic Imaging Department, University Hospital in Cracow (Pracownia Diagnostyki Obrazowej Piersi Zakładu Diagnostyki Obrazowej Nowego szpitala Uniwersyteckiego w Krakowie).

process taking place in the breast. Ultrasound and mammography are presented in Figure 2.7.

Due to the tumor's size on mammography, the patient was referred for MRI. The MRI image is presented in Figure 2.8.

The patient was referred for PET/CT examination in order to exclude metastasis. This examination is presented in Figure 2.9.

In conclusion, the diagnosis and evaluation of breast cancer rely on various imaging modalities that play critical roles in detecting, characterizing, and staging the disease. Mammography remains the gold standard for breast cancer screening, while ultrasound and MRI offer additional information to evaluate suspicious findings further. PET imaging provides functional and metabolic information, aiding in staging and treatment response assessment. Each modality has its strengths and limitations,
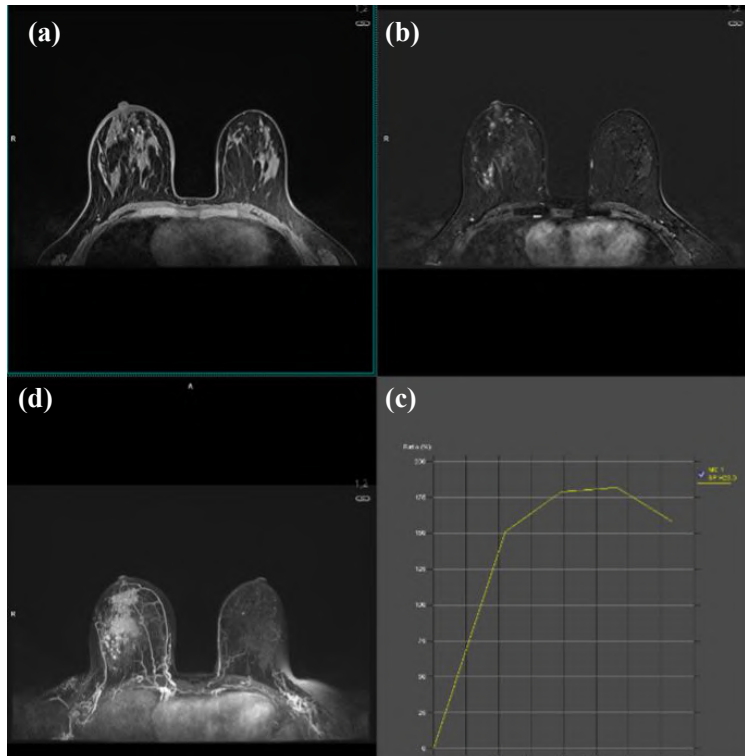
Figure 2.8: MRI image of a patient 42 y.o. Breast MRI T1-weighted (a), (b) T1 SUB after C (which means T1-weighted images acquired after the administration of a contrast agent, with subtraction performed to enhance the visualization of areas showing contrast uptake.), maximum intensity projection (MIP) images (d) and enhancement curve (c) from the tumor. The right breast extended tumor comprises outer quadrants and the borders of the quadrants. In the bottom right, the tumor enhancement curve between the time (x-axis and the signal intensity (y-axis) demonstrates a wash-out pattern, indicating a specific type of contrast uptake and clearance behaviour. Examination performed in Breast Diagnostic Imaging Unit, Diagnostic Imaging Department, University Hospital in Cracow (Pracownia Diagnostyki Obrazowej Piersi Zakładu Diagnostyki Obrazowej Nowego szpitala Uniwersyteckiego w Krakowie).

and the choice of modality depends on factors such as patient characteristics, clinical presentation, and the specific information needed. The integration of multiple imaging modalities and the advancement of technology continues to improve the accuracy and effectiveness of breast cancer diagnosis, leading to better patient outcomes.

2.3 General concepts

2.3.1 Prediction versus explanation

Prediction modelling and explanatory modelling are two different approaches used in statistical analysis [37]. Prediction modelling focuses on developing models that can accurately predict outcomes or estimate future values based on available data. The primary objective is to minimize the prediction error and optimize the accuracy of predictions. In prediction modelling, the emphasis is on identifying the most
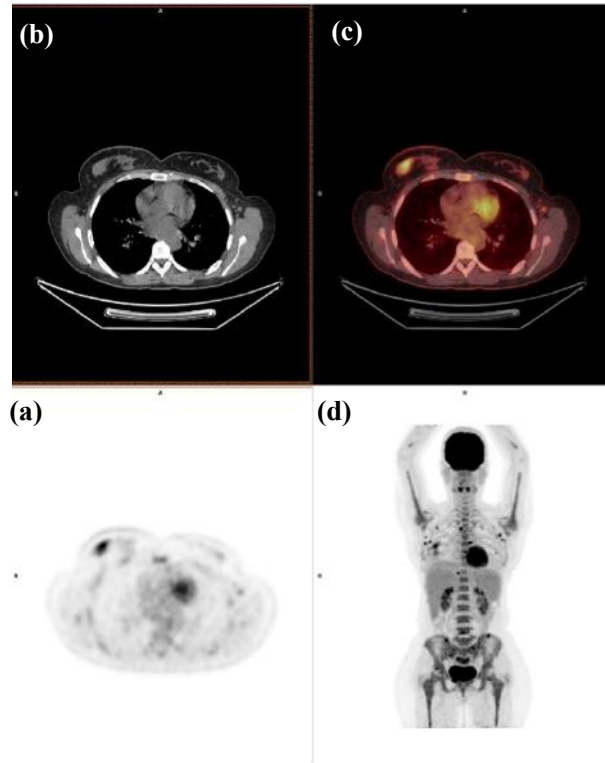
Figure 2.9: PET/CT images. A patient with tumor is observed in the right breast along with multiple metastases in the right axillary lymph nodes. Additionally, there are multiple metastases detected in the bones. (a) PET image, (b) CT transverse projection, (c) fused PET/CT and (d)Maximum intensity projection. Examination performed in PET/CT Unit, Nuclear Medicine Department, University Hospital in Cracow (Pracownia PET/CT Zakładu Medycyny Nuklearnej Nowego Szpitala Uniwersyteckiego in Kraków).

relevant predictive factors and using statistical techniques to create a model that can effectively forecast outcomes in new data. This approach is commonly used in machine learning, data mining, and forecasting [38, 39]. Explanatory modelling, on the other hand, aims to understand and explain the relationship between variables and the underlying causal mechanisms. The focus is on identifying and estimating the causal associations between independent variables (exposures) and dependent variables (outcomes). Explanatory modelling involves assessing the strength and significance of these associations using statistical methods such as regression analysis or experimental designs. This approach is often employed in research studies and scientific investigations to gain insights into the underlying processes and mechanisms driving the observed outcomes [40]. While both prediction and explanatory modelling rely on statistical methods and analyses, they differ in their primary objectives. Prediction modelling is concerned with accurate prediction and forecasting, whereas explanatory modelling focuses on understanding the causal relationships and mechanisms between variables. However, it is worth noting that there can be some overlap between the two approaches, and in some cases, prediction models may provide insights into explanatory factors, and explanatory models may be used for prediction purposes.

2.3.2 Sensitivity and Specificity

Sensitivity and specificity are measures that are commonly used in both prediction modelling and explanatory modelling to assess the performance and accuracy of the models [41]. In prediction modelling, sensitivity and specificity are important measures for evaluating the predictive power of a model. Sensitivity refers to the ability of the model to correctly identify true positives or the proportion of actual positive cases that are correctly classified as positive by the model. It indicates the model's ability to detect the presence of a particular outcome [42]. On the other hand, specificity measures the ability of the model to correctly identify true negatives or the proportion of actual negative cases that are correctly classified as negative by the model. It indicates the model's ability to exclude cases that do not have the outcome of interest [43, 44].

In the context of explanatory modelling, sensitivity and specificity may also be relevant when assessing the performance of a model in correctly identifying the presence or absence of a particular exposure or risk factor. For example, if the objective is to understand the association between a certain risk factor and the occurrence of a disease, sensitivity would indicate how well the model captures the true positive cases where the risk factor is present, while specificity would indicate how well the model correctly identifies the true negative cases where the risk factor is absent.

Overall, sensitivity and specificity play a crucial role in evaluating the accuracy and performance of predictive and explanatory models, helping to determine the model's ability to correctly classify cases and provide insights into the presence or absence of a particular outcome or risk factor.

2.3.3 Confusion Matrix

A confusion matrix is a tabular representation that summarizes the performance of a classification model, as shown in Table 2.1. It provides a detailed breakdown of the model's predictions compared to the true values [45, 46]. The confusion matrix consists of four main components:
1. True Positives (TP): The number of positive cases correctly predicted by the model.
2. True Negatives (TN): The number of negative cases correctly predicted by the model.
3. False Positives (FP): The number of negative cases incorrectly predicted as positive by the model.
4. False Negatives (FN): The number of positive cases incorrectly predicted as negative by the model.

Sensitivity, also known as the true positive rate or recall, is calculated as TP divided by the sum of TP and FN. It represents the fraction of actual positive cases correctly identified by the model. Sensitivity is a measure of how well the model can detect the presence of a particular outcome. Specificity, on the other hand, is calculated as TN divided by the sum of TN and FP. It represents the proportion of actual negative cases correctly identified as negative by the model. Specificity measures how well the model can exclude cases that do not have the outcome of interest. The confusion matrix provides the raw counts for these four components,

which can be used to calculate sensitivity and specificity. Sensitivity and specificity are complementary measures, and their values depend on the distribution of true positive and true negative cases in the data set. These measures help evaluate the performance of a classification model in correctly classifying cases and are useful for assessing the model's ability to detect or exclude a particular outcome.

Table 2.1: A confusion matrix (also known as a table of confusion) is a two-row, two-column table that reports the number of true positives (TP), false negatives (FN), false positives (FP), and true negatives (TN). This enables a more detailed analysis than simply examining the proportion of correct classifications (accuracy).

	Positive (Predictive condition)	Negative (Predictive condition)	Total
Positive (True condition)	True Positive (TP)	False Negative (FN)	(TP+FN)
Negative (True condition)	False Positive (FP)	True Negative (TN)	(FP+TN)
Total	(TP+FP)	(FN+TN)	TP+FP+FN+TN

2.3.4 Receiver Operating Characteristic (ROC) curve

The Receiver Operating Characteristic (ROC) curve is a graphical representation of the performance of a binary classification model, as shown in Figure 2.10 [47]. It illustrates the trade-off between the true positive rate (sensitivity) and the false positive rate (1 - specificity) at various classification thresholds. To construct a ROC curve, the model's predictions and the corresponding true labels are needed. The model's output probabilities or scores determine the classification threshold. The threshold is then adjusted to classify instances as either positive or negative, and the true positive rate (TPR) and false positive rate (FPR) are calculated at each threshold [48]. The ROC curve is created by plotting the TPR against the FPR at
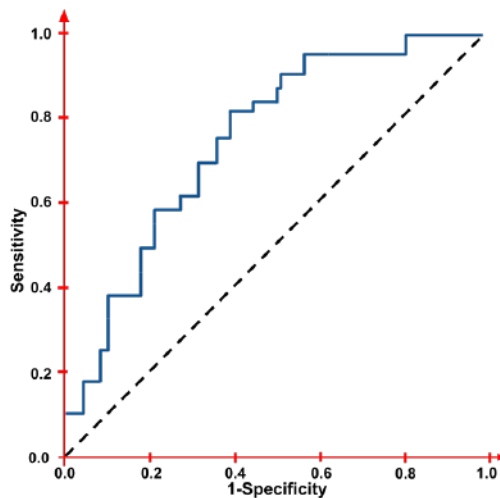
Figure 2.10: Graphical representation of exemplary ROC curve (Bold blue line) of a diagnostic test. (Black dashed line) The diagonal line serves as a reference line.

different threshold settings. The curve represents the model's performance across various threshold choices. The diagonal dashed line in the ROC space represents a random classifier, while a curve that bends towards the top-left corner indicates a better-performing model. The area under the ROC curve (AUC) is often used as a summary measure of the model's discriminative ability. An AUC of 1 represents a perfect classifier, while an AUC of 0.5 indicates a classifier that performs no better than random chance. The ROC curve provides a visual tool to evaluate and compare the performance of different classification models. It allows for selecting an appropriate threshold based on the desired balance between sensitivity and specificity. Additionally, the AUC can provide a single metric to quantify and compare the overall performance of different models.

The confusion matrix provides the necessary information to calculate the TPR and FPR, which are used to construct the ROC curve. The confusion matrix helps in understanding the performance of the model at specific threshold settings. At the same time, the ROC curve provides a comprehensive visualization of the model's performance across various threshold choices.

Chapter 3

Medical data analysis

3.1 Hospital Data

In the University Hospital in Cracow between November 2019 and November 2021, the following examinations were performed: 5250 mammography, 2460 breast ultrasounds, 543 contrast-enhanced mammographies (CEM), 856 breast MRI and 1060 core needle biopsies and Vacuum-assisted breast biopsy (VABB) under ultrasound, mammography, and MRI guidance. The examinations were assessed by three experienced radiologists, two of them with 20 years of experience in mammography and one with 7 years of experience in mammography evaluation.

3.2 Methods and Materials

3.2.1 General Information

A group of 114 patients were included in the study. The hospital's ethics committee approved this retrospective analysis, and all patients provided written informed consent. All of these patients underwent mammography, ultrasound, CEM and MRI before the surgical procedure, and all of them had undergone a pathological assessment of the studied breast lesions via core needle biopsy or surgical excision. The medical records of these patients were reviewed to analyse critical clinicopathological factors such as age, lesion site, tumor size, grade, and histological type. All visible lesions were reviewed by three radiologists. The evaluation was blinded, and the radiologists independently interpreted each modality, each examining a similar number of Conventional mammography (CM), spectral mammography (SM), ultrasound (US), and magnetic resonance imaging (MRI) tests.

- Mammography was performed in the erect position using an adequate mammographic apparatus Mammograph General Electric. It employs a lower-energy X-rays lamp with a rotating anode, typically Mo and additional Rh path (different to common radiography). Two foci: 0,3 mm – big, 0,1 mm – small. The size of foci is adjusted to the size of objects subjected to imaging – microcalcifications – image sharpness. The small focus is used for enlarging.

- Spectral mammography was conducted using a specialized software-equipped General Electric USA apparatus. Women received iodine contrast administration, and both breasts were examined in two different projections. An

automatic syringe was used to administer a contrast medium at a rate of 1.5 ml/kg of body weight, delivered at a speed of 3 ml/s. The first mammography images were captured after a 2-minute interval. The examination always began with the breast that did not exhibit any suspicious pathological abnormalities. The apparatus automatically performed scans in both low-energy projection (energy range of 26 - 32 keV) and high-energy projection (energy range of 45 - 49 keV). These images were displayed on diagnostic monitors as low-energy images, which corresponded to standard mammography images. Additionally, subtraction images were generated, showing attenuated fat tissue and identifiable areas of contrast enhancement. The breasts were then scanned in bilateral craniocaudal (CC) and mediolateral oblique (MLO) projections. The entire procedure typically lasted approximately 15 minutes.

- The ultrasound examinations were conducted with patients lying in the supine position. Lesions displaying suspicious characteristics on ultrasonography, such as irregular solid hypoechoic nodules, a vertical-to-horizontal ratio greater than 1, uneven margins, or punctate calcification, were identified as positive and required subsequent biopsy or excision. The examinations were performed using a Hitachi ultrasound machine equipped with a linear transducer operating at a frequency range of 12-16 MHz.

- All contrast-enhanced MRI scans were conducted using a 1.5T Sola MRI equipment manufactured by Siemens in Erlangen, Germany. Patients were positioned in a prone posture during the scans, and parallel imaging with a 2.0 acceleration factor was employed. A specialized 4-channel breast coil from Siemens was utilized for image acquisition. T1-weighted turbo spin-echo (TSE) sequence, echo-planar diffusion-weighted imaging with apparent diffusion coefficient (DWI/ADC), T2-weighted TSE, and T2-weighted TSE with fat saturation (SPAIR) in the transverse plane were all employed using a specialized 4-channel (Siemens) breast coil. To administer contrast, a power injector from Medrad was employed. The contrast medium was injected at a rate of 2 ml/s, followed by the injection of 20 ml of saline at the same rate.

3.2.2 Evaluation of tumor pathology

After performing imaging examinations, a core biopsy or vacuum-assisted core biopsy was performed. The verification method depended on the lesion size and its availability on imaging examination. If the lesion was visible on ultrasound and corresponded to the lesion visible on mammography, SM or MRI, the biopsy was performed under ultrasound guidance. If the lesion was visible only on mammography in the form of microcalcifications, VABB under mammography guidance was performed. In the case of enhancing microcalcifications on SM or MRI, the mammography-guided biopsy was carried out. In case of the lesion visible as enhancing area on SM, MRI was the next step and if the lesion was still present, biopsy verification was performed also under MRI. The next steps involved specimen evaluation. Specimens obtained with core biopsy or vacuum-assisted core biopsy were fixed in formalin and then embedded in paraffin blocks. After being cut into 4–5 mm slices, the standard hematoxylin and eosin staining procedure was performed. If cancer cells were

present, additional immunohistochemical staining was performed to determine the sub-type of cancer better (such as ER, PR, and HER expression and Ki-67 index).

3.2.3 Statistical analysis

ROC analysis was performed on a lesion-specific basis, generating ROC curves and comparing the areas under the curves (AUC) between MRI and CEM data. The comparison was conducted using a Z-test. Sensitivity, specificity, accuracy, and positive and negative predictive values were calculated using BI-RADS scores of 4. McNamara's test, adjusted for continuity, was used to compare the results. For dependent variables, a student t-test with an alpha significance level of 0.05 was employed to compare lesion sizes. All statistical analyses were performed using STATISTICA 10.0 (Stat Soft, Cracow, Poland).

3.3 Results

3.3.1 Patient characteristics

114 consecutive patients received paired CM, SM, US and MRI, and 141 lesions were visualized by the combination of these methods. Histopathological studies confirmed that 114 patients, among whom 98 had one lesion, 14 had two lesions, and one patient had three lesions detected. The lesions were cancers in 92 cases (70%), and the remaining 39 cases (30%) appeared to be benign. The results of the diagnostic test based on BI-RADS classification are presented below, including the assumption that the value $>=4$ is interpreted as malignant while BI-RADS <4 is benign.

Table 3.1: The sensitivity, accuracy, positive predictive value (PPV), and negative predictive value (NPV) were determined based on the BI-RADS assessment. The values are presented with corresponding 95% confidence intervals.

Specification	CM	SM	USG	MRI
Sensitivity	91.3%	100.0%	93.5%	100.0%
Specificity	28.2%	25.6%	23.1%	20.5%
Accuracy (ACC)	72.5%	77.9%	72.5%	76.3%
PPV	75.0%	76.0%	74.1%	74.8%
NPV	57.9%	100.0%	60.0%	100.0%

3.3.2 BI-RADS Classification

On CM, of 15 lesions classified as BI-RADS 1, 7 proved to be cancer on histopathology. Of 78 lesions classified as BI-RADS 4 on CM, 50 were cancers. Of 34 lesions classified as BI-RADS 5 on CM, 34 proved to be cancers on histopathology. CM had a sensitivity of 91.3%, an accuracy of 72.5%, a PPV of 75%, and an NPV of 57.9% (Table 3.1). On SM, all 10 lesions classified as BI-RADS 1 proved to be benign on histopathology. Of 31 lesions classified as BI-RADS 4 on SM, 12 were cancers. Of 89 lesions classified as BI-RADS 5 on SM, 79 proved to be cancers. Of 1 lesion

classified as BI-RADS 6 on SM, none proved to be cancers on histopathology. SM had a sensitivity of 100%, an accuracy of 77.9%, a PPV of 76%, and an NPV of 100% (Table 3.1). On US, of 14 lesions classified as BI-RADS 1, 6 were cancers. All 1 lesions classified as BI-RADS 2 proved to be benign. Of 51 lesions classified as BI-RADS 4 on US, 21 proved to be cancers. Of 65 lesions classified as BI-RADS 5 on US, all proved to be cancers on histopathology. US had a sensitivity of 93.5%, an accuracy of 72.5%, a PPV of 74.1%, and an NPV of 60% (Table 3.1). On MRI, of 8 lesions classified as BI-RADS 2, all proved to be benign. Of 47 lesions classified as BI-RADS 4 on MRI, 18 of them were cancers. Of 76 lesions categorized as BI-RADS 5 on MRI, 74 proved to be cancer. Breast MRI had a sensitivity of 100%, an accuracy of 76%, a PPV of 74.8%, and an NPV of 100%. Sensitivity, accuracy, PPV and NPV of CM, SM, US and breast MRI, along with 95% confidence intervals, are summarized in Table 3.1.

3.3.3 ROC analysis

ROC curves are constructed by calculating the sensitivity and 1-specificity at various threshold or cut-off values. In this study, threshold values are chosen to correspond to each value of the BI-RADS classification system. Specifically, for cM (MK) and USG, threshold values of 5, 4, 2, and 1 are utilized, while for sM (MS), threshold values of 6, 5, 4, and 1 are employed. For MR, threshold values of 5, 4, and 2 are considered. As a result, the ROC curves consist of 4 points for CM, SM, and USG, and 3 points for MR, as shown in Figure 3.1. The ROC curve analysis was performed using Statistica software.
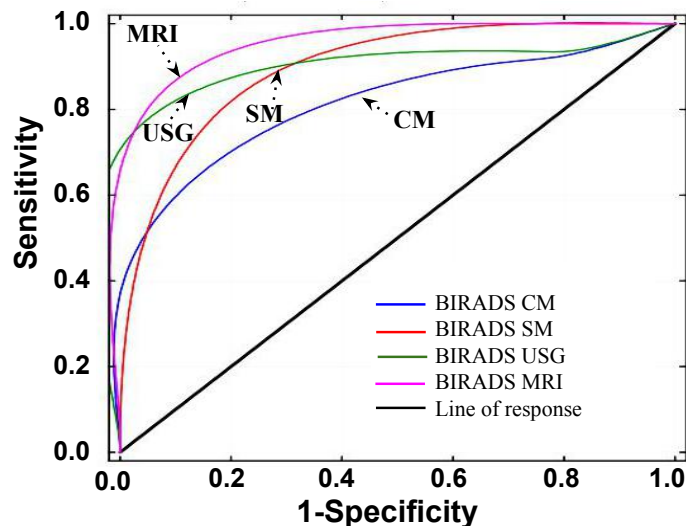
Figure 3.1: Comparison of ROC curves for CM (blue line), SM (red line), USG (green line) and MRI (pink line) based on BI-RADS scores. The reference line (black line) represents the ROC curve for a random distribution of cases with negative and positive test results.

In addition to the positioning, the areas under the ROC curves (AUC) were calculated to quantitatively measure the diagnostic performance. The AUC values

for each modality were reported as follows: CM had an AUC of 0.752, SM had an AUC of 0.825, US had an AUC of 0.854, and MRI had the highest AUC of 0.895. These values indicate the ability of each modality to correctly distinguish between positive and negative cases. To determine whether there were statistically significant differences among the AUC values, a statistical analysis was performed. The analysis resulted in a p-value of 0.001, indicating that there is a significant difference in the AUC values among the different modalities. This suggests that MRI, with the highest AUC, performs significantly better in terms of diagnostic accuracy compared to the other modalities, as presented in Table 3.2.

Table 3.2: The analysis of Receiver Operating Characteristic (ROC) curves included the calculation of Area Under the Curve (AUC) values along with their corresponding 95% confidence intervals. These metrics were employed to evaluate and compare the performance of the diagnostic tests under investigation.

	CM	SM	USG	MRI
AUC	0.72	0.825	0.854	0.897
p	<0.001	<0.001	<0.001	<0.001

3.4 Discussion

Mammography is an established diagnostic method for breast cancer and has proven effective in detecting clinically asymptomatic cases. However, its accuracy is reduced in women with dense glandular breasts, resulting in lower specificity and sensitivity, particularly in high-risk individuals. Despite these limitations, mammography remains the only imaging test proven to reduce breast cancer mortality, with a population-based sensitivity of 75% to 80%. To overcome its shortcomings, other techniques based on mammography principles, such as tomosynthesis and spectral mammography (SM), have been introduced. Tomosynthesis allows for thinner slices in breast imaging but may not detect all lesions, leading to an increase in false negative results. On the other hand, SM utilizes digital mammography and contrast medium administration, enabling evaluation of a larger number of breast lesions, detection of multifocal and multicentric processes, and confirmation or exclusion of focal lesions presence.

Ultrasound (US) is useful for detecting lesions in dense glandular breasts, but it also has limitations, as not all lesions are visible through this modality. SM has been utilized as an alternative for ten years, offering the evaluation of a greater number of breast lesions and the detection of multifocal and multicentric processes. Recent publications suggest that SM is comparable to MRI, which is currently considered the most sensitive and reliable imaging tool for breast cancer detection and staging [49, 50]. MRI is particularly valuable for high-risk patients and those with gene mutations. However, its availability is often limited, and the quality of breast MRI varies across clinics. Conventional mammography (CM), SM, and ultrasound can also aid in breast cancer detection and staging.

In terms of diagnostic performance, MRI exhibited the largest area under the curve (AUC), indicating its effectiveness as an examination. MRI and SM showed 100% sensitivity, while CM and US had lower sensitivity rates. SM demonstrated

the highest accuracy compared to CM, US, and MRI, although the difference was not statistically significant. SM and MRI had 100% negative predictive value (NPV), while CM and US had lower NPV values. SM was found to be the most utilized method in breast cancer diagnostics due to its high sensitivity, accuracy, positive predictive value (PPV), and NPV.

This study provided insights into and comparisons among the imaging modalities of ultrasound (USG), mammography, and MRI for breast cancer detection. Unfortunately, data for PET/CT was not available due to its limited usage in breast cancer detection and the constraints of its availability in Poland. However, according to the literature review, PET/CT has been reported to detect a higher number of breast lesions compared to other modalities, allowing for simultaneous evaluation of both local and general stages of breast cancer [51, 52]. Nevertheless, it's limited availability and high cost currently restrict its application in primary breast cancer diagnostics. Ongoing research aims to develop PET technology with improved accessibility and reduced cost to facilitate breast cancer diagnostics.

Chapter 4

Jagiellonian Positron Emission mammography

4.1 General concept

The first idea of using positron emitters for mammography was proposed in 1994 by C. J. Thompson, K. Murthy, I. N. Weinberg, and F. Mako in their article "Feasibility study for positron emission mammography " [53]. This inspired the concept of detecting breast cancer in its early stages by using the emission tomography technique to visualize functional processes in the body. In early 2012, breast examinations using Europe's first Positron Emission Mammography (PEM) scanner were offered to the patient [54]. This technique is based on the phenomenon that cancer cells have enhanced glucose uptake. The radiopharmaceutical (^{18}F-FDG) is subsequently taken up by the glucose transporter and delivered into the tumor cell. The radiopharmaceutical becomes phosphorylated once within the cell and cannot be transported, resulting in accumulation. When the fluorine-18 nucleus decays, it produces a positron. A positron and an electron collide to create two 511 keV gamma rays emitted 180 degrees off each other. In PEM, these gamma rays are detected by striking a pair of gamma radiation detectors above and below the breast. Studies have also demonstrated that the use of a PEM diagnostic tool has certain potential benefits over mammography, including the capacity to identify suspected lesions in the breast and the ability to distinguish between malignant and benign tumors without the use of X-rays or radiation [55, 56, 57]. And in terms of sensitivity, NPV, and accuracy, the PEM approach is superior to the PET method for detecting primary breast cancer [23]. Naviscan has been one of the commercially available scanners since 2007.

In this thesis, a high-resolution breast-specific PET system called J-PEM has been developed. This device features a fast acquisition rate and a high detector spatial resolution (approximately 5 mm) for breast imaging. Some advantages of this procedure include wavelength shifters, which may improve sensitivity and identification of challenging deep lesions, enhanced detection of small tumors, especially in young women and those with thick breasts, and portable equipment that allows imaging in the operation room.

4.2 Jagiellonian positron emission mammography (J-PEM)

For breast cancer diagnosis, J-PEM employs specialized equipment with two parallel photon detectors in a configuration similar to mammography compressors. As illustrated in Figure 4.1, the detector system comprises two layers of plastic scintillators with wavelength shifters arranged orthogonally between them. For signal readout, each scintillator bar is connected to Silicon Photo-multipliers on both ends in the case of a plastic scintillator. For WLS, the readout Silicon Photo-multipliers are used on one side while on the other side, a reflective foil is used. From the detailed
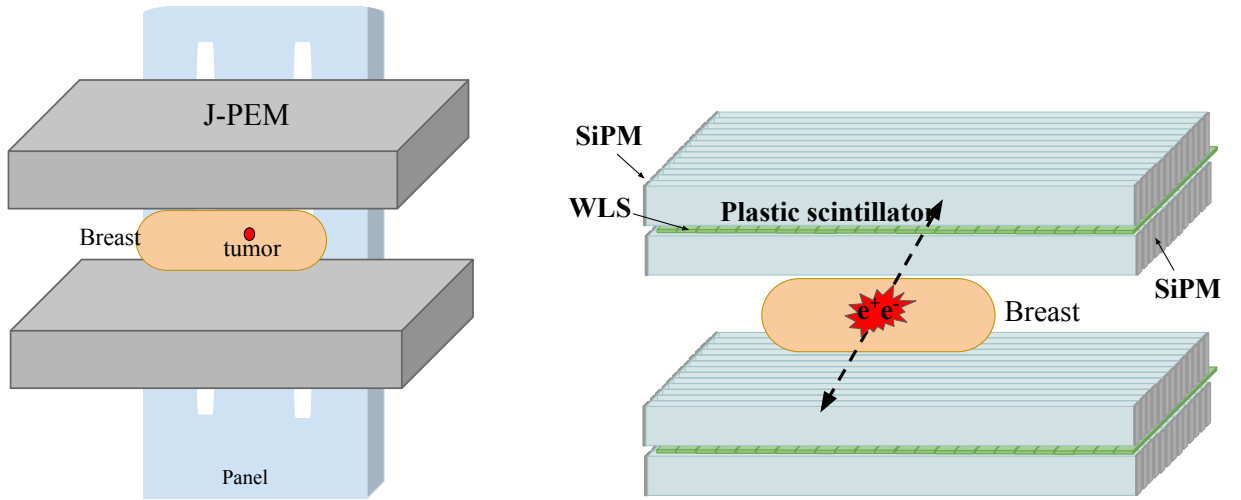
Figure 4.1: (Left) General concept of J-PEM detector design equipment with two parallel photon detectors (grey colour). The figure on the right illustrates the schematic representation of the materials and readout components incorporated within the detectors. The light blue-coloured strips denote the presence of a plastic scintillator, while the green-coloured bar represents the use of wavelength-shifting material (WLS).

studies of the J-PET experiment [2, 58, 59, 60, 61, 62, 63], we are well aware of the properties of plastic scintillators, one of which is having excellent timing qualities. Combined with WLS strips, it can produce a low-cost and accurate scanner that improves spatial resolution and efficiency for breast cancer detection. The position of the gamma interaction point is determined by measuring the timing of the signals arriving at the ends of the long scintillator strips. A resolution of around 10 mm has been reached thus far for plastic scintillators [2, 1]. To achieve high resolution, we propose using an array of WLS to register the scintillation light departing the scintillator bar through a side wall. It has previously been proved that a spatial resolution of 5 mm for the position along the scintillator bar is possible [24, 25]. This thesis presents the construction of such a prototype detector with a single module, as shown in Figure 4.2.

The scintillator is typically surrounded with a reflective material to minimize the loss of light and then is optically coupled to the silicon photo-multiplier on both sides of the scintillator for readout purposes. They are used instead of crystals (see Table 4.1) because they are relatively cheap and effectively reduce the price of the
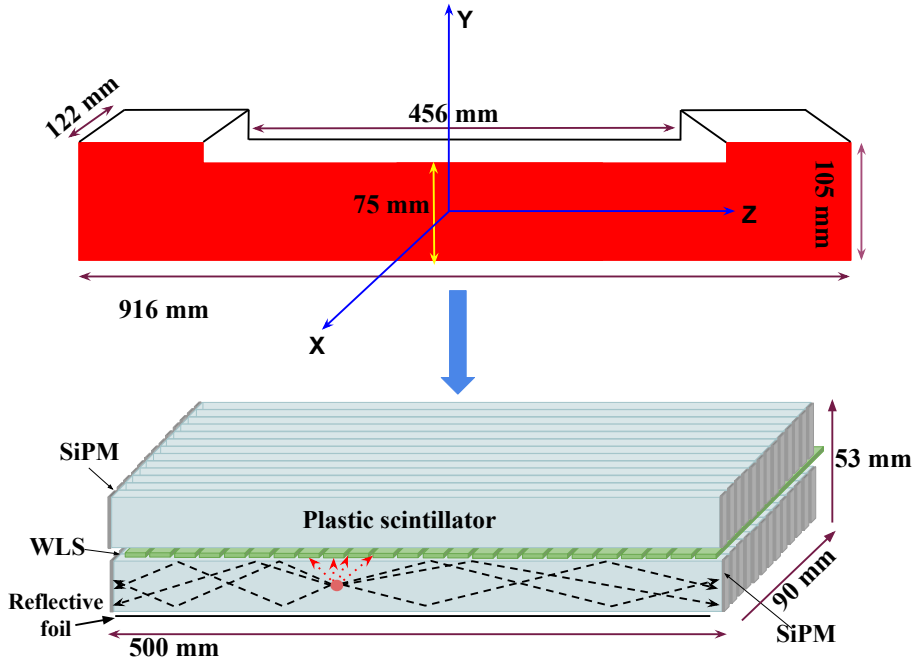
Figure 4.2: Geometrical dimension of the detector setup. Schematic of JPEM Detector setup consisting of 26 plastic scintillators in total and 40 wavelength shifters placed perpendicularly

whole detector [6, 7]. Secondly, they have high timing resolution (in order of 100 ps), offering fast signals with a decay time of 1.8 ns. But plastic scintillators have a noticeably lower detection performance for gamma quanta when compared to inorganic crystals, and it can be compensated by increasing the length and thickness of the scintillator segments because of the flexibility of large light attenuation lengths (in order of 100 - 400 cm) [62]. However, it degrades the time resolution and, as a result, the position resolution also worsens [2]. Even with high precision for measuring the time difference of 100 ps. (FWHM), the resultant position resolution is only modest, equals 7.5 mm (FWHM). This estimation was made with the knowledge that the speed of light propagation in a scintillator strip is around two times slower than in a vacuum [1]. Hence, we use wavelength shifter (WLS) strips to detect scintillation light departing the scintillator segments to increase position resolution. For constructing the J-PEM detector, 26 pieces of Saint-Gobain crystals; BC- 404 plastic scintillator strips with dimensions $500 \times 24 \times 6 \ mm^3$ are used. To prevent light from escaping, the scintillator is wrapped in two distinct types of foils. The first wrapping uses Vikuiti 3M, an Enhanced Specular Reflector (ESR), an ultra-high reflectivity, mirror-like optical polymer film. And the second wrapping is done by using Kapton 100B DuPont. The matte black colour of Kapton polyimide foil provides a uniform, aesthetically pleasing appearance while maintaining key physical properties. The homogeneous pigmentation provides better colour integrity against flexural cracking or abrasion than black coatings or dyes. These characteristics make it ideal for use in many industrial applications where opacity, low reflectivity, or aesthetics are required. The first layer of wrapping was done with Vikuiti, Second layer of wrapping was done with Kapton 100B. For the testing of these scintillators, two types of tests were performed. First was measuring the dimensions of the strip to check the compatibility of obtained scintillators with our requirements and with thickness

tolerance. Width and thickness were measured from both sides near the edges with a calliper with an electronic readout with an accuracy of 0.02 mm and length with an aluminium ruler with an accuracy of 1 mm.
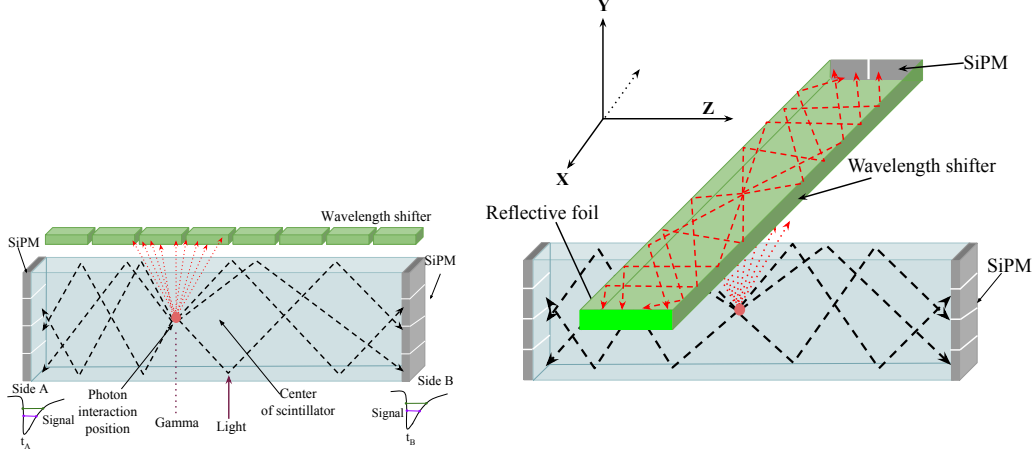
Figure 4.3: The diagram illustrates the interaction occurring within the plastic scintillator (indicated by the red dot), with the subsequent propagation of light (depicted by the black dashed line) towards both sides of the scintillator. The light is then detected by the silicon photo-multipliers (SiPMs) represented in grey. Positioned perpendicularly above the scintillator are wavelength-shifting fibres (WLS), which capture the transmitted light from the plastic scintillator. WLS remit the light with a higher wavelength, which then propagates towards the need of WLS, where they get registered in SiPM. The right-hand figure demonstrates the internal propagation of light within the WLS, depicted in red.

In order to determine the precise location of the interaction point within a plastic scintillator, we propose a method utilizing a set of parallel wavelength-shifting (WLS) strips. These strips are designed to detect scintillation photons that escape from the scintillator material. The concept is illustrated in Figure 4.3, depicting a side view of the scintillator strips and a parallel arrangement of WLS strips positioned above the scintillator. As scintillation photons are emitted, they undergo total internal reflection as they encounter the walls of the scintillator strips, thereby propagating towards a silicon photo-multiplier (SiPM). When the emission angle is smaller than the critical angle, scintillation photons can exit the scintillator strip through the side walls and be absorbed by the adjacent WLS strips [64, 65]. The WLS material chosen is carefully selected to absorb photons falling within a range that corresponds to the emission spectrum of the scintillator, as shown in Figure 4.4.

An important characteristic of this proposed solution is the isotropic emission of photons with wavelengths that experience minimal absorption in the WLS material. This particular feature leads to some of the secondary photons becoming trapped within the WLS fibres and propagating towards the edges via total internal reflection. At the end of these fibres, a SiPM is attached to detect the trapped photons. The position of the interaction point along the z-axis can be determined as a weighted average of z-coordinates of WLS strips with weights equal to amplitudes of
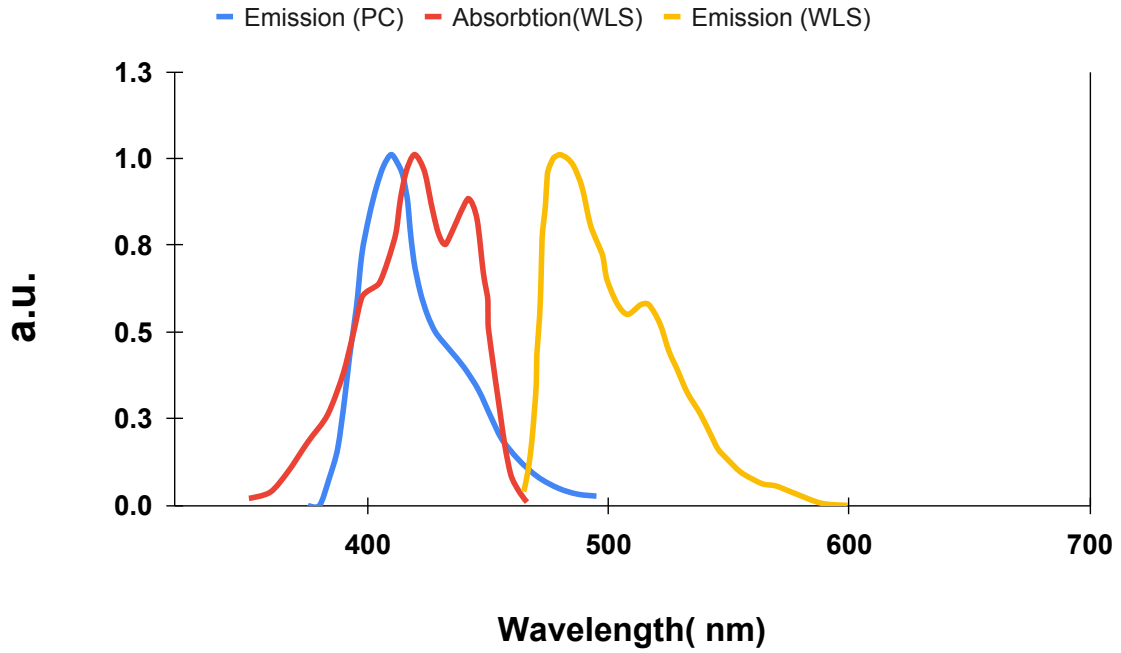
Figure 4.4: The graph depicts the emission spectra of the Plastic scintillator (Blue colour) and the emission and absorption spectra of the wavelength shifter (Yellow and Red colour).

signals registered in the WLS strips being proportional to the numbers of absorbed scintillation photons [25, 24]. And for the position of the interaction point along the y-axis is determined from the number of WLS strips that registered the photons. The wavelength shifter we use in the detector is BC-482A, a green-emitting WLS
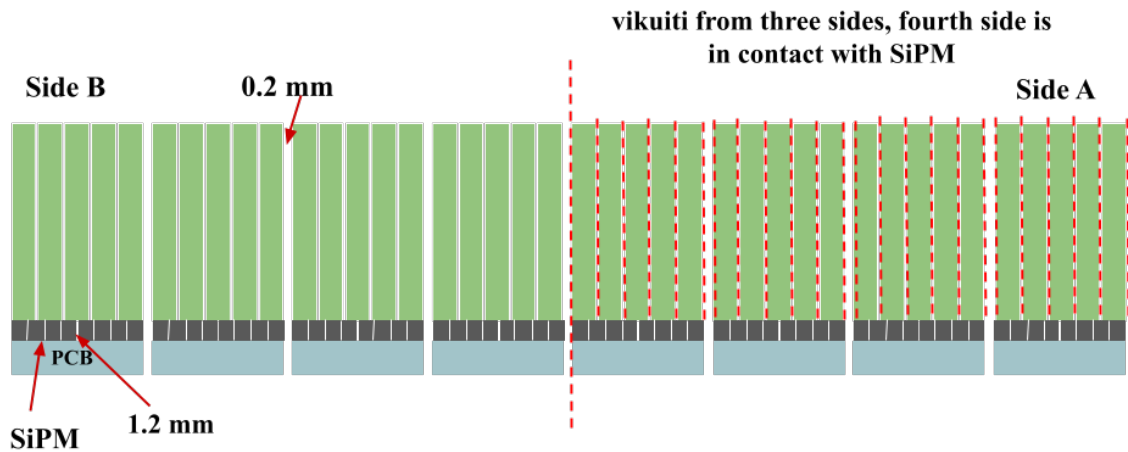
Figure 4.5: Diagram showing the placement of WLS in the detector setup. The green colour 40 WLS are connected to the SiPM (dark grey squares) for readout purposes. The first 20 WLS have a reflective surface from only one side, the opposite side to the SiPM. Next, 20 WLS are covered with reflective foil from three sides. The left side of the red dashed line is WLS without the Vikuiti, and the right side is WLS and has Vikuiti from three sides. The light blue colour represents the PCB on which SiPM is mounted.

29

plastic ideal for shifting the emission spectra of common blue scintillators (BC-404). So half of WLS in the J-PEM has Vikuiti on the two sides 100 mm x 3 mm(side surface between WLS), and on one side, 3 mm x 10 mm, opposite to SiPM. This was done to check how wrapping would influence the output signal and spatial resolution. The top and bottom surfaces of WLS 100 mm x 10 mm can not have foils because it reads blue light from the scintillator from up and down, as shown in Figure 4.5. Figure 4.6, Figure 4.7 and Figure 4.8 illustrates the complete composition of the detector, showcasing its various components and their arrangement.
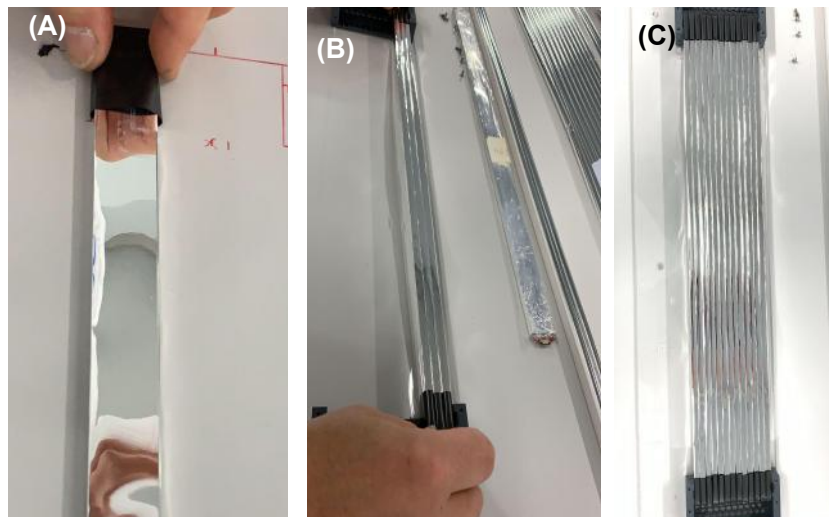
Figure 4.6: The figures depict the assembly process for the first layer of the plastic scintillator. In step (A), each scintillator was individually wrapped in reflective foil. Subsequently, in steps (B) and (C), all 13 scintillators were arranged adjacent to each other.

4.3 Methods and Design

4.3.1 Scintillator

Scintillators are materials capable of converting some of the energy of an incoming high-energy particle into low-energy photons, usually in the ultraviolet to the visible range [66]. As scintillation photons need to be able to escape the material to be detected, a scintillating material must be a homogeneous, transparent solid (can also be liquid) that does not significantly absorb the emitted photons [67, 68]. The interaction process of radiation in the scintillator depends on the ionizing radiation type and the scintillator elements. When the high energy X-ray or gamma ray interacts with the scintillator material, there is the possibility that three processes will occur; photoelectric absorption, Compton scattering, and pair production. Photoelectric effect and Compton scattering are dominant mechanisms of low to medium energies (less than 100 keV) and between 100 keV and 1 MeV, respectively. For energies above 1.02 MeV, the interaction between radiation and matter may also occur by creating pairs of electrons and positrons [69, 70]. This implies that this phenomenon cannot occur for 511 keV gamma quanta. Gamma quanta in PET or PEM have an energy of 511 keV because the energy of two annihilation photons equals the sum of electron
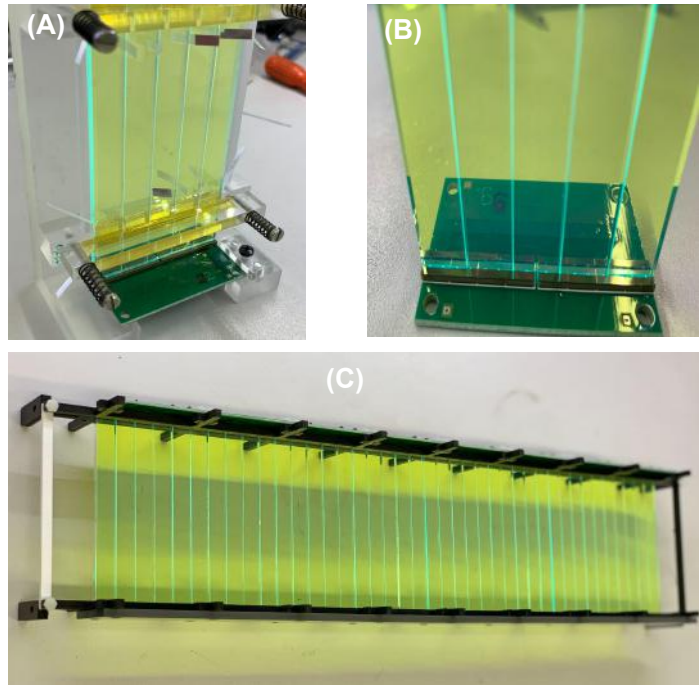
Figure 4.7: The images illustrate the second layer of the J-PEM constructed using WLS (Wavelength Shifting) material. In step (A), the WLS was attached in batches of five, as the connection of SiPMs (Silicon Photo-multipliers) is not a one-to-one correspondence (B). Finally, in step (C), the complete layer was assembled by combining all eight batches of 5 WLS .
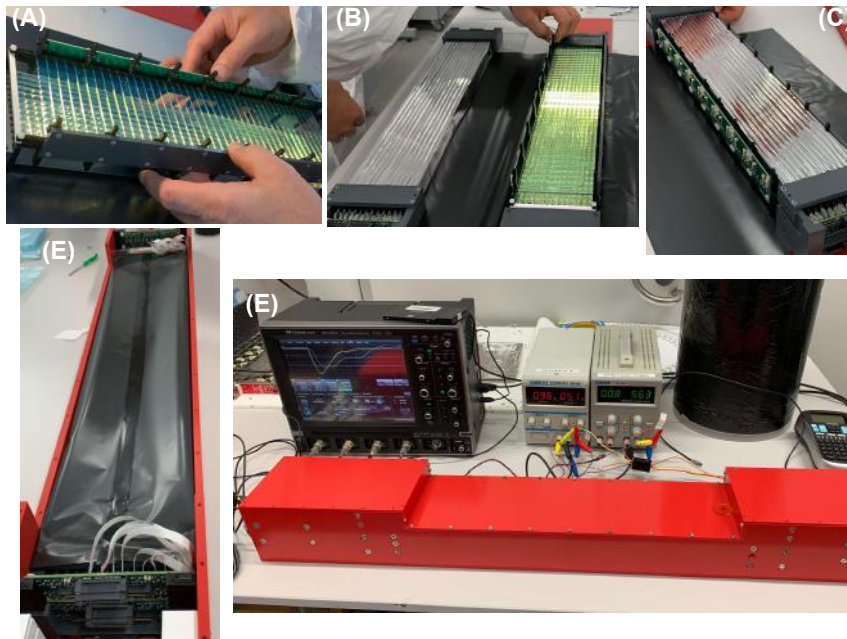
Figure 4.8: After individually assembling each layer, they were then interconnected. The assembly comprised the first and third layers comprising plastic scintillators, while the second layer consisted of WLS materials (depicted in images A, B, and C). The entire structure was covered with black foil to ensure light tightness (shown in image D). Once the complete covering was done, the J-PEM (J-PET Emission Mammography) setup was prepared for testing (illustrated in image E).

and positron masses [71, 72]. Due to these interactions, a lot of excited secondary electrons are generated. These secondary electrons interact with lattice and other electrons, where they dissipate their kinetic energy. Finally, scintillation photons are emitted when these secondary electrons recombine with holes. For every MeV of energy the electron deposits, tens of thousands of photons are normally emitted.

There are primarily two types of scintillators distinguished based on the structure, organic and inorganic, with different photo-physical processes [73, 61]. The main detection mechanism for these types is fluorescence, which is the fast emission of visible radiation (light). The following are the most significant scintillator parameters [67, 74]:

- light output - the number of photons generated per 1 keV of energy deposited by quanta in the scintillator. This is important because photo-electron statistics determine the resolution of energy deposition.

- The luminescence decay time should be as short as feasible. As ultimate time resolution depends on the decay and rise time of the scintillator.

- The resolution of energy should be high.

- High stopping power

- When gamma interacts with the scintillator, it deposits some or all of its energy. Then it produces light which transmits throughout the scintillator isotropically in the visible range of electromagnetic spectra. As the likelihood of 511 keV interaction is proportional to the density of material related to atomic number, the scintillator should be composed of large atomic number elements.

- **Inorganic Scintillator :**

Inorganic scintillators have been designed to offer the high light yields necessary to get high energy resolution for gamma spectroscopy and are available as single crystals, glasses, and transparent ceramics [67]. Despite the fact that inorganic scintillators can be made in large sizes, their cost rises, and their performance deteriorates in large quantities due to material and optical in-homogeneity [68]. Inorganic scintillators are typically crystals grown in high-temperature furnaces, such as alkali metal halides, doped with a small trace of activator metal ions. The crystal lattice structure determines the mechanism of scintillation [68, 61]. In the pure crystal, the charged particle interacts and absorbs the energy, which leads to the transition of electrons from the valence band to the conduction band. However, electrons are inefficient in returning to the valence band with photon emission because band gap widths are such that the resulting radiated photon is too high to be in the visible range. As a result, small quantities of doping are added to the crystal. electrons from the conduction band transit to the activator excited level. Scintillation in inorganic crystals is typically slower than in organic ones, as shown in Table 4.1.

- **Organic Scintillator :**

Organic scintillators comprise a transparent host material doped with a scintillating organic molecule [61]. The scintillation mechanism in organic materials is quite different from the mechanism in inorganic crystals. In inorganic scintillators, e.g., NaI, and CsI, scintillation arises because of the structure of the crystal lattice, as explained previously. The fluorescence mechanism in organic materials arises from transitions in the energy levels of a single molecule [73].

4.3.1.1 Plastic scintillator

Plastic scintillators are organic scintillators typically made up of an aromatic organic matrix and one or more dissolved fluorescent dyes (a primary fluor, and a secondary fluor, which also serve as wavelength shifters (WLS)) that allow for light emission [68]. The most common method of making plastic scintillators is bulk free-radical polymerization, which often uses poly(vinyl toluene) and polystyrene as the polymerizable matrix, provides benefits of simplicity, scalability, and controlled polymerization around solutes, such as fluors (to wavelength shift the emission) and high-Z components [75]. In organic scintillators, the polymer base or aromatic ma-
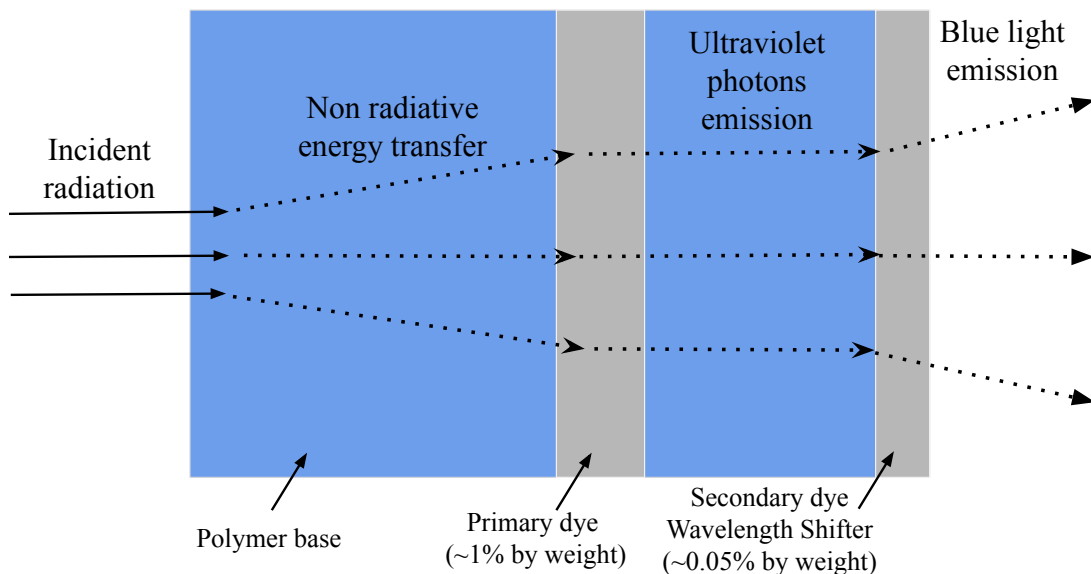
Figure 4.9: A plastic scintillator's functioning mechanism. An incident's radiation interacts with the plastic basis. The deposited energy is subsequently transferred to the primary dye and WLS. The primary dye produced ultraviolet photons, which the wavelength shifter converted into visible light (This figure is from [61]).

trix produces UV when ionized, but the mean free path of the generated photons is too short, as a result, scintillation additives are employed. Additives (fluors) absorb primary light from the base and emit it at longer wavelengths. It is fair to assume that any direct excitation of these dyes by the ionizing particle will not occur and

that all ionization and subsequent relaxation to excited states will initially only oc-
cur on the matrix if the total concentration of these dyes is minimal (no more than
a few wt%). The typical distance between a fluor molecule and an excited base
molecule at the concentrations utilized (1% and more) is roughly 10 nm, which is
substantially smaller than a wavelength of light. The major mechanism of energy
transfer from base to fluor at these distances is a resonant dipole-dipole interaction
between the energy donor (polymer) and acceptor (primary solute), described by
Förster, which strongly links the base and fluor. Primary dye loadings are normally
between 1 and 5 weight %, a level that for the majority of dyes will result in a large
loss of the released photons owing to self-absorption, to guarantee the full and effi-
cient transmission of the excitation energy [76]. To reduce these losses, a secondary,
wavelength-shifting dye that has a much lower loading content (0.005-0.5 wt.%) is
added. Its sole purpose is to absorb the photons released by the primary dye and
re-emit them at longer wavelengths than the primary dye can absorb, thereby in-
creasing the amount of out-coupled photons released from the material. Depending
on the required wavelength of radiated photons, one or several fluors can be utilized
[68, 61], see Figure 4.9.
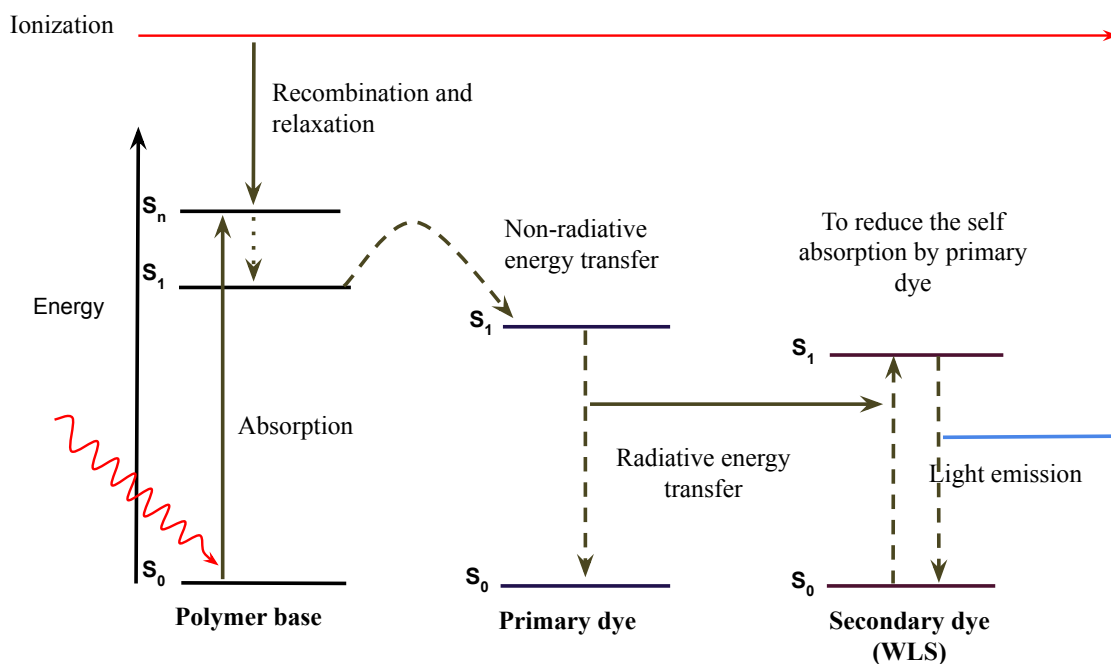
Figure 4.10: This figure summarises the overall scintillation process and the primary
processes involved. The figure is adapted from [76]

Since plastic scintillators consist mainly of elements with atomic numbers, such
as carbon and hydrogen, they have a low probability of photoelectric absorption.
Hence, the gamma rays rarely react through photoelectric absorption. Therefore
when gamma rays interact with plastic scintillator detectors, the Compton scatter-
ing dominates among photoelectric absorption, the Compton scattering, and the
production of pair [77, 61], as shown in Figure 4.11. When gamma quanta travel

through a plastic scintillator, it first interacts with the polymer and expels electrons from it. These electrons possess part of gamma energy, which is responsible for the excitation of other regions of the polymer. The excited polymer transmits some of its energy to the fluorescent additive by non-radiative methods (the Förster resonance energy transfer), resulting in no light emission [61, 78]. The fluorescence additive then absorbs this energy and returns a portion of it by radiative transfer - fluorescence in ultraviolet light. The last phase includes the absorption of UV light by a wavelength shifter and de-excitation by the emission of a longer wavelength photon, which releases blue light via fluorescence, see Figure 4.10.

The scintillation light is emitted isotropically inside the scintillator and is transmitted throughout the scintillator via total internal reflection. The scintillator is typically surrounded with a reflective material to minimize the loss of light and then is optically coupled to the silicon photo-multiplier on both sides (in the case of J-PEM) of the scintillator for readout purposes.
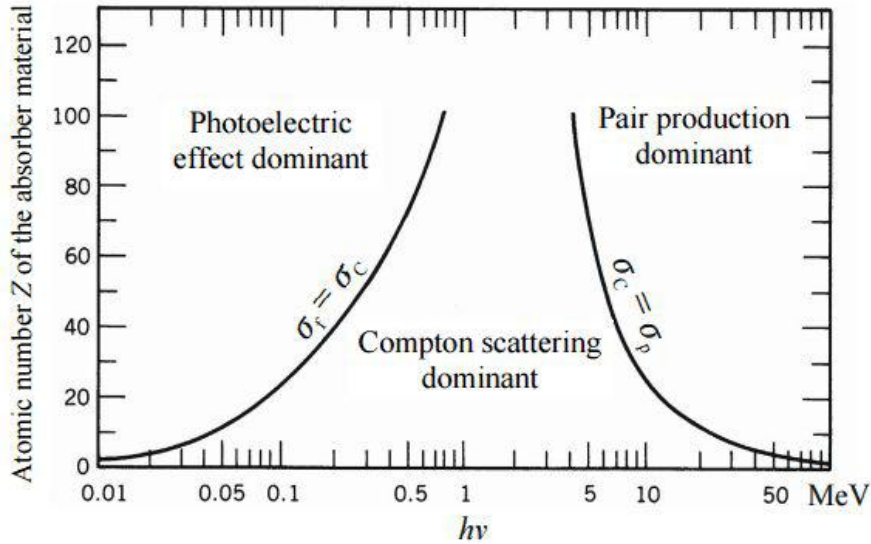
Figure 4.11: The significance of the three basic forms of gamma-ray interaction. The lines represent Z and hv values for which the two surrounding impacts are equal [77]

The reason for using them instead of crystals (see Table 4.1) is that they are relatively cheap and effectively reduce the price of the whole detector. Secondly, they have high timing resolution (in order of 100 ps) as it offers fast signals with a decay time of 1.8 ns [6, 7].

- **BC-404:**

For the construction of the J-PEM detector, 26 pieces of Saint-Gobain crystals; BC-404 plastic scintillator strips with dimensions $500 \times 24 \times 6 \ mm^3$ are used. To prevent light from escaping, the scintillator is wrapped in two distinct types of foils Figure 4.12.

For the testing of these scintillators, two types of tests were performed. First was measuring the dimensions of the strip to check the compatibility of obtained

Table 4.1: Comparison of the properties of crystals and plastic scintillator [79, 81, 82, 83, 84, 85, 86, 87, 88, 80].

Characteristic	NaI(Tl)	BGO (Bi4Ge3O12)	LSO,LYSO	GSO (Gd2SiO5:Ce)	BaF2	LaBr3(Ce)	LXe (Liquid xenon)	BC404 (Plastic scintillator)
Effective atomic number	50	74	66	59	52	46.7	54	5.7
Density(g/cm3)	3.7	7.1	7.4	6.7	4.9	5.3	3.06	1.023
Scintillation decay time (ns)	230	300	40	60	0.6	~25	27/45* (30%/70%)	1.8
Energy resolution at 511 keV (%)	6.6	20	10	8.5	11.4	3.6	10	9 (@340 Kev)
light output (Photons/MeV)	100	15	75	25	5	175	90/30*	26
Refractive index	1.85	2.15	1.82	1.85	1.54	1.90	1.6	1.58
Linear attenuation coefficient, μ (cm-1)	0.35	0.96	0.87	0.7	0.44	0.47	0.29	0.0980
Photoelectric fraction (%)	17	40	32	25	17	13	21	0.0063

(a) First wrapping is done by Vikuiti 3M warpping

(b) the second wrapping is done by wrapped in ESR

Figure 4.12: Wrapping scheme of a single plastic scintillator

scintillators with our requirements and with thickness tolerance. Width and thickness were measured from both sides near the edges with a calliper with an electronic

readout with an accuracy of 0.02 mm and length with an aluminium ruler with an accuracy of 1 mm. Protective foil was removed before the test for BC-404 was a strip examination by eye under UV light and a test of its optical properties. Scintillation strips were illuminated from one side (5 cm area from the edge) by a UV lamp, and the resulting blue light was read with a photodiode on the second side, Figure 4.13.

(a)   (b)
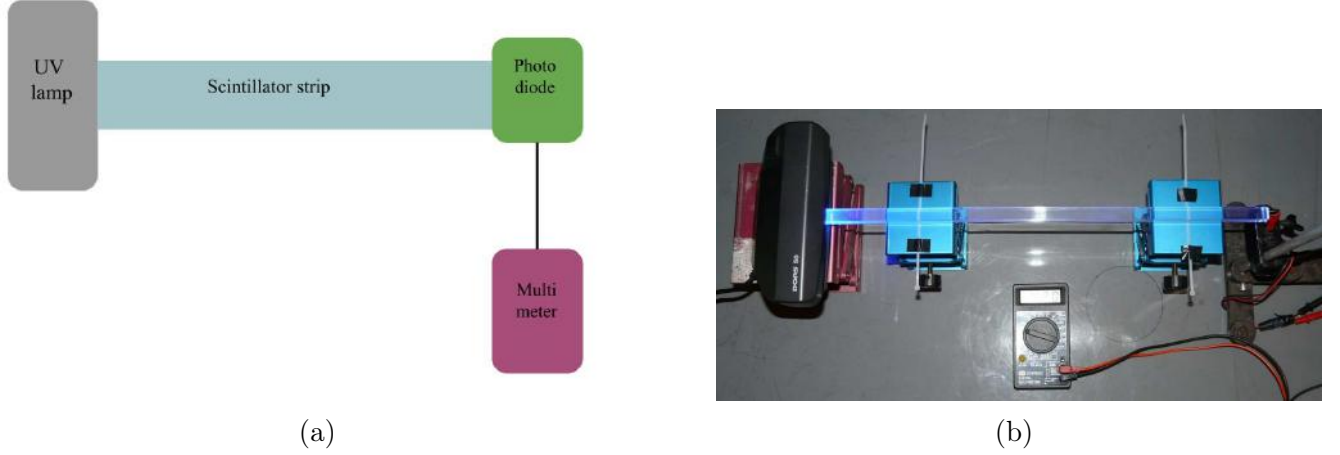
Figure 4.13: Scheme of the experimental setup (left) and its photograph (right) used in BC-404 measurements

The photodiode converts the incoming light into electric pulses whose amplitudes are measured using a multimeter. Every strip was examined two times with a photodiode coupled to the left and right sides. A fractional change of the voltage measured on the left and right side:

$$C = 100\% \frac{|V_{Left} - V_{Right}|}{(V_{Left} - Background + V_{Right} - Background)/2}$$

can be used as a measure of the scintillator optical homogeneity. The big difference (more than 20% value of C parameter) of amplitudes measured at both ends indicates the presence of some defects in the scintillator's volume. As a result, the extreme value of the C parameter comes out to 6.14%, in the case of the scintillator, which means all scintillators have good homogeneous optical properties in volume.

4.3.2   Wavelength shifter

Wavelength shifter comprising a supporting structure of solid material, fluoropolymer and a fluorescent wavelength shifting dye capable of absorbing light in the UV range and re-emit light in the visible range [89, 90]. Absorption of light depends on the thickness of WLS, the concentration of fluorescent type, and the type of fluorescent dye used in the making process. It is made by dissolving a powder mixture of the fluoropolymer and WLS dye in liquid monomer solvent to obtain a solution of 0.001% to 0.2% by weight of the dye in the fluoro-thermoplastic material, where the wavelength-shifting dye is chosen from the group consisting of 1-phenyl-3-mesityl-2-pyrazoline (C18H20N2), 1,4bis (5-phenyloxazol-2-yl) benzene (POPOP), p-bis (omethylstyryl) benzene (bis-MSB) [91]. These aromatic organic compounds fluoresce when their pie-orbital electrons are excited, either by ionizing particles or
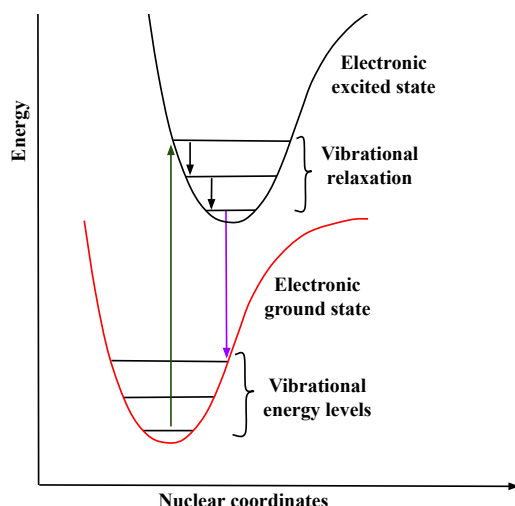
Figure 4.14: Principle of absorption and emission processes in WLS fluorescent dye. This figure is adapted from [92]

UV radiation. When an electron is promoted to an electronically excited state, it often ends up in an excited vibrational state as well, the first excited state (S1). Thus, some of the energy put into electronic excitation is immediately passed into vibrational energy. The vibrational energy, however, doesn't just transfer in photons [93]. It can be gained or lost through molecular collisions and heat transfer. The electron might drop down again immediately; a photon would be emitted of exactly the same wavelength as the one that was previously absorbed. On the other hand, if the molecule relaxes into a lower vibrational state, some of that initial energy will have been lost as heat. When the electron relaxes within picoseconds, the distance back to the ground state is slightly shorter. The photon that is emitted will have lower energy and a longer wavelength than the initial one. If the concentration of the wavelength-shifting solute is high enough, this energy is transferred by non-radiative dipole-dipole interactions to its excited levels producing fluorescence. This phenomenon was explained by Franck's codon principle [92, 94, 95], shown in Figure 4.14.

Blue light from a plastic scintillator, as shown in Figure 4.15, gets absorbed in the polymer base; after travelling a few micrometres, it reaches the WLS material, where it gets re-emitted with higher wavelength light (green light in my case). This shift in wavelength occurs due to the Franck–Condon principle.

- **BC-482A:**

In J-PEM, 40 pieces of BC-482A wavelength shifter bars with dimensions 100x10x3 mm^3 and rectangular cross-section are used from Saint-Gobain Crystals. large surfaces were as-cast, edges were diamond-milled and secured with soft, sticky removable plastic foil. The properties of these WLS are mentioned in Table 4.2 [96, 97].

- **Experimental test:**

An optical test for BC-482A was performed with the same setup, except the UV lamp was replaced with a laser pointer. UV lamp with optical filter cut off UV
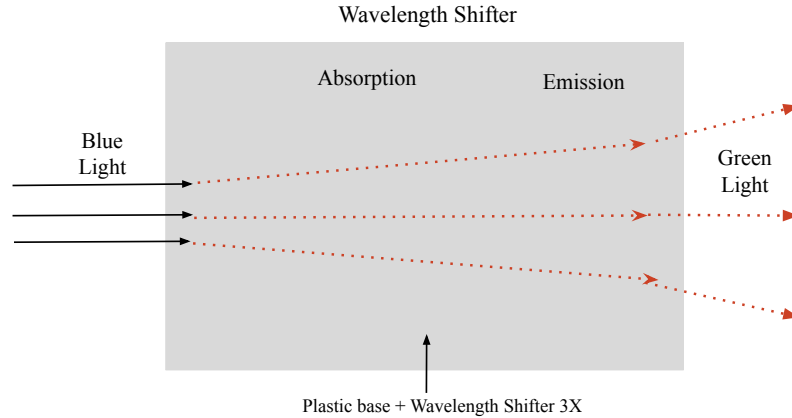
Figure 4.15: Wavelength Shifter functioning mechanism. Blue light from a plastic scintillator interacts with the WLS bar/strip. The scintillator produced blue photons, which the wavelength shifter converted into green light.

Table 4.2: Properties of BC-482A wavelength shifter.

The wavelength of maximum emission (nm)	494
The wavelength of maximum absorption (nm)	420
Decay time (ns)	12
Quantum efficiency (%)	86
Density (g/cc)	1.03
Polymer base	Polyvinyltoluene
Refractive index	1.58
Softeing point	70°C
Vapor pressure	Vacuum-compatible
Coefficient of Linear Expansion	7.8 x 10-5 below 67°C

light at 380 nm does not match BC-482A with absorption peak around 420 nm. Instead, a laser pointer was used with a 405 nm emission wavelength (blue light) that overlaps the absorption spectrum of the BC-482A wavelength shifter bar. The pointer was set perpendicularly to the shifter bar at 1 cm from the end of the bar (Figure 4.16). Every bar was examined two times with a photodiode coupled to the left and right sides. The results of these measurements are that the extreme value of the C parameter is 2.3%, and that means all wavelength shifter bars have good homogeneous optical properties in volume.

4.4   Electronic readouts

Read-out and data acquisition (DAQ) are specialized technical areas of engineering and science that thrive primarily in the community of major research operations. It comprises mostly electronics, computer science, networking, and physics. The general structure of the readout consists of Front end electronics and a data acquisition
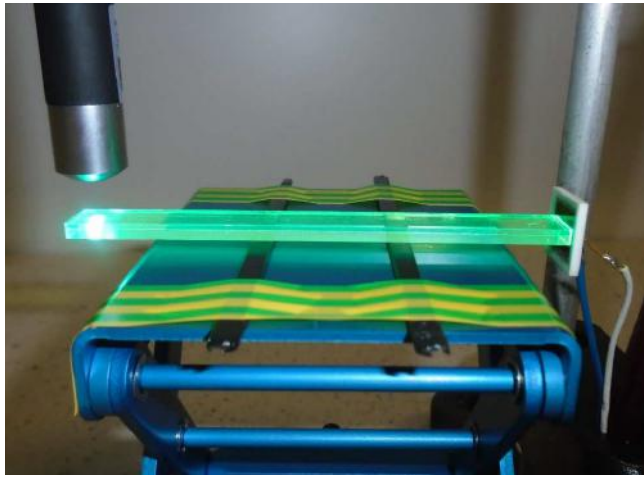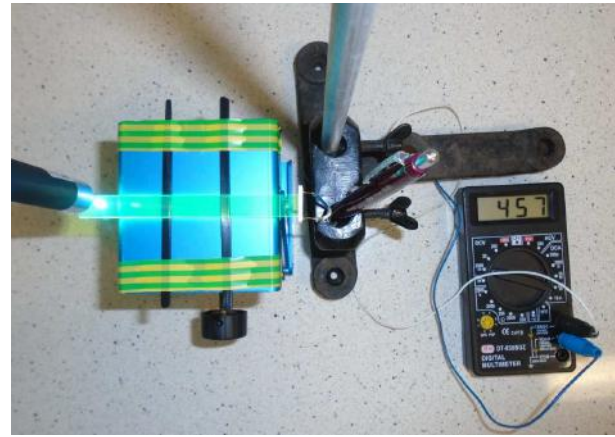
<center>(a)   (b)</center>

Figure 4.16: Photograph of the experimental setup used in measurement for BC-482A: top view (left) and side view (right). WLS bar is excited by a blue laser, and the converted green light is read out by a photodiode mounted at one end of WLS

system, Figure 4.17. A more detailed explanation follows.
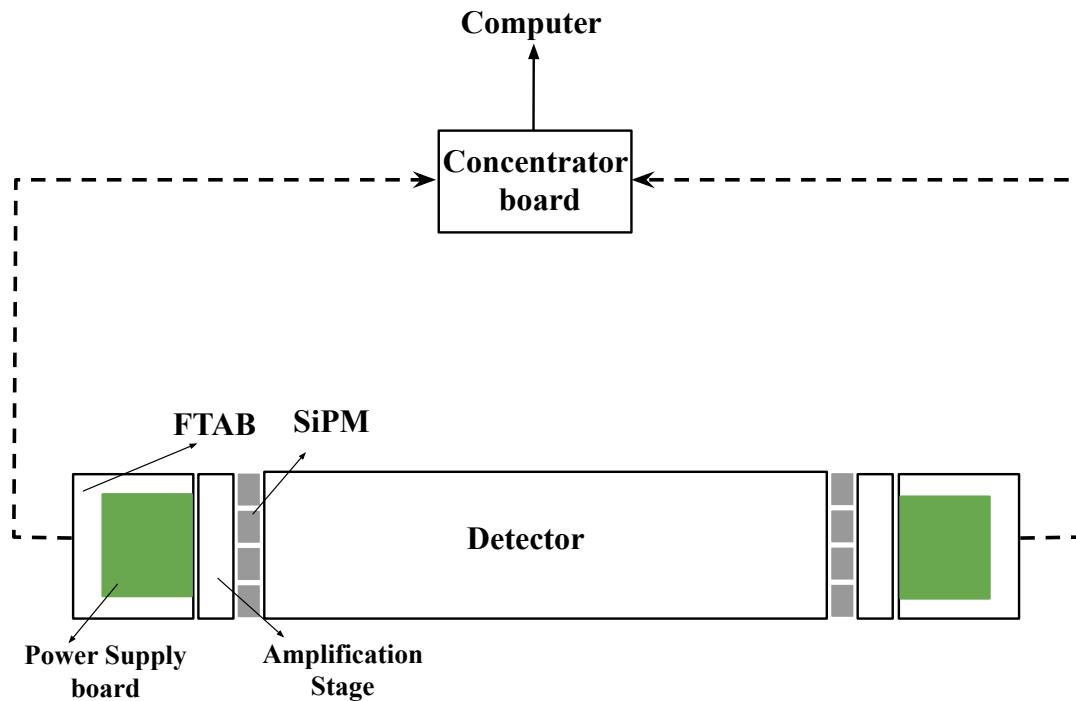
Figure 4.17: Readout chain for scintillation detector

4.4.1 Front-end electronics

The front-end electronics (FEE) are the electronic components that are directly connected to the detector (sensitive element). Their purpose is to acquire an electrical

<center>40</center>

signal from the detector and tailor the system's response to optimize the minimum detectable signal and energy measurement, and time of arrival, as well as digitize and store the signal for later processing. This is a broad term for a system that records the electrical response of the detector and organizes its transmission to storage.

- **Analog:**

The analogue FEE interfaces the detector response signal with the digitizer. The nature of these detector electrical responses varies depending on the detector type and ranges in time from ns to microseconds with modest amplitudes (tens of mV). To determine the timing and amplitude of these signals, fast shaping and amplification are necessary (for charge measurement). As a result, the analogue portion of the FEE is made up of signal amplifiers, shapers, and, in certain cases, discriminators, followed by a digitization unit. To decrease signal losses and parasitic capacitance, the analogue FEE is always located close to or directly linked to the detector.

- **Digital:**

The digital FEE is responsible for translating the shaped signal from the analogue to the digital domain. Analog to Digital Converters (ADC) and Time Digital Converters (TDC) are the most common forms. The function of the digital front end (block of digital filters) is typically to perform gain control, sampling rate conversion, pulse shaping, matched filtering, and phase correction.

Front-end electronics in J-PEM consist of the silicon photo-multipliers, for the readout of the scintillation from the Scintillator and WLS, which convert the emitted photons into electrical pulses. The section that follows specifies these parameters and describes how they are evaluated. It also consists of an amplification stage, power distribution board, and front-end TDC acquisition board, explained below in detail. For the understanding, the performance of a SiPM requires knowledge of the following parameters: SPAD (Single-photon avalanche photo-diode), gain, Photon detection efficiency (PDE), dark count rate (noise), optical cross-talk, and after-pulsing. Hence these parameters are explained in detail below.

4.4.2 Silicon Photo-multipliers (SiPMs)

Silicon Photo-multipliers (SiPMs) manufactured by Hamamatsu are advanced solid-state silicon detectors capable of single photon counting. SiPMs possess numerous advantages and exhibit exceptional performance in various applications. These SiPMs exhibit a quantum efficiency of approximately 40% at 450 nm (Figure 4.19), effective for emissions in plastic scintillators. They can operate within a temperature range of -40°C to +85°C. The SiPMs utilized in our experiments feature an active area of 6×6 mm^2 and multiple channels (Figure 4.18). Specifically, we conducted our experiments using a 36 mm^2 photosensitive SiPM from the S13361 series.

Figure 4.18: (left) Pictorial representation of SiPM mounted on red board. (right) Representation of test setup consisting of a light-tight container with scintillator and SiPMs inside.

In this study, we present the findings obtained from the analysis of the SiPM model S13361-5797, focusing on its amplitude spectra, charge spectra, and time difference spectra (with varying threshold values) to assess its time resolution. For this particular SiPM model, we exclusively employed a single operational voltage to establish a reference framework. Comparison of commercially available photo-diodes is shown Table 4.3 There are several factors that should be considered are sensitivity, spectral range, dark current, and noise characteristics. By examining these factors, one can make an informed decision on which photodiode best suits their specific application requirements.
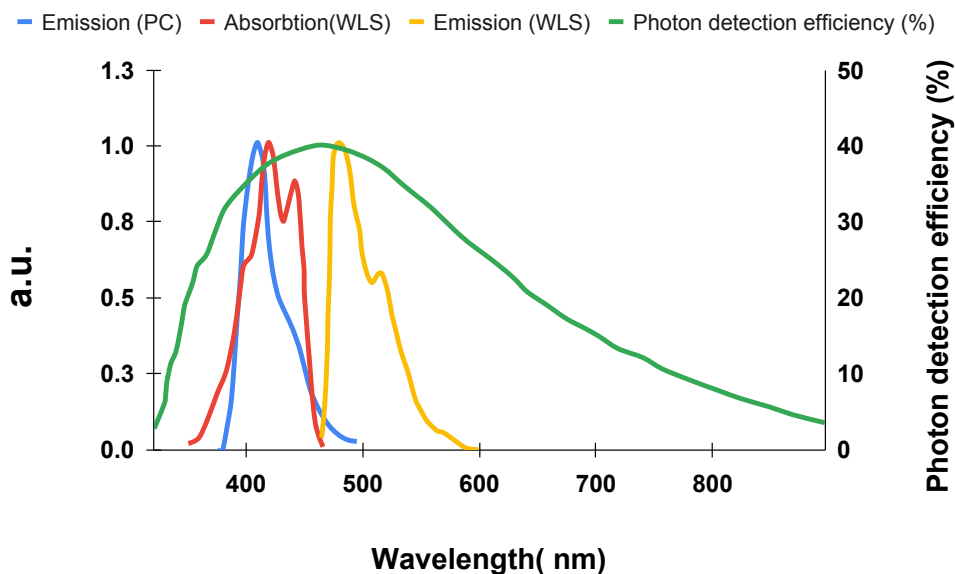
Figure 4.19: The figure demonstrates the emission spectra of the plastic scintillator (depicted in blue) and the emission and absorption spectra of the wavelength-shifting material (WLS) (illustrated in red and yellow, respectively). Both the emission and absorption spectra of the plastic scintillator and the WLS fall within the quantum efficiency range of the silicon photo-multiplier (SiPM), which is represented by the green colour.

Table 4.3: Comaprison between photo-diodes, which are commercially available

	Photo-Diode	APD	PMT	SiPM (MPPC)
Gain	1	<100	10^5-10^7	10^5-10^7
Spectral range	Up to 1200 nm (Silicon)	Up to 1150 nm	190 to 1700 nm	320 to 900 nm
Bias voltage	$\sim$few V	$\sim$200 V	$\sim$1000V	$\sim$60V
Magnetic field	Immune	Immune	Need protection	Immune
Dark Output	Limited by amplifier	Limited by amplifier	Up to 500 CPS (quiet)	Up to 1000 KCPS (Noisy)
Temperature sensitivity	Low	High	Low	Medium
System timimg	Slow	Fast	Fast/very fast	Fast

4.4.2.1 Experimental Setup

To assess the performance of the SiPMs, the power boards were affixed to each of them, as depicted in Figure 4.20. The arrangement of the boards enabled the signal to be read out using a LEMO cable, while the voltage could be manually adjusted using a power supply. For signal probing purposes, an Infiniium oscilloscope was employed.
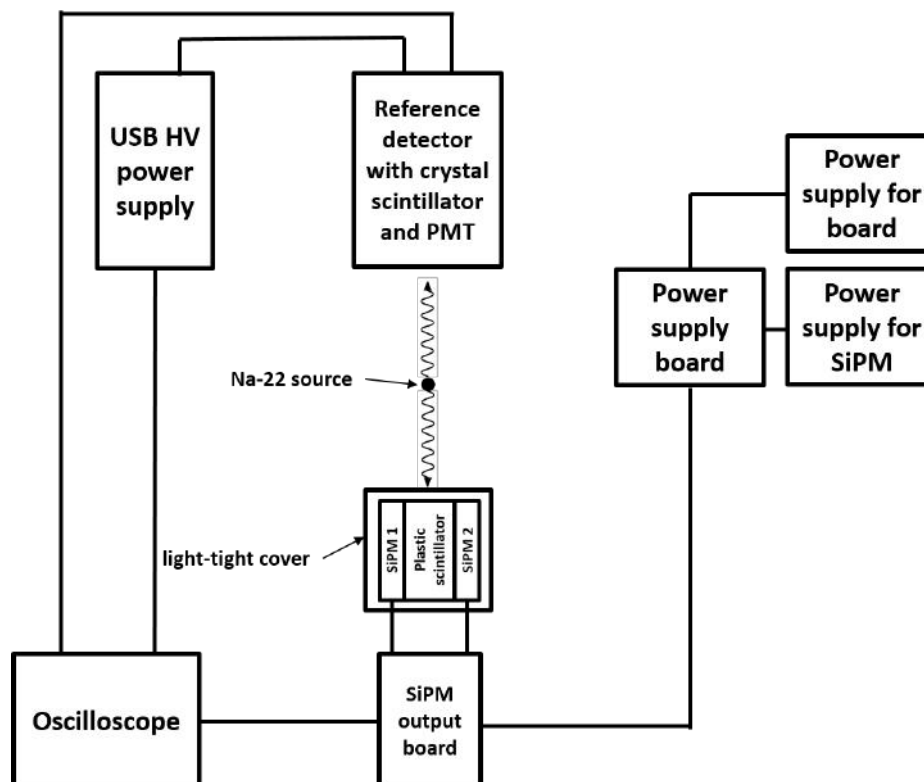
Figure 4.20: Experiment Setup scheme

In this study, a setup was devised to investigate the characteristics of scintillation detectors using Silicon Photo-multipliers (SiPMs). The SiPMs were affixed to a small scintillator measuring $5.75 \times 6.6 \times 8.5$ mm^3 on both sides using an optical gel as an adhesive. To ensure accuracy and prevent external light interference, the entire setup was placed within a light-tight box. One of the SiPMs could be easily replaced, allowing for convenient experimentation. To initiate the measurements,

the setup was irradiated with a collimated gamma beam. A reference detector, which served as a fixed trigger, was positioned on the opposite side of the beam. Initially, tests were conducted without the presence of lead bricks. However, it was observed that the prompt energy levels were significantly higher in this configuration. As a result, the decision was made to prolong the measurement times by using lead bricks. Despite the extended duration, the increased data acquired from annihilation quanta justified this choice.

It is worth noting that a plastic scintillator was not utilized as the reference detector due to its low signal rates, which averaged only one signal per minute. Instead, a crystal scintillator was employed in this capacity.

The experimental setup comprised the following elements:

- Prototype silicon photo-multipliers (SiPMs) manufactured by Hamamatsu (model S13361-5797) were optically connected to a small plastic scintillator measuring $5 \times 5 \times 10 \ mm^3$.

- A reference detector was employed, consisting of an Enhanced Lanthanum Bromide [LaBr3(Ce+Sr)] scintillation crystal sourced from Saint-Gobain. This crystal had dimensions of $50.8 \times 50.8 \ mm^2$ and was optically connected to a detector assembly (R7723-100 ASSY) provided by Hamamatsu.

- Data acquisition and analysis were conducted using the Keysight DSO-S 404A oscilloscope.

- A gamma radioactive source containing Na-22 was utilized in the experiments.

- The SiPMs were powered by the Matrix MPS-6003D power supply.

- The SiPM output board was powered by the Keysight E36312A power supply.

- The reference detector was powered by the CAEN USB HV Power Supply DT5471N, set to 1750 V.

- A scintillator with dimensions of $5.75 \times 6.6 \times 8.5 \ mm^3$ was employed, and the tested SiPMs were optically coupled to it using an optical gel.

4.4.3 Measurement procedure

The measurement procedure was as follows:

- In order to measure the timing properties, we implemented the setup depicted in Figure 4.20. The radiation source was positioned between the reference detector, equipped with a crystal scintillator connected to a vacuum tube photo-multiplier (PMT), and a test setup placed between lead blocks to collimate the beam. The PMT was connected to a USB HV power supply, while the SiPMs in the test setup were connected to a SiPM output board to capture the SiPM signals. Both PMT and SiPM signals were acquired using an oscilloscope.

- Since the SiPMs were arranged in a 1×4 matrix configuration, we had four SiPMs on each side of the plastic scintillator. However, for our measurements, we selected only one SiPM from each matrix.

- The trigger condition was set to achieve coincidence within a 20 ns time window between the signal from one of the tested SiPMs and the signal originating from the reference detector. We set the threshold values as low as possible, approximately 10 mV on the SiPMs and the lowest achievable value on the crystal of the reference detector. The testing was conducted using an operational voltage of 56V, which is suitable for the S13361-5797 SiPM model.

- Summary of settings for S13361-5797:
  Coincidence condition: SiPM1 then crystal within time window
  Coincidence time window: 20 ns
  Thresholds: 10 mV on SiPM and as low as possible on crystal
  Supply voltages: 56V (operating voltage)

- The acquired data was saved in the form of signals recorded at fixed time intervals

- Data analysis was performed using version 4 of the framework software [98].
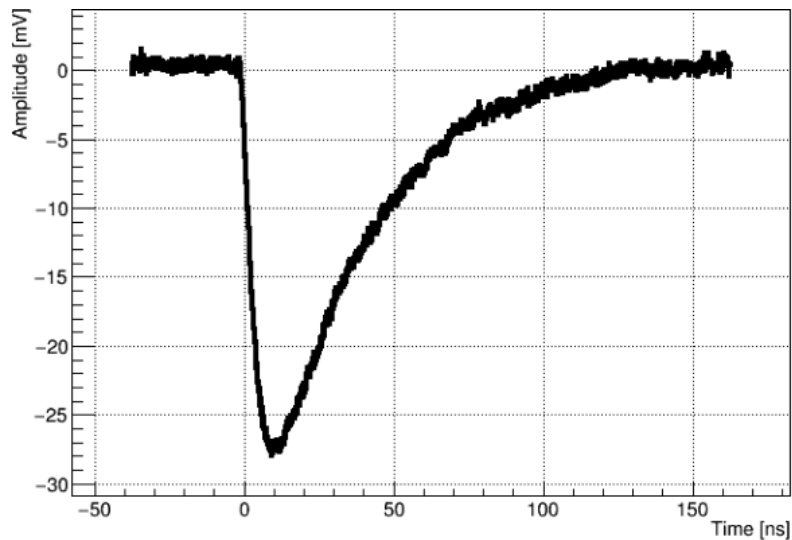
Figure 4.21: Sample signal from S13361-5797, which is used in the J-PEM module.

In order to suppress the influence of scattered photons and prompt gammas in the results, we selected the range between 15mV to 30 mV from the amplitude spectra as presented pictorially in the following figures. The cuts were applied before the calculation of timing properties.
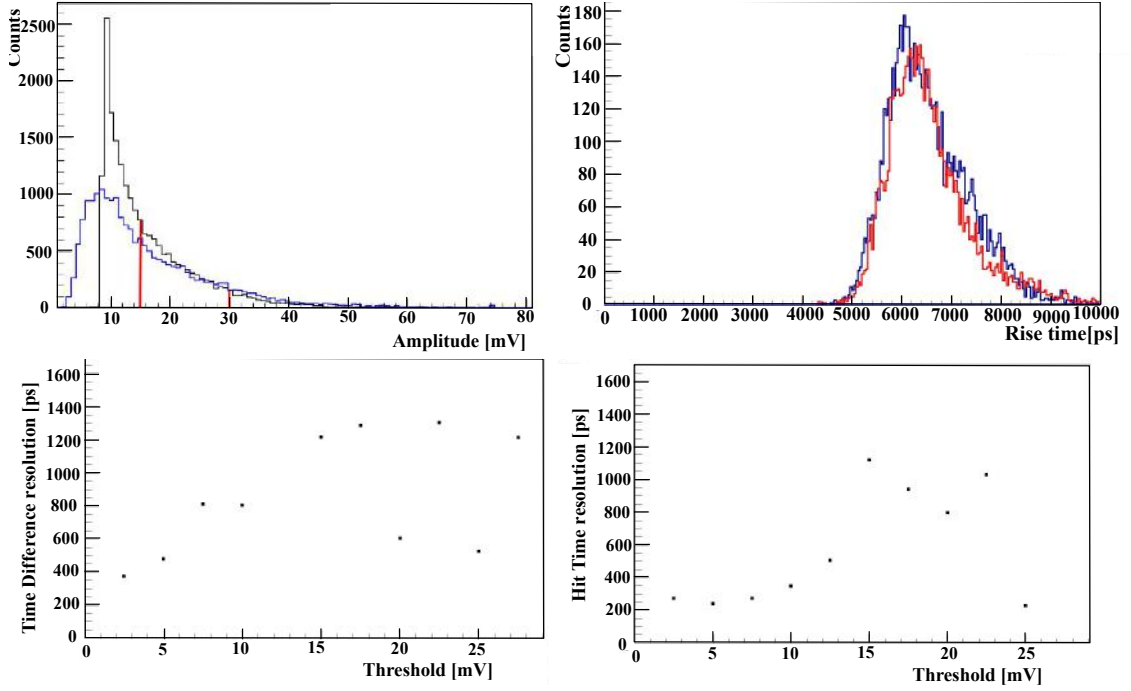
Figure 4.22: The top left figure displays the amplitude spectra obtained from both sides of the scintillator when the S13361-5797 SiPM operates at its operational voltage. Red vertical lines indicate the cuts applied to the amplitude. The top right figure illustrates the rise time spectra from both sides of the scintillator at the operational voltage for the S13361-5797 SiPM. In the bottom left figure, the time resolution is presented for the SiPM at opposite sides of the scintillator. The resolution is depicted as a function of the threshold applied for timing calculation. Finally, the bottom right figure shows the hit time resolution. The resolution is shown as a function of the threshold applied for timing calculation. Only signals with amplitude in the range from 15 mV to 30 mV were considered.

Table 4.4: Timing properties of SiPM amplitudes in the range between 15 mV to 30 mV.

Supply Voltage [V]	Rise [ns]	Amp at CE [mV]	Best threshold [mV]	Time Resolution[ps]	Best threshold[mV]	Hit time[ps]
56.0	6	15	2.5	374	5.0	239

Table 4.4 shows the results of that time resolution with SiPM in the order of 375 ps and the hit time is around 239 ps.

4.4.3.1 Amplification Stage

Once the electrical signals are generated, they go through the amplification stage. At this stage, the amplifier board is responsible for 12 factors of signal amplification, Figure 4.23. Its size is only 22.5 cm^2, with 52 high-frequency amplifiers and 13 connections. To reduce size and energy consumption, MMIC standard amplifiers

are used: ON Semiconductors SMA-3107. So the 1 W of power consumption is 19 mW per amplifier. It has been proven that amplifiers do not heat SiPM - the temperature measured directly on the amplifier is at 37°C level.
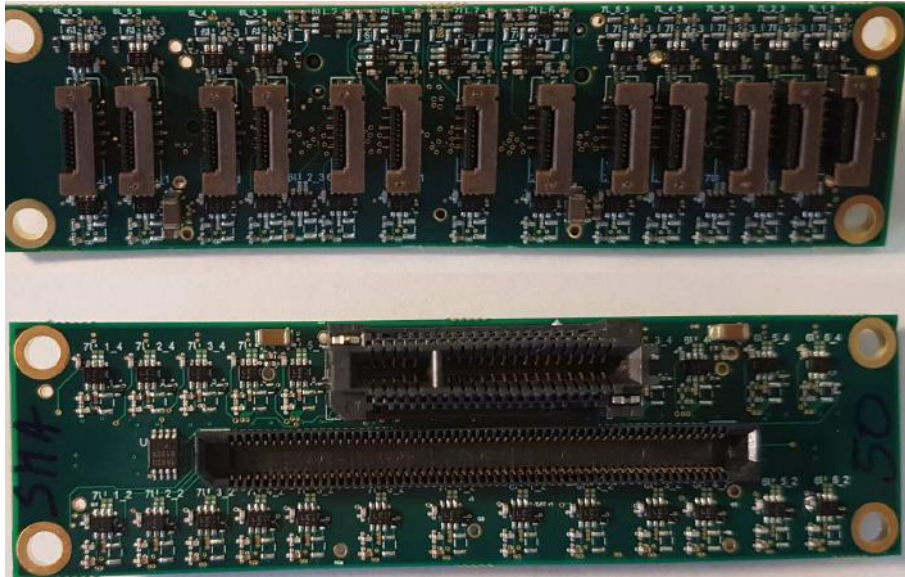
Figure 4.23: Amplification stage

4.4.3.2   Power distribution board

The power distribution board is used to distribute the same voltage (56.5 V) for each SiPM individually in the detector setup, Figure 4.24.

Figure 4.24: Power supply board (left) and Power supply board and FTAB inside the detector.

- **Front-end TDC Acquisition Board (FTAB):** After following the amplification step, signals from each SiPM are supplied to the FTAB, where these

signals are passively split into two - 104 measurement channels for individual thresholds (Thresholds were set at 30 and 70 mV during measurements) and then transformed using the TDC method using Field-Programmable Gate Array (FPGA) [99]. FTAB measures the time of signal arrival and its end, at the
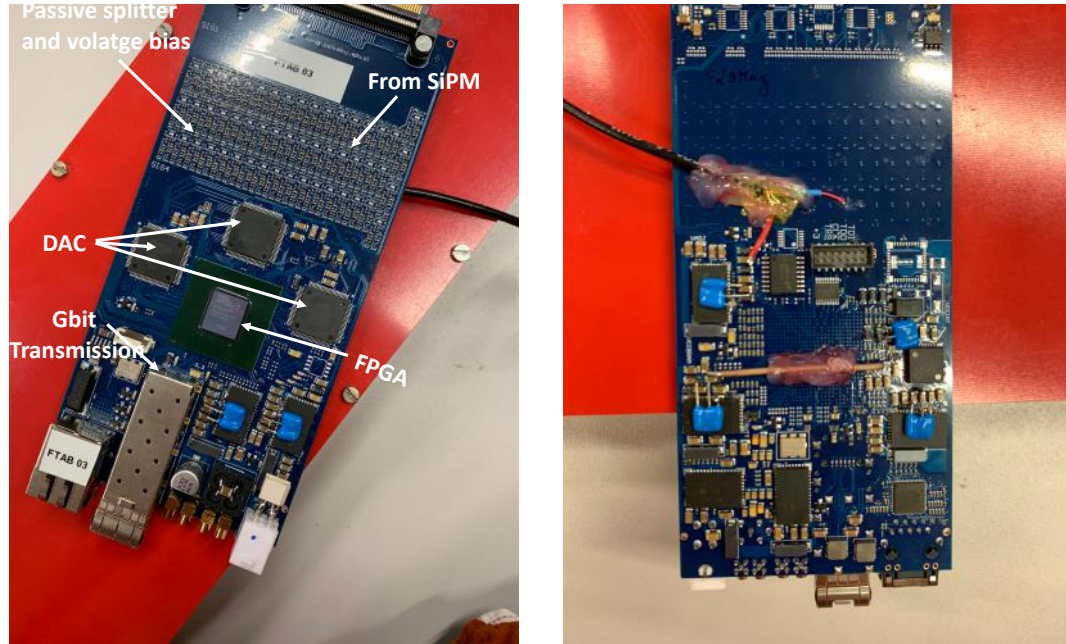
Figure 4.25: Power supply board (left) and Power supply board and FTAB inside the detector.

threshold level, with a very high precision of 30 ps RMS. We have opted for a compact design to place FTAB directly on the detector to avoid cumbersome cabling. It requires 5W of power consumption. Large data yield minimizes FTAB dead time [100].

4.4.3.3 Data acquisition system

A data acquisition system (DAQ or DAS) is a collection of hardware and software components that gather, measure, and analyze data from a variety of sensors or measuring devices. DAQs are extensively employed in scientific research, engineering, and industrial applications where physical phenomena must be measured and analyzed. Sensors or measuring devices, signal conditioning circuitry, an analogue-to-digital converter (ADC), a data storage device, and a computer or data acquisition unit (DAU) for data processing and analysis are the fundamental components of a data acquisition system. Sensors or measuring devices translate physical events such as temperature, pressure, or voltage into electrical signals. The signal conditioning circuitry amplifies, filters, and moulds these signals so that they may be processed by the ADC. The ADC transforms analogue impulses into digital signals that may be processed and saved in a computer or data storage device.

- **Concentrator Board:** A concentrator board is an electrical circuit board that manages and routes communications between various devices or components. It is intended to simplify device interconnection by merging several signals into a single channel or interface. Concentrator boards are utilized

in other applications such as data collection systems to handle signals from various sensors or measuring devices. Signal conditioning, filtering, and amplification may be included to increase signal quality and dependability. The data readout is done in continuous mode, with no hardware trigger. The digitized detector response is saved in data buffers on the Endpoints while waiting for the synchronization message. The messages are generated by the Controller board at a set frequency of 20 kHz and are transmitted to the Endpoints through the Concentrator boards. In response, the Endpoints send the contents of the buffers back to the Concentrators, which aggregate data from many Endpoints, package it in UDP packets, and send it out of the system to storage through the 10 Gigabit Ethernet network.

- **slow control:** Slow control refers to a method that regulates and monitors all aspects of the read-out and DAQ. It takes hardware, firmware, and software to configure and monitor the read-out process's parameters. The gear being monitored or controlled should have a network interface. Using this, we may transmit and receive orders to a single or a group of chosen DAQ components using software on a PC.

- **Field Programmable Gate Array FPGA:** FPGA is an abbreviation for Field-Programmable Gate Array. FPGAs, as opposed to traditional Application-Specific Integrated Circuits (ASICs), are programmable devices that may be programmed and altered by the user to do things like digital signal processing, logic operations, and control functions. This gives many applications more flexibility and a shorter time to market [101]. When compared to other processing devices such as CPUs and GPUs, FPGAs have several benefits. Multi-core CPUs effectively tackle complicated tasks that may be separated into a few functioning threads with mixed instruction sequences. On each thread, GPUs do a high number of the same operations with various data sources. The topology of FPGAs provides exceptional performance for real-time applications and parallel data processing with a restricted arithmetic operation set [101, 102, 103]. The whole Data Acquisition System is built on Field-Programmable Gate Array (FPGA) electronics that allow effective pipeline processing in real time for various data streams. Its design is hierarchical, with the Controller board serving as the central point, Concentrator boards serving as hubs, and Endpoints, which are digitizing boards positioned on detector modules, serving as endpoints. The negative SiPM signal is adjusted for differential FPGA buffers(1024mV). Using an FPGA as a multi-channel TDC and comparator device provides for substantial size and cost reduction. At 50% LUT and 35% FF use, 105 TDC channels could be accommodated. These channels are "manually" placed to achieve great TDC accuracy [101].

This chapter was dedicated to the understanding of concepts used in making J-PEM.

Chapter 5

J-PEM data reconstruction

Simulations play a crucial role in improving the quality and precision of reconstructed images by allowing the testing and evaluation of designs, models, and systems before their real-world implementation. By conducting simulations, potential issues can be identified and addressed, performance can be optimized, and the risks and costs associated with untested ideas or systems can be reduced. Furthermore, simulations provide the opportunity to explore alternative design parameters, configurations, and operating conditions, thereby enhancing the performance of systems and processes. This iterative process helps determine the optimal settings and parameters to improve performance, efficiency, or other desired outcomes. Simulations also enable the prediction of system and process behaviour under different settings or scenarios, allowing for the anticipation of potential issues or opportunities, analysis of the impact of changes, and informed decision-making.

5.1   Materials and methods

5.1.1   Monte carlo simulation

GATE software was utilized for simulation purposes [104]. GATE is an advanced open-source software developed by the international OpenGATE collaboration and targeted to numerical simulations in radiotherapy and medical imaging. The Geant4 package serves as the foundation for GATE. Of all GATE functions, a handful was employed in the thesis and are listed below.

1. Built-in sets (lists) of physics models containing numerous interaction types, each with its own production cut-offs specialized to clinical applications, such as nuclear medicine or proton and ion radiotherapy.

2. Geometry handling tools allow the user to construct setups or support for CT images, which are critical for simulations of therapeutic treatment planning and PET imaging.

3. Actors are scoring tools that interact with the simulation kernel to preserve special information required by the user, for example. Secondary particles or particles that enter/leave the provided volume are scored by the Phase-Space actor. The dose actor contains information about the amount of energy/dose placed in a certain volume.

4. Radiation sources with the use of specific software import and export tools.

5. PET imaging requires a digitizer and coincidence sorter to represent detector energy and spatial resolutions, electronics characteristics (digitizer), combined coincidence windows - prompt and delay - and multiple coincidences handling.

6. A list of coincidences is kept in a ROOT file format, which is easily converted to the file format required by PET reconstruction software programs automatically.

In order to quantify the J-PEM geometry, all the simulations were performed with the GATE software version 8.2 equipped with Geant4 version 10.4.2. The J-PEM detector's entire geometry and the detector material's composition were considered in the simulations as shown in Figure 5.1. The interactions of photons in the scintillators were simulated by GATE. In the simulations, we assumed that the annihilation source is placed in the centre of the detector and that the back-to-back photons (each with an energy of 511 keV) from the $e^+e^- \rightarrow 2\gamma$ annihilation are isotropically emitted. The simulated data were analyzed using the following conditions:

1. The energy deposited by both coincidence photons must be in the 200-380 keV range.

2. The coincidence time window is set to 3 ns. This means checking if the time difference between recorded photons is less than three nanoseconds.

3. The GATE coincidence sorter is used to evaluate and handle lists of coincidences. A default GATE multi-coincidences policy (GATE flag: keep If All Are Goods) was used [104].

4. The 50 cm long strips were artificially discretized into 100 6x24x5 mm^3 crystals because CASToR reconstruction software does not permit TOF modelling along the plastic scintillator strip. Because the TOF resolution along the strip is predicted to be at the level of σ =5 mm, the strip is discretized into 5 mm crystals. [24].

Figure 5.1: The figures illustrate the geometric configuration of the JPEM detector in different orientations. In the diagrams, the WLS (Wavelength Shifting) material is represented in green colour, while the plastic scintillator is depicted in grey. The left figure specifically presents the detector geometry in the x-y cross-section.

The design of J-PEM consists of 26 plastic scintillators and 40 WLS in one module, with dimensions $6 \times 24 \times 500\ mm^3$ and $3 \times 10 \times 100\ mm^3$, respectively (Figure 5.1). For analysis, we only accept events with exactly two interactions and select events for which energy loss is larger than a given threshold value.

5.1.2 Image Reconstruction

Image reconstruction is the process of producing an image from raw data received by an imaging device [105]. It is a fundamental method utilized in many disciplines of science and technology, including medical imaging, remote sensing, and non-destructive testing. Image reconstruction is used in medical imaging to generate 2D or 3D representations of the interior structure of the human body from data collected by imaging modalities such as X-ray computed tomography (CT), magnetic resonance imaging (MRI), or positron emission tomography (PET) [106]. This procedure often incorporates mathematical algorithms that translate raw data into a representation that depicts the image. The algorithms used for image reconstruction can be broadly classified as analytical or iterative [107]. Analytical methods, such as the filter back projection (FBP) method used in CT, use mathematical formulas that directly relate the raw data to the image. On the other hand, iterative methods use a trial-and-error approach to iteratively refine an initial estimate of the image until it satisfies certain criteria, such as minimizing the difference between the raw data and the estimated data [107].

In the case of PEM, the idea of image reconstruction generally involves creating a 3D image of the distribution of a radioactive tracer in the body. A radiotracer must be injected into the patient for PET or PEM imaging. This radiotracer generates positrons that collide with the electrons present in the patient's body to create two back-to-back annihilation photons that travel in opposing directions to each other. These photons are detected by two heads detector in the case of PEM, which are placed above and below the breast of the patient. If two photons are detected in a short time window (the prompt window), the detection is called a coincidence event. And the line connecting the two detectors that detect the photons is called the line of response (LOR). With the aid of a mathematical algorithm, data from several LORs are combined to create a 3D representation of the distribution of annihilation points in the body, as shown in Figure 5.2. The algorithm uses the information (such as data) to predict how the radiotracer will be distributed throughout the body, represented as a 3D voxel picture. Attenuation correction is also performed to compensate for the attenuation of the gamma rays as they pass through different tissues in the body. This is important to ensure that the PEM data accurately reflect the tracer distribution in the body.

5.1.3 Maximum Likelihood Estimation Method

Fully 3D measurements require more storage of data. As a result, reconstruction becomes more computationally intensive, and the solution is to use iterative methods such as the MLEM [109, 110]. The maximum likelihood estimation method (MLEM) is a statistical method for estimating the parameters of a probability distribution given a collection of observed data. The MLEM approach assumes that a probability distribution with unknown parameters creates the observed data. The
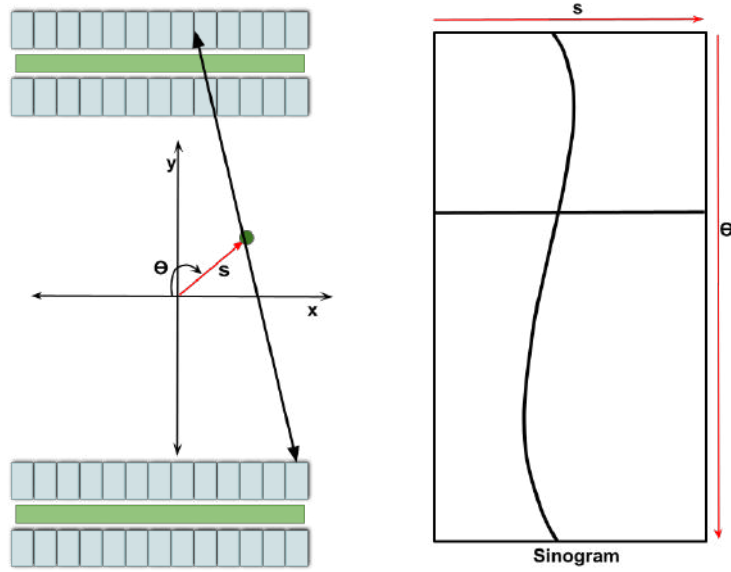
Figure 5.2: (Left) Schematic diagram of J-PEM. Two gamma rays emitted as a result of positron annihilation are detected by two detectors. The lines connecting the detectors (LOR) are described by coordinates (s, θ) and (Right) representation of a point of annihilation shown as a green dot in the image space on the sinogram. (adapted from [108])

goal is to determine the parameter values that maximize the likelihood of detecting the data. The diagram in Figure 5.3 shows the basic procedure for using an iterative algorithm. The initial estimate of the image in an iterative algorithm is usually
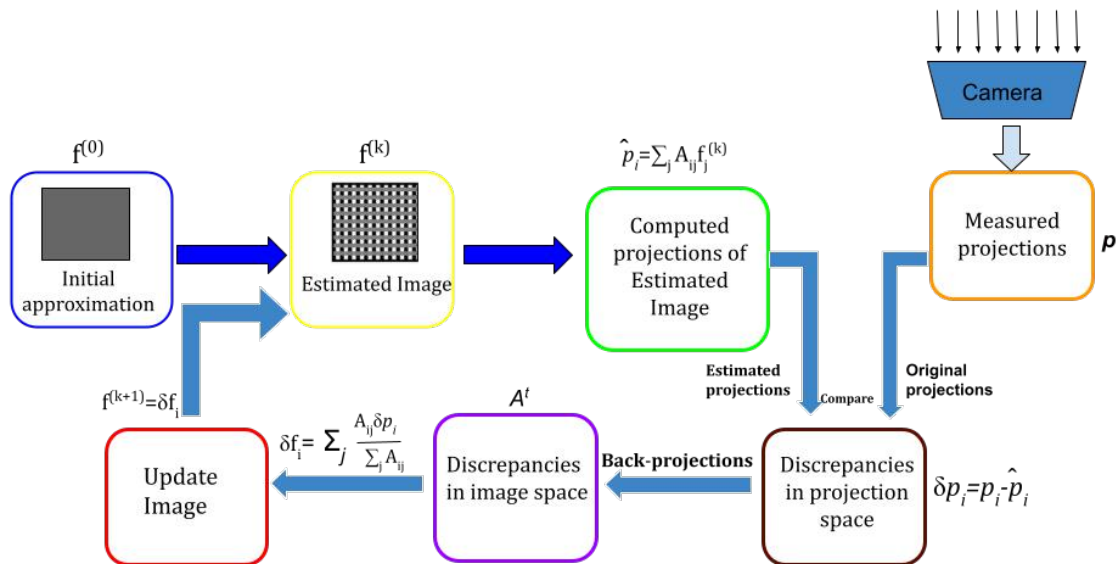
Figure 5.3: The provided figure depicts the flow chart of the iterative image reconstruction method (adopted from [108]).

a uniform distribution [108]. The projections are computed from the image and compared with the measured projections. Suppose there is a difference between the estimated and measured projections. In that case, corrections are made to improve the estimated image, and a new iteration is performed to assess the convergence

between the estimated and measured projections. Iterations are continued until a reasonable agreement between the two sets of projections is achieved. The iterative equation describes the MLEM algorithm for sinogram data as follows [111, 112]:

$$\lambda_j^{k+1} = \frac{\lambda_j^k}{\sum_i^m C_{ij}} \sum_i^m C_{ij} \frac{C_{ij}}{\sum_j^m C_{ij}\lambda_j^k}$$

λ_j^k – the value of the reconstructed image at the pixel $'j'$ for the $'k'$- th iteration,
k - iteration number,
j - pixel number,
i - the bin number of the projection,
C_{ij} – the probability of detecting emission from the pixel $'j''$ in bin $'i'$ of the projection.

The sum over $'j'$ represents the forward projection in the context being discussed. The sum over $'i'$ in the numerator represents the back projection of the ratio between the measured and estimated data. The sum over $'i'$ in the denominator corresponds to the scanner's sensitivity for voxel $'j'$. The sensitivity map determines the probability that gamma quanta of 511 keV emitted from voxel $'j'$ will be detected as a coincidence by the J-PEM scanner.

For several reasons, iterative image reconstruction approaches are frequently considered superior to the filter back projection method. First, compared to filtered back projection, iterative approaches can handle noisy and incomplete data better. This is because iterative approaches utilize regularization techniques to generate a more accurate image while considering the statistical characteristics of the noise in the data. Contrarily, when the input data is noisy or lacking, filter back projection can result in artefacts and errors in the rebuilt picture. Second, iterative techniques can provide pictures with higher spatial resolution and better contrast compared to filter back projection. This is because iterative algorithms develop results using previous knowledge about the picture, such as its smoothness or sparsity, to produce a sharper and more detailed image. Lastly, Iterative techniques can integrate extra data into the reconstruction process, such as the geometry of the imaging system or the properties of the object being imaged. In contrast, filter back projection, which assumes that attenuation coefficients are distributed uniformly throughout the object being imaged, can result in more accurate and exact reconstructions.

5.1.4   J-PEM data reconstruction

5.1.4.1   Reconstruction software

CASToR is an open-source project dedicated to the reconstruction of 4D transmission (CT) and emission (PET and SPECT) tomographic data [113]. The CASToR project's goal is to provide a user-friendly framework that provides basic image reconstruction capabilities for non-expert users as well as more complex tools for reconstruction professionals and developers. Under the CASToR framework, new reconstruction algorithms, projectors, dynamic data modelling, kinetic models, and other features might be implemented. Because of the generic nature of the CASToR software and the flexibility in the selection of the input data file format, the user must pre-compute and incorporate all information required for the reconstruction: list-mode or histogram data format, normalization, attenuation correction, scatter

correction, random correction, and so on. CASToR has the benefit of being able to run in multithread and multi-computer modes. In this dissertation, CASToR version 2.0.3 was employed.
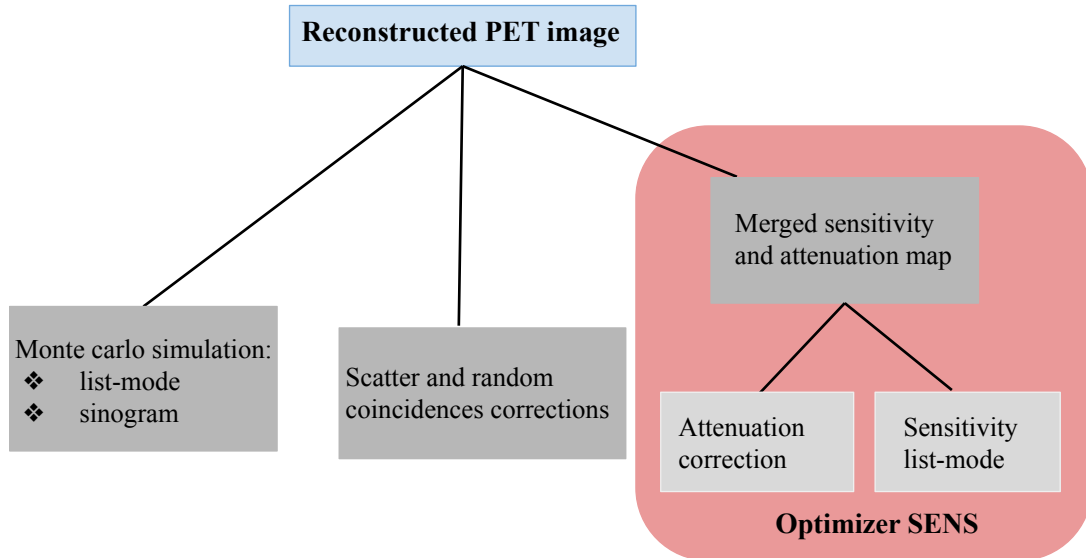
Figure 5.4: The procedure for reconstructing PET scans using the CASToR program (adopted from [114]).

Figure 5.4, depicts a schematic method for PET data reconstruction using CASToR. Coincidence data might be presented in either list or sinogram mode. In Monte Carlo simulations using GATE, developers provide a coincidence list converter from GATE's ROOT file format to the CASToR format. Nevertheless, the user must compute the correction factors (attenuation, normalization, sensitivity, scatter coincidences, random coincidences) for the PET reconstruction. Preferably, all modifications should be made individually for each LOR [113]. With the official version of CASToR ver.2.0.3, there is no option to submit the sensitivity and attenuation adjustments as a map with the values supplied for each voxel at the same time. CASToR will not calculate correction factors for each LOR. In the given methodology, sensitivity maps indicate the voxel-wise likelihood that back-to-back 511 keV gamma quanta will be recognized as a coincidence with the J-PEM scanner. If the sensitivity map is given, the attenuation correction map cannot be included in the reconstruction. If the attenuation correction map is given, the scanner sensitivity map is produced internally by the CASToR program using just the geometrical acceptance. The estimate is true in crystal scintillators with high gamma quanta detection efficiency, such as LSO and BGO. The sensitivity map computation using CASToR is not valid for J-PEM scanners because plastic scintillators are large, and the probable pathway of contact inside the strip is longer for highly oblique planes. As a result, the probability of energy deposition increases considerably [97] in comparison to the direct planes. To address this J-PEM-specific issue, CASToR developers shared the dedicated CASToR functionality (-opti SENS), which allows merging the attenuation correction map with sensitivity correction information delivered in the list-mode format into a single map containing both attenuation and sensitivity corrections. Because the full capability of the J-PEM system was not

available at the time of thesis preparation, normalization correction could not be included in the reconstruction. It was, however, replaced by the approach of sensitivity correction. Only the MLEM and TOF-MLEM reconstruction methods are available in CASToR for list-mode reconstruction, and these were employed in the thesis. In reconstructing the PET data, the combined sensitivity and attenuation map is forward projected via CASToR. The resulting system matrix H is then utilized for image reconstruction.

5.1.4.2 Reconstruction workflow

Early experimental testing of the J-PEM system revealed that the predicted TOF resolution along the LOR is around 500 ps, and this value was utilized for reconstruction. Unless otherwise stated, the reconstruction was carried out using true and scatter coincidences. The data were reconstructed using the Siddon projector [115] and the list-mode TOF-MLEM method. The reconstruction FOV was $32 \times 36 \times 200$ mm^3. The voxel size was set to $2.4 \times 2.4 \times 2.4$ mm^3 for all setups. The voxel size of the attenuation and merged sensitivity and attenuation maps was the same as the reconstruction FOV. During and after the image reconstruction process, there were no filtering and smoothing applied. Scatter and random corrections were not examined or included into the reconstruction framework given in this study.

5.1.5 Sensitivity correction

The sensitivity of a PET or PEM imaging system can vary across the field of view due to various factors, including detector efficiency, attenuation of photons by the patient's body, and scatter of photons inside the patient's body. These sensitivity differences might cause distortions and inconsistencies in the system's images, affecting the accuracy and reliability of diagnosis and treatment plans. Sensitivity correction approaches try to adjust for these differences in sensitivity by estimating or measuring the imaging system's sensitivity profile and adding a correction factor to the obtained data. The acquisition of a blank scan, which entails collecting a picture with no radiotracer present, is a typical approach for sensitivity correction. The blank scan can determine the imaging system's sensitivity profile and mitigate sensitivity non-uniformity [114].

A further Monte Carlo simulation is required to acquire the sensitivity list mode. The sensitivity list mode is a list of true coincidences obtained from a water phantom detected throughout the whole FOV. Scattered and random coincidences are discarded since the scanner's sensitivity is independent of the scanned item. However, plastic scintillators used in J-PEM have low efficiency for detecting Compton scattering events (the efficiency is equal to 0.1 for a 24 mm thick scintillator and a photon energy threshold of 200 keV), Monte Carlo simulations require high statistics of the primary particles to register all possible LORs. As a result, another technique was suggested. To achieve sensitivity list mode, simulations in the water phantom are traditionally performed to enhance the frequency of true coincidences and lower the simulation length. In this scenario, the water phantom was replaced with an air phantom. The entire FOV was covered by the cuboid air phantom (dimension). The phantom was virtually filled with 10^{11} back-to-back 511 keV gamma quanta events.

5.1.6 Attenuation correction

Attenuation correction includes modelling radiation attenuation as it goes through a patient's body to adjust for this effect in the images. This is especially relevant in PET imaging, where the absorption and scattering of radiation in the patient's body can cause image abnormalities and inaccuracies. The attenuation coefficient affects the simulated air and water phantoms attenuation correction. For 511 keV photons in air and water, μ is equal to 0.0005 cm^{-1} and 0.1 cm^{-1} [116]. The resultant attenuation map for the water phantom is shown in Figure 5.5.
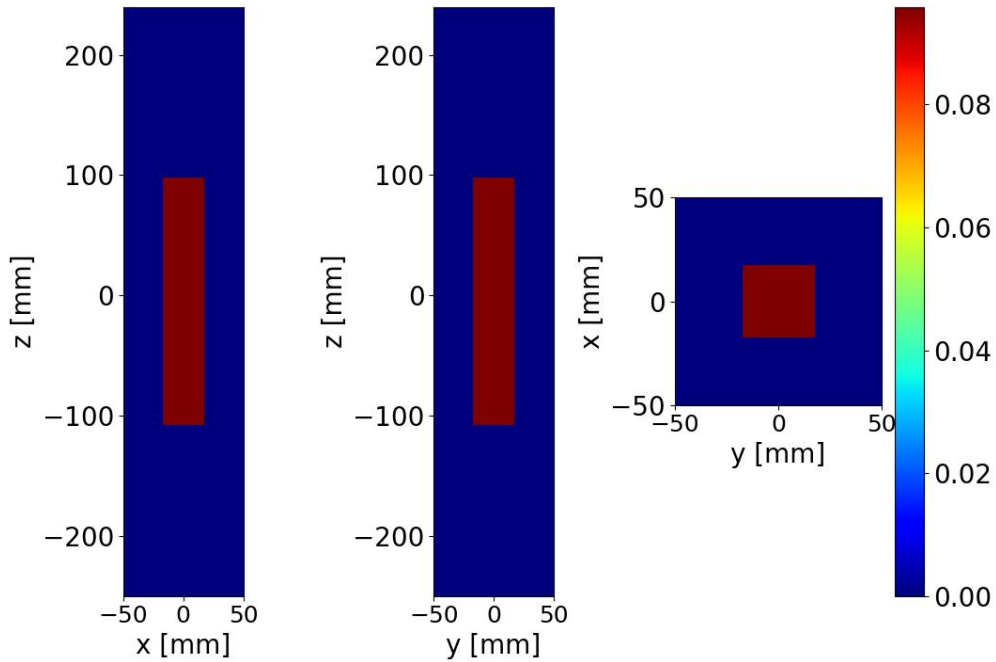
Figure 5.5: The attenuation map of the water phantom was visualized in sagittal (left), coronal (middle) and transverse (right) views, as depicted in the left, centre, and right panels, respectively.

5.1.7 Merged sensitivity and attenuation map

To obtain accurate images in Positron Emission Mammography (PEM) scanning, it is essential to consider the sensitivity of the detectors and the attenuation of gamma rays as they pass through the patient's body. The attenuation map represents the degree of absorption or scattering of gamma rays in different tissues, while the sensitivity map indicates the efficiency of each detector in detecting gamma rays of varying energies. These two maps are combined into a single image to account for these effects.A software algorithm is typically employed to integrate the spatial distribution of sensitivity and attenuation values. By using the merged image, the raw PET data is adjusted to accurately represent the patient's anatomy, accounting for sensitivity and attenuation effects. A specific reconstruction technique called SENS optimizer is utilized to incorporate the sensitivity and attenuation maps. Although this optimizer is not included in the official release of the CASToR project, the

creators have kindly shared it with the J-PET cooperation. Originally designed to generate a sensitivity map from a phantom acquisition with uniformly distributed activity, such as a uniform cylinder or cuboid encompassing the entire field of view (FOV), the SENS optimizer can also accommodate non-uniform phantoms and patient attenuation maps.

For reconstruction, the SENS optimizer is employed with a single iteration and does not utilize Time-of-Flight (TOF) information. Calibration of the final map is necessary. The combined sensitivity and attenuation map is generated whenever there is a change in the attenuation map, such as when a new object is scanned. The sensitivity list mode remains the same for any J-PEM scanning setup. Due to the large number of coincidences that need to be examined, the reconstruction process can be time-consuming.

5.1.7.1 Calibration factor of the merged sensitivity and attenuation map

The calibration of the reconstructed merged sensitivity and attenuation map is crucial. When the map is not calibrated, it exhibits abnormally high levels of activity, which can reach magnitudes on the order of 10^6 if a large number of coincidences are registered. Conversely, the reconstructed PEM (Positron Emission Mammography) images display extremely low voxel values, typically on the order of 10^{-11}. To address this, the merged sensitivity and attenuation map needs to undergo correction. The most straightforward approach is to determine a voxel-wise calibration factor through simulations. A phantom with uniformly dispersed known activity is simulated, and an image of the phantom is generated. The calibration factor is then calculated as the ratio of the mean activity in the reconstructed PET image to the known simulation activity within the same region of interest (ROI). The entire phantom region is utilized as the ROI for estimating the calibration factor.

Considering a total of 15,680 voxels and a known simulated number of 10^{11} back-to-back quanta, the calculated known simulated number of annihilations is 6377551 per voxel (10^{11} divided by 15680). The obtained calibration factor is subsequently applied voxel by voxel to the merged sensitivity and attenuation map. It is important to note that calibration should be performed for each specific J-PEM setup configuration, but it does not need to be repeated unless a new attenuation map is introduced.

5.1.8 J-PEM image reconstruction

The MLEM technique with 30 iterations was employed using the CASToR software to reconstruct J-PEM data. The reconstruction process incorporated a Time-of-Flight (TOF) setting of 500 ps and a voxel size of 2.4×2.4×2.4 mm^3. Both attenuation and sensitivity correction methods were applied to account for the effects of attenuation and the varying detection efficiency of the scanner.

5.1.9 Spatial resolution

The spatial resolution of a detector refers to its ability to distinguish between two distinct points in an image after the reconstruction process. To measure the spatial resolution, point sources are imaged in an air environment, and images are reconstructed without applying any smoothing techniques. The purpose of this study is to
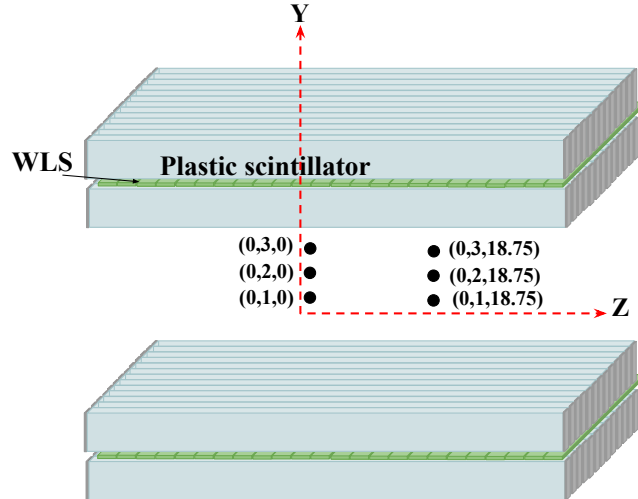
Figure 5.6: The figures depict the arrangement of six-point sources(black dots)within the J-PEM detector.

evaluate the widths of the reconstructed images, which are represented by the point spread functions (PSF) of various radioactive sources. The width of a point spread function is quantified by its full width at half maximum(FWHM) and full width at tenth maximum amplitude. These parameters provide valuable information about the level of detail and precision that can be achieved in the reconstructed images. (Figure 5.6) shows the placement of all six sources used in the simulations.

5.2 Results

5.2.1 Sensitivity maps

The sensitivity map was generated by recording the number of true coincidences obtained from a phantom emitting uniformly distributed 10^{11} primary back-to-back gamma quanta, encompassing the entire field of view (FOV). To visualize the sensitivity distribution across the FOV, sensitivity maps were plotted and presented in Figure 5.7. These maps provide a visual representation of the varying sensitivity levels throughout the imaging system. They offer valuable insights into the regions where the system most responds to the detected gamma quanta.

5.2.2 Merged sensitivity and attenuation map

An example of the calculated, non-calibrated merged sensitivity and attenuation map is depicted in Figure 5.8. The calibration factor for the merged sensitivity and attenuation map is determined using the procedure outlined in section 5.1.7. It is important to note that all other merged sensitivity and attenuation maps presented in the thesis have been calibrated and include the appropriate calibration factor to convert numbers of events (counts) to activity values.

The merged sensitivity and attenuation maps may exhibit higher voxel values outside the phantom than inside the phantom due to the lower linear attenuation
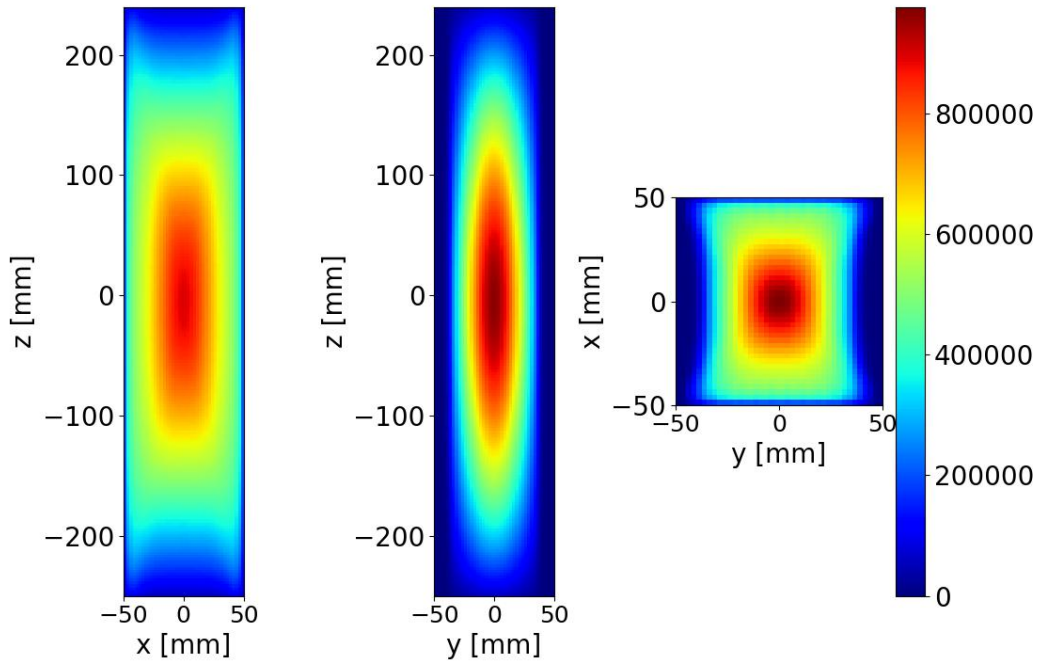
Figure 5.7: Reconstructed sensitivity map of J-PEM, in all three directions sagittal (left), coronal (middle) and transverse (right) is presented.
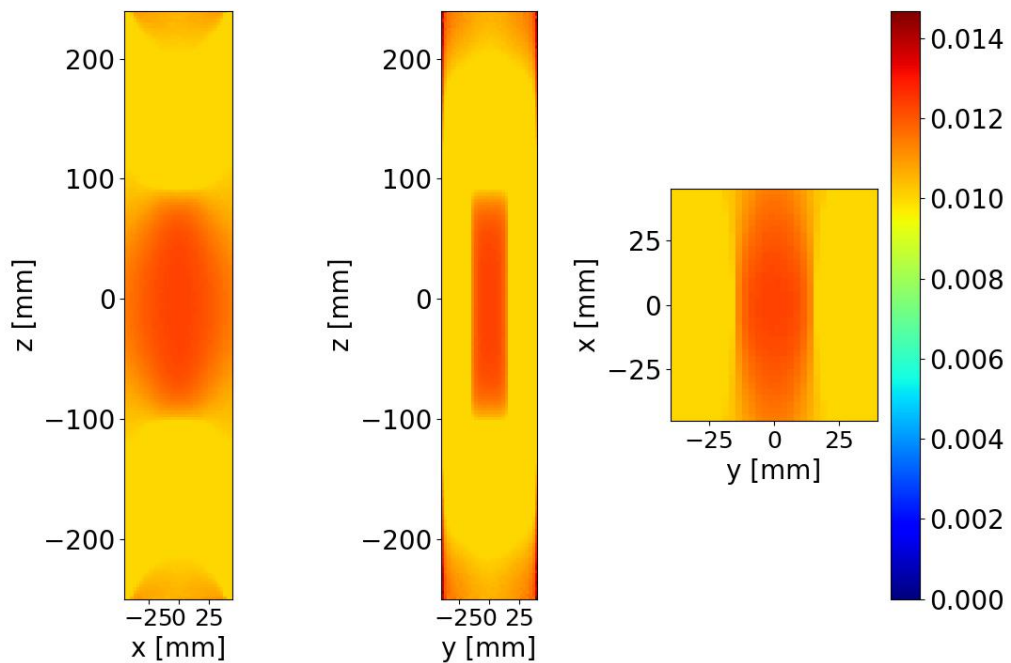
Figure 5.8: The non-calibrated merged sensitivity and attenuation map of the water phantom for the J-PEM configuration is displayed in all three directions sagittal (left), coronal (middle) and transverse (right).

coefficient of air relative to water. These varying voxel values result from the intrinsic properties of different materials. Merging attenuation and sensitivity correction is a time-consuming task that requires careful consideration. To ensure the accurate reconstruction of actual PET images, it is necessary to calibrate the merged sensitivity and attenuation maps as discussed in Section 5.4.3.1.

5.2.3 Reconstructed image

The quantification of the spatial resolution of the reconstructed image is accomplished through the utilization of the point spread function. To assess the point spread function (PSF), a simulation was conducted using six-point sources positioned at specific coordinates, each simulated with 10^{11} MBq annihilations. The positions of these point sources were precisely defined as (0,1,0), (0,2,0), (0,3,0), (0,1,18.75), (0,2,18.75), and (0,3,18.75). The full width at half maximum (FWHM) was calculated as a measure of spatial resolution. The reconstructed image clearly presents the six sources as distinct and well-separated entities, as depicted in Figure 5.9.

It is important to acknowledge a limitation in this evaluation, namely, the absence of additional smearing introduced during the simulation. This limitation could potentially impact the PSF and overall image quality. Despite this constraint, the reconstructed image provides a clear representation of the individual point sources and their spatial distribution.
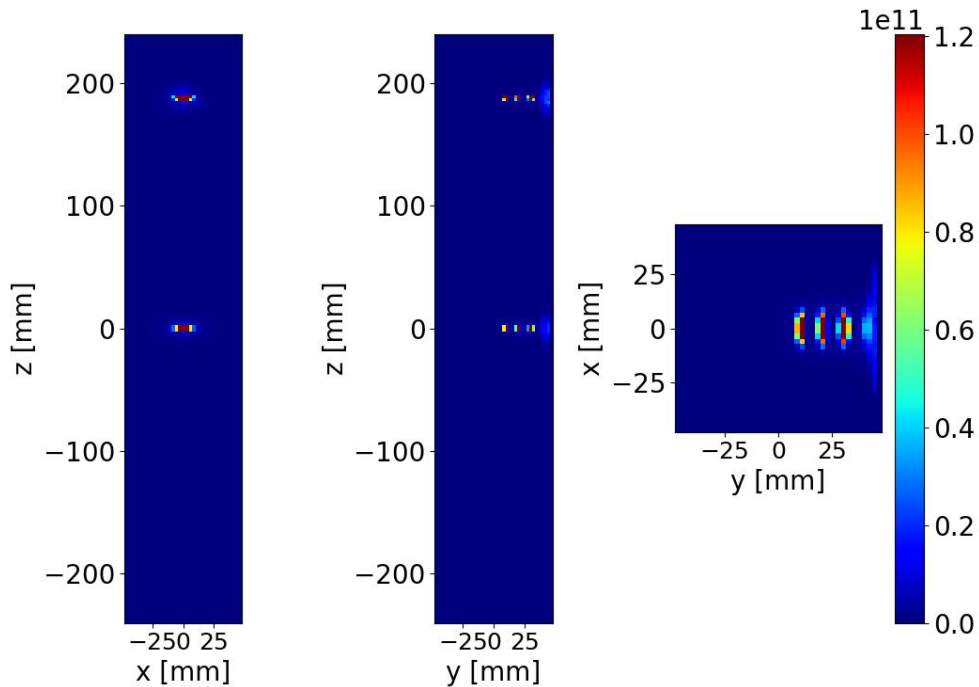
Figure 5.9: Reconstructed J-PEM images of the six-point sources for J-PEM configuration in all three directions sagittal (left), coronal (middle) and transverse (right) is presented.

5.2.4 Point spread function

PSF was computed iteratively for 30 iterations in three directions: axial (y-axis), coronal(x-axis), and sagittal(z-axis). Results were generated to investigate the relationship between the number of iterations and the FWHM in each direction, shown in Figure 5.10.

In the x-axis direction, it was observed that increasing the number of iterations led to a significant reduction in the value of FWHM, suggesting the achievable resolution in this x direction to be approximately 10 mm (Figure 5.10a). It is important to note that the obtained results in this direction were comparatively poorer due to the geometric constraints of the J-PEM setup. Similarly, in both the y-axis and z-axis directions, the FWHM values demonstrated a decreasing trend as the number of iterations increased (Figure 5.10b andFigure 5.10c). This indicates an improvement in spatial resolution in these directions. The achievable resolution along the y-axis and z-axis was estimated to be approximately 4 mm. These findings highlight the effectiveness of the iterative reconstruction algorithm in enhancing the spatial resolution of the reconstructed images along the y-axis and z-axis.

(a)

(b)

(c)
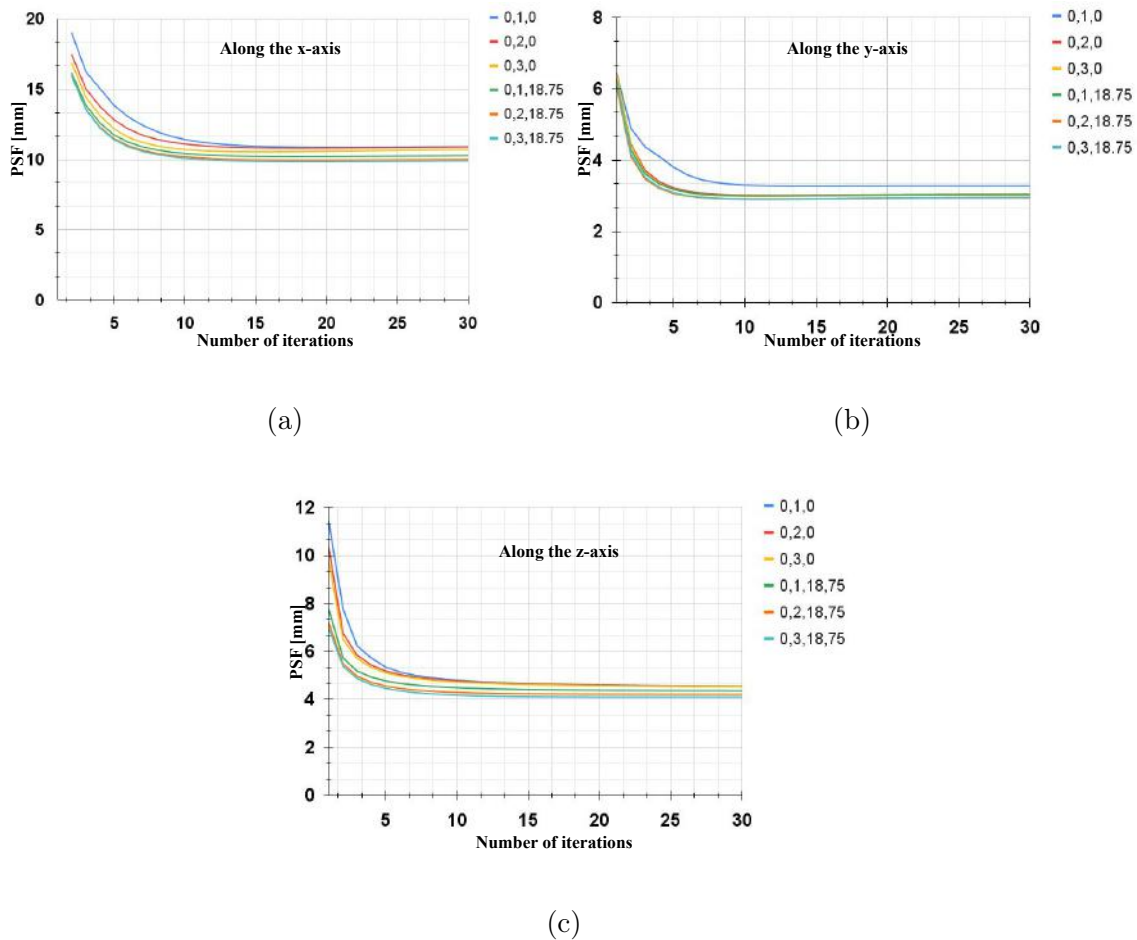
Figure 5.10: Distribution of FWHM over the number of iterations in the three directions. The plot exhibited a clear convergence pattern, consistently demonstrating decreased FWHM values as iterations progressed. (a) tangential, (b) radial and (c) axial direction.

These findings underscore the advantages of increasing the number of iterations during the reconstruction process, improving image quality and spatial resolution. The plots visually depict the association between the iteration count and FWHM, providing insights into the convergence behaviour of the algorithm in each directional plane. In conclusion, the point sources were successfully reconstructed using the J-PEM setup. The calculated point spread function (PSF) revealed that the obtained spatial resolution was approximately 4 mm in the sagittal (along z) and coronal directions, while it was 10 mm along the tangential direction (along y). These findings demonstrate the capability of the J-PEM setup to accurately reconstruct and resolve the point sources with a satisfactory level of spatial resolution.

Chapter 6

Experimental test and Data Analysis

Experimental testing and data analysis are critical components of every research study as they offer a systematic strategy for gathering and evaluating data in order to answer research questions or test hypotheses. One can use experimental testing to acquire empirical evidence that supports or refutes their hypothesis. It entails rigorous experiment design, data gathering, and measurement of variables of interest. Data analysis, on the other hand, enables one to make sense of the data they've gathered. It entails applying statistical or other analytical approaches to data to determine patterns, trends, and correlations. Data analysis assists in concluding, making deductions, and providing evidence to support hypotheses or research questions.

6.1   Data taking with J-PEM

The experimental setup shown in Figure 6.1, consisted of:

- A pair of BC-404 scintillators with dimensions $6\times24\times500$ mm^3, wrapped in Vikuiti foil for the reflection of light and Kapton foil for light tightness;

- Four 6 mm by 6 mm size of SiPM, connected at each end of the scintillator via optical gel

- Lead collimator with 4 mm slit width, which could house a 22Na and a stand for the placement of point-like sources;

- Reference detector used for the purposes of tagging 511 keV, which consists of 13 plastic scintillators (same as in J-PEM).

- For the purposes of measurement, the distance between the J-PEM prototype and reference detector was set as 52 cm. The source was centred in all three x,y and z directions with respect to J-PEM.

In order to test the J-PEM module prototype, three different types of measurements were performed:

- Open source measurement was performed by placing the source at three different positions along the z-axis for the time, velocity and time over threshold calibration, as shown in Figure 6.1.
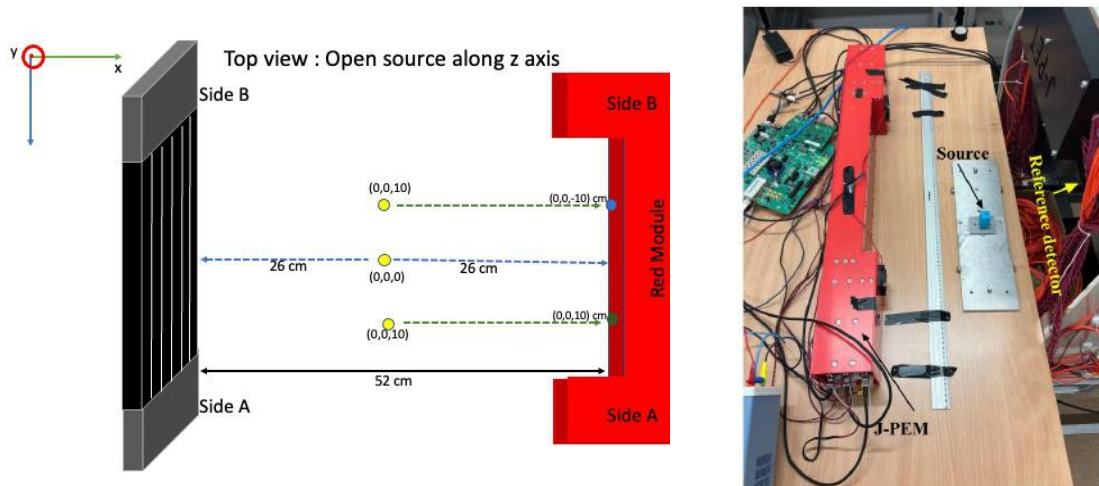
Figure 6.1: (Left) Diagram illustrating the open source measurement configuration. The configuration includes the J-PEM (red module), which comprises two layers of plastic scintillator with a layer of WLS (wavelength shifting) material sandwiched between them. The reference detector (black) is utilized for tagging the 511 keV energy. During the measurement, an open Na-22 source was positioned at the centre of both detectors. (Right) Photograph showcasing the experimental setup used for the measurement

- A scan along the detector for nine different positions along the z-axis with the source inside the collimator was performed to estimate the interaction position of a hit (spatial resolution along the z), as shown in Figure 6.2.
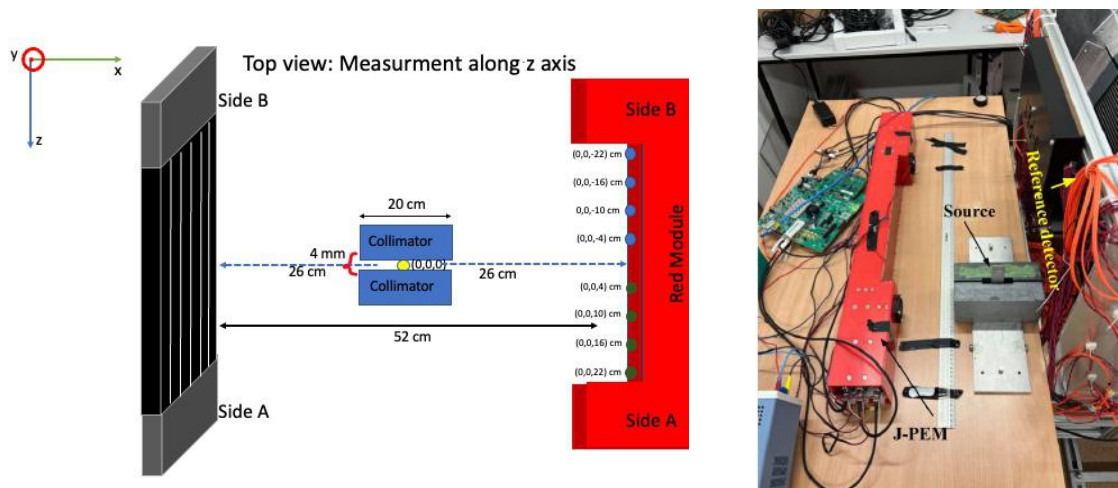
Figure 6.2: (Left) Diagram illustrating the measurement with collimated source. During the measurement, a collimator with a 4 mm slit width was used with a Na-22 source and was positioned at the nine different positions along the J-PEM detector (red module). (Right) Photograph showcasing the experimental setup used for the measurement.

- Last but not least, measurement was done to determine the depth of interaction along the y-axis. And it was done for three different positions, as shown in Figure 6.3.
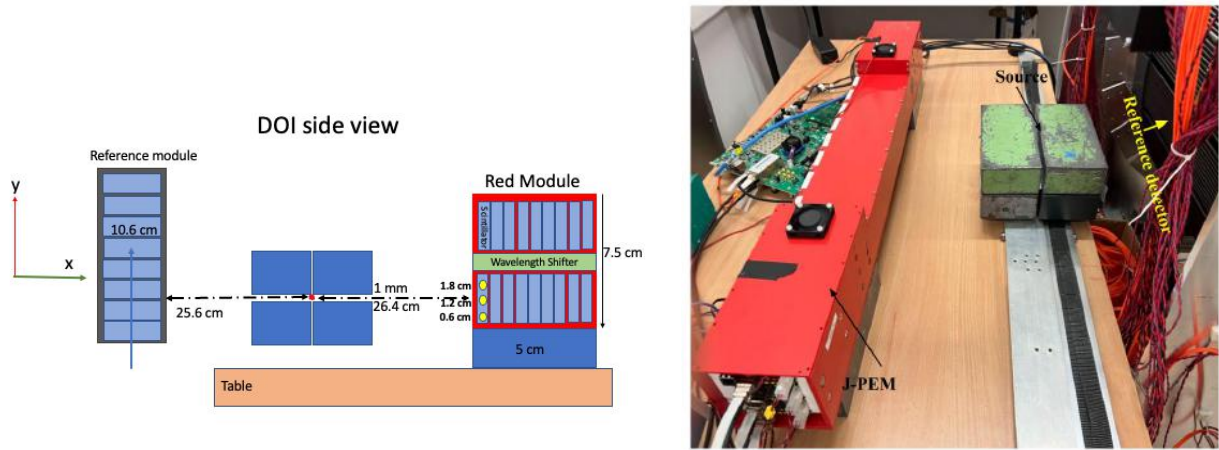
Figure 6.3: (Left) A diagram depicting the depth of interaction measurement using a collimated source is presented. The measurement involved the utilization of a collimator featuring a 1 mm slit width, along with a Na-22 source. The source was positioned at three distinct locations along the y-axis. (Right) Photograph showcasing the experimental setup used for the measurement.

6.1.1 Baseline scan

A baseline scan is a technique that sets a baseline or reference point for noise in the detector at the electronic level. After power-up, the baseline levels of all channels, which differ owing to the complicated manufacturing process, must be synchronized. This is possible because of an inbuilt Digital to Analog Converter (DAC) circuit that permits modifying individual baseline-threshold values to be positioned in the centre of the noise spectrum measured individually for each channel. The strength of the noise and its proximity to the threshold at 0 mV enable the determination of a channel's eligibility for operation.
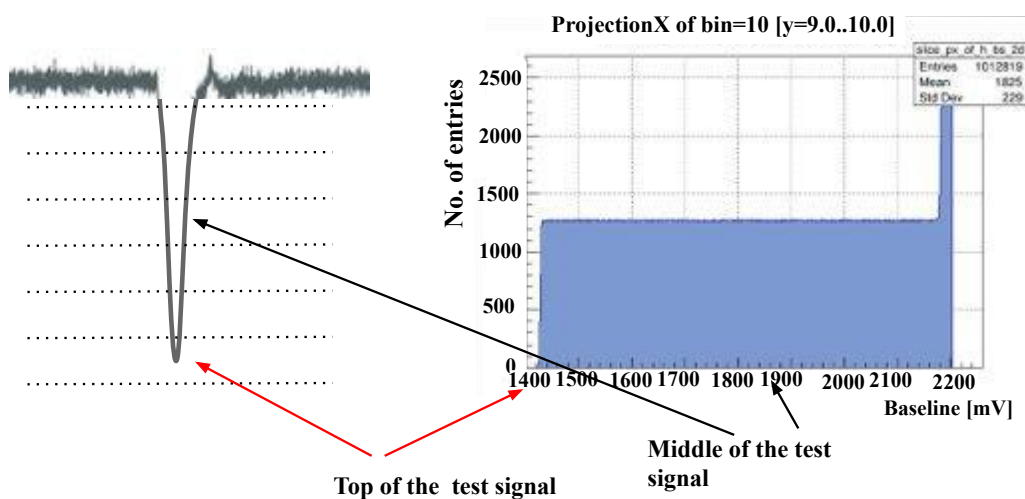
Figure 6.4: This figure shows an example of a baseline scan done for 2mV steps. The baseline signal remains steady until the scan encounters noise, at which point a sudden peak emerges. The red arrow indicates the starting point of the scan, while the black arrow highlights the middle portion of the scan.

The method used to determine such baseline positions is a noise profile scan, in which the baseline or threshold of each channel in the semiconductor is moved and the number of registered output pulses is counted at each step. In this technique, the front-end board (FEB) is connected to the detector, and a common threshold value of 0 mV is established. The baseline locations of each chip channel are adjusted with a 2 mV step within the allowable range of -30 to +30 mV, as shown in Figure 6.4. Counts are counted for each baseline location and channel during the scan. The baseline location is calculated using the mean value of the measured profile of counts. The estimated mean value is subtracted for each channel by the DAC setting. The observed signal count profile has a Gaussian shape. It is used to characterize the noise of separate channels using root mean square (RMS). This scanning approach is extremely beneficial for simultaneously measuring baseline position and noise width from a large number of FEBs.

6.2 J-PEM framework

The data gathered during the measurement was analyzed using the J-PET Framework architecture. It is built on the C++ programming language and the ROOT and Boost libraries [98]. The J-PET Framework software offers comprehensive event recovery from a trigger-less data-gathering system. The J-PET Framework's fundamental premise is the breakdown of analytic chains into a set of standardized modular components. Each module corresponds to a certain computational job, such as a reconstruction technique or a calibration procedure, and has its own set of input and output methods. The processing chain is constructed by registering selected modules in the JPetManager, which synchronises data flow across modules [117, 118]. This approach has several advantages, including the ability to quickly interchange modules and create a processing chain that can be used for different experimental setups. As illustrated in Figure 6.5, a typical Framework processing system is divided into multiple modules, each analysing a collection of data items and combining them into increasingly sophisticated structures.

Starting with a series of raw time-to-digital converter (TDC) data, the technique reconstructs the forms of electric signals from photo-multipliers. After that, on a scintillator strip, pairs of signals corresponding to a single photon hit are recognized and utilized to construct hit objects. Lastly, pairs of hits from a single annihilation event are combined into Event structures, which serve as input to image reconstruction algorithms created for the J-PEM. Each of these processes is executed by a distinct module, allowing for simple procedure exchange in case of a change in the DAQ system.

Furthermore, the framework is ideally suited to developing processes in parallel by leveraging the standardised module structure and established input/output. This feature is especially significant during the prototype phase of the project when the various reconstruction processes are created and evaluated concurrently by different subgroups.

6.2.1 Data reconstruction

For the purpose of the analysis, we used the J-PET Analysis Framework and a set of procedures that were developed for the purposes of analysis of the data from
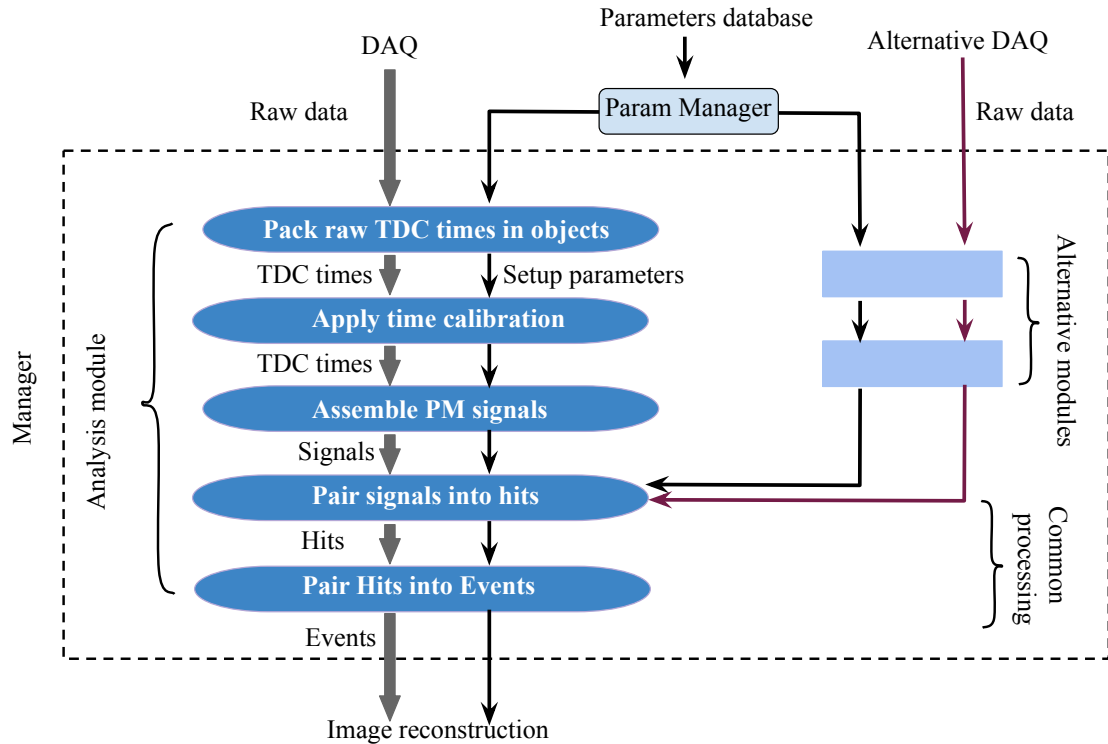
Figure 6.5: An illustrative representation of a data processing chain within the J-PET framework is provided. This chain serves as an example and showcases the various steps involved in processing the data.

the detector with the WLS layer [117]. This dedicated program is an extension of the software used for the analysis of Modular Detector data and is a part of the repository of examples. The workflow is designed to reconstruct step by step the data from the binary level to the form of representation of the physical events. These steps are:

1. Reading of configuration and calibration files to be used during all the analysis steps

2. Reading the input data file (HLD format) and decoding the binary data into DAQ channels timestamps

3. Building SiPM signals

4. Merging SiPM signals to Matrix signals

5. building hits in scintillators and in the WLS layer

6. Creating events - the selection of the hits that depends on the input data type and the goal of the test (i.e back-to-back events, calibrations)

6.2.2   Configuration files

The set of files necessary to analyse the input data consists of the following:

1. Setup configuration file - in `json` format, that describes the positioning of the elements of the detector (scintillating and wavelength shifter strips, silicon photo-multipliers), physical connections between the elements, thus allowing the workflow of the data reconstruction. Two separate files were prepared for the different arrangements of the detector during the measurement:

   a. The J-PEM module layers orthogonal to the table for open source and collimator runs `red_module_setup.open.source.json`

   b. The red module on the side, layers perpendicular to the table for DOI measurement `red_module_setup.doi.json`

2. Additional WLS configuration file in `json`, explicitly marking the connections between SiPM and WLS, positioning along the z-axis of the geometrical centre of SiPMs and WLS strips, percentage of area coverage of WLS by SiPM

   `wls_conf.4.json`

3. Calibration file in `json`, including all constants and offsets that are the result of the calibration procedures and are applied during the data reconstruction

   `red.module.calib.const.offset.json`

4. User options file in `json`, that includes selection options and parameters, adjusted before the run of reconstruction, depending on the type of measurement, calibrations and analysis goal

   `up.red.22.07.json`

6.2.3 Binary data transformation

The input files for the analysis procedure are HLD files, which are binary files in Hades-like format. They are decoded by an external library J-PET Unpacker, incorporated into the Framework executable. The procedure reads the chunks of data marked by headers until the end of the file is reached. Each header describes the length of the data word and the content, subsequently, the following data is decoded: epoch time, reference times, coarse times, fine times and edge types. Each reference time marks a new time slot of 50 μs, represented by a `Time Window` data object, that contains the collection of channel signals - time stamps in the range from 0 to 50 μs, assigned edge type and channel ID. The time of a channel signal is calculated in the following way:

$$t_{\text{CHANNEL}} = t_{\text{REF}} - (t_{\text{COARSE}} * C_{\text{PERIOD}} - t_{\text{FINE}*F_{\text{BIN}}}) \tag{6.1}$$

where C_{PERIOD} is the constant of the coarse time period equal to 2352.941 [ps] and F_{BIN} is the bin width of the fine time measurement equal to 18 [ps]. In general, this procedure step can apply the corrections for TDC non-linearity, but in the case of this experiment, the calibration file was not prepared.

6.2.4 Signal building and merging

Each of the SiPM signals is reconstructed separately based on the data acquired on the channels assigned to the specific photo-multiplier as the registration thresholds.

The reconstruction is performed for all SiPMs - 208 units connected to scintillators and 64 to WLS. The principle of matching the DAQ timestamps into SiPM signals is explained in the left part of Figure 6.6. The right part illustrates the method of calculating the Time-over-Thresholds of the signal, which is a rectangular approximation of the area under the curve based on the time information and values of the thresholds. It is calculated using 6.2. Where, t_1^{TRAIL}, t_2^{TRAIL}, t_1^{LEAD} and t_2^{LEAD} are the time at the leading and trailing edges of the signal for thresholds 1 and 2 (THR1 and THR2).

$$\text{ToT}_{\text{SiPM}} = (t_1^{\text{TRAIL}} - t_1^{\text{LEAD}}) \cdot \text{THR}_1 + (t_2^{\text{TRAIL}} - t_2^{\text{LEAD}}) \cdot (\text{THR}_2 - \text{THR}_1) \quad (6.2)$$
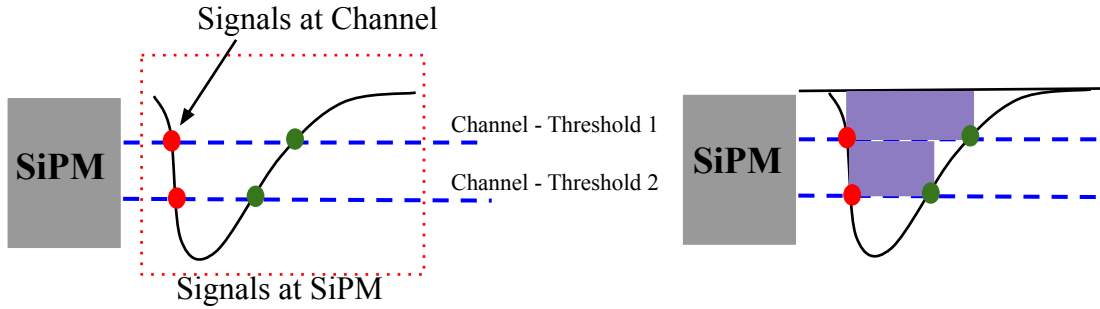
Figure 6.6: Left: illustration of the procedure SiPM signal building. The timestamps on DAQ channels can be of one of two types - leading edge (red circles) when the rising signal crosses the threshold and trailing edge (green circles) when the signal is descending. The first step is to match signals on the same channel: of the two consecutive timestamps, the first is the leading edge and the second is trailing, and the latter arrives no more than 200 ns later than the former. The second step is checking for the coincidence of timestamps on two thresholds, two pairs of signals are saved as a SiPM signal if the module of the time difference of two leading-edge channel signals is no greater than 10 ns. Right side represents a rectangular approximation of the Time-over-Threshold value for the signal. It is calculated for the assembled signals as described by equation 6.2.

Once the signals for separate SiPM are created, the reconstruction proceeds to the step of merging several signals into so-called Matrix signals, as they are registered in coincidence by 1-4 photo-multipliers at the end of the scintillating strip, most probably originating from the same instance of the deposition of the energy, propagating along the material. The algorithm iterates all the SiPM signals in the DAQ slot that are sorted in time, starting from the earliest. The new signal matrix is constructed with at least one SiPM signal and the consecutive ones can be added if they meet the following conditions:

1. Time difference between the first signal and $n - th$ one is smaller than the user-defined time window for matrix signal coincidence $t_n - t_1 < \Delta T_{\text{MTX}}$. In the case of analysis ΔT_{MTX} was set to 10 ns.

2. The matrix position of the SiPM that registered the $n - th$ signal is not the same as any other included so far (1 ... n-1).

71
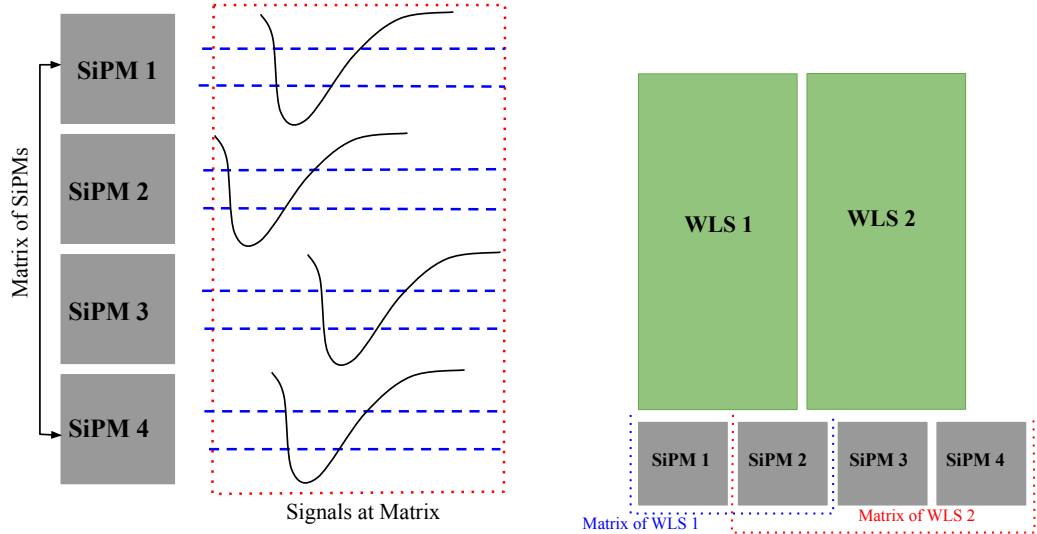
Figure 6.7: Both figures illustrate the process of merging some SiPM signals for the case of a matrix of 4 SiPMs attached to the end of a strip (left part) and in the case of photo multipliers working with wavelength shifters (right part). The definition of a certain matrix at WLS depends on which SiPM is covering the strip, as shown above: matrix 1 includes SiPM id 1 and 2, and matrix 2: SiPM 2, 3 and 4. The definitions of the WLS matrices are included in the configuration files. The procedure of creating Matrix Signals is explained in the text.

6.2.5   Hit matching

As a hit, we define a recorded gamma interaction with the scintillating material based on the three registered signals: from side A and side B of the 50 cm scintillator strip and from the WLS layer, as shown in Figure 6.8. Firstly, the procedure considers A-B signals of the same strip and matches the pairs in 5 ns coincidence $|t_B - t_A| < \Delta T_{AB}$. For the found cases, the following values are calculated:

1. Time of a γ interaction is an average of times of light arriving at each of the two ends of a scintillator strip (t_A and t_B) excluding the total time needed by the light to propagate to the SiPM matrices:

$$t_{hit} = \frac{1}{2}(t_A + t_B) - \frac{L}{2v}, \tag{6.3}$$

Where L denotes the length of the scintillator strip and v is the effective speed of light propagation along the strip.

2. Axial position of the interaction with respect to the centre of the strip is inferred from the difference in light recording times at sides A and B:

$$z_{hit} = \frac{v}{2}(t_B - t_A). \tag{6.4}$$

3. Hit TOT is an average TOT of two signals:

$$\mathrm{TOT} = (\mathrm{TOT_A} + \mathrm{TOT_B})/2 \tag{6.5}$$

As the next step, the algorithm is looking for the time coincidences of reconstructed gamma interactions and WLS signals in 4 ns time window $|t_{\mathrm{hit}} - t_{\mathrm{WLS}}| < \Delta T_{\mathrm{SCIN\text{-}WLS}}$.
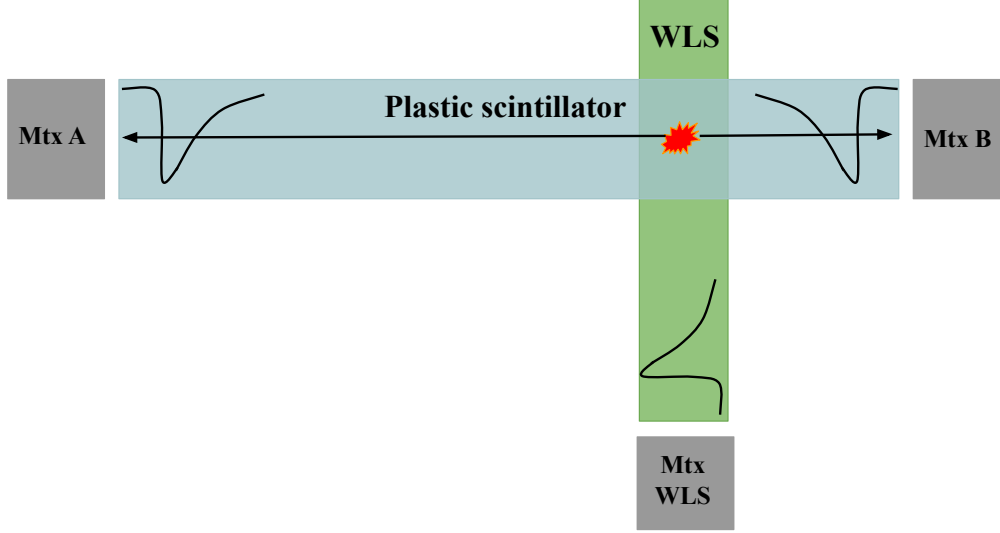
Figure 6.8: The representation of a gamma interaction (red star) in the scintillator (light blue rectangle), the light propagated to its ends. It was registered by matrices of SiPM on sides A and B. The light is also transferred to the WLS strip (green rectangle) and another signal was recorded by the third matrix. The reconstruction procedures look for coincidences of the signals, as described in the text.

6.2.6   Z-axis position using WLS signals

The alternative way of estimating the hit position is to use time and TOT data recorded by SiPMs attached to WLS strips. The following three methods were implemented to test the functionality of wavelength shifters:

1. TOT weights:
$$w_i = \frac{\mathrm{TOT}_{\mathrm{SiPM}_i}}{\sum_i \mathrm{TOT}_{\mathrm{SiPM}_i}}, \quad z = \frac{\sum_i (w_i \cdot z_{\mathrm{SiPM}_i})}{\sum_i w_i}$$

2. TOT weights squared:
$$w_i = \frac{\mathrm{TOT}_{\mathrm{SiPM}_i}}{\sum_i \mathrm{TOT}_{\mathrm{SiPM}_i}}, \quad z = \frac{\sum_i (w_i^2 \cdot z_{\mathrm{SiPM}_i})}{\sum_i w_i^2}$$

3. TOT and coverage weights:
$$w_i = c_{\mathrm{SiPM}_i}^{\mathrm{WLS}} \cdot \frac{\mathrm{TOT}_{\mathrm{SiPM}_i}}{\sum_i \mathrm{TOT}_{\mathrm{SiPM}_i}}, \quad z = \frac{\sum_i (w_i \cdot z_{\mathrm{SiPM}_i})}{\sum_i w_i}$$

In the formulas above z_{SiPM_i} is the fixed position of the centre of the given SiPM that registered the signal; w_i denotes weights, $c_{\mathrm{SiPM}_i}^{\mathrm{WLS}}$ is the percentage of the surface that given SiPM in the matrix covers the WLS. As it is shown in the example in figure 6.7, this number can be different for the same SiPM (i.e. ID 2) depending if whether we are considering the signal reconstructed in WLS ID 1 or 2, as this

SiPM in-equally covers the surface of the strip. These percentages are stored in the configuration file used during the reconstruction procedures.

6.3   J-PEM detector calibration

To determine and correct for offsets caused by delays in signals due to cables and electronics (FEE), calibration was performed using data collected from the irradiation of the scintillator at its centre. The goal was to ensure that the difference in times between signals measured at opposite ends of the strip remains constant (ideally zero):

$$t_A - t_B = t_{offsetAB}, \tag{6.6}$$

The calibration process involved determining the offsets between the time differences measured for each strip in J-PEM and a reference detector, shown in Figure 6.9. This allowed for the calibration of time measurements to account for any discrepancies or delays introduced by the individual strips and ensure accurate timing information across the system.
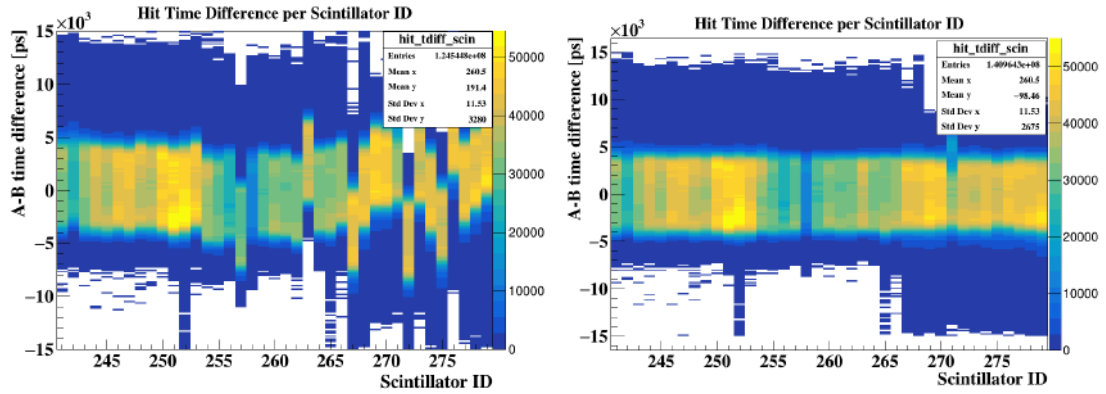
Figure 6.9: The calibration of the scintillator hit time difference, that is, a time offset of the time difference between matrix signal on side B and side A in a given strip. It is based on finding the edges of the spectra and centring the distribution around 0 [ns]. The results are shown for two layers of the red module (strip ID 240-253 and 254-266) and the reference module (ID 267-279). The left part shows the distributions before the calibration and the right - after.

In addition to calibrating the time measurements, another step involved normalizing the Time-Over-Threshold (TOT) for the hits registered in the strips. This normalization aimed to align the Compton and de-excitation edges of all the strips to consistent values of 7ns and 9ns, respectively, as shown in Figure 6.10. After achieving time synchronization between the registered hits in the strips, the analysis proceeds to identify coincidences between signals from strips and WLS. To perform this analysis, we look for an array of intersections between the strips and WLS strips. For each of these cross-sectional areas, time offsets are calculated to determine the relative timing between the corresponding signals. These offsets are normalized around zero to establish a consistent reference point, Figure 6.11. Once the offsets are determined and normalized, the measurements can be further investigated to draw physical conclusions. The series of calibration constants were obtained with additional methods during the analysis of the measurements with the
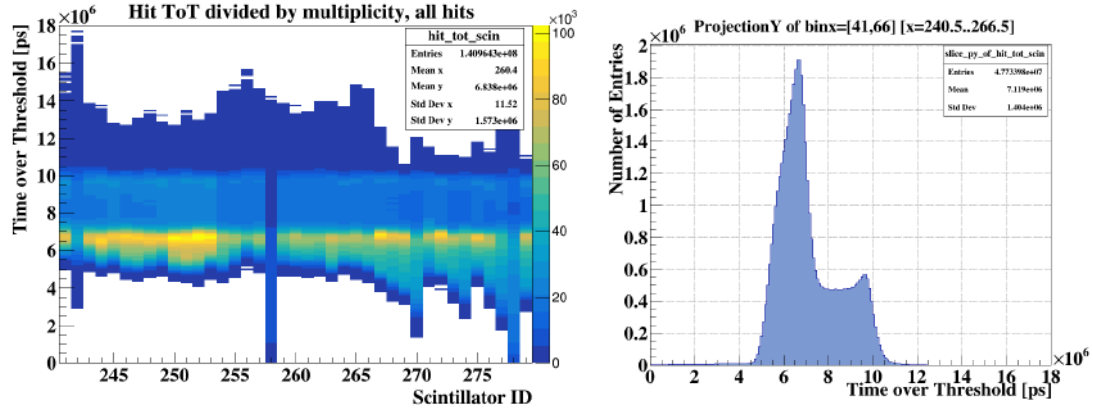
Figure 6.10: Histograms of scintillator hit TOT after normalisation of the SiPM response. The left side shows the results for all the strips in the J-PEM (ID 240-266) and reference layer (ID 267-279). On the right, the projection of all the J-PEM scintillators, showing calibrated TOT with annihilation and de-excitation edges normalised to 7 and 10 [ns·mV], respectively.
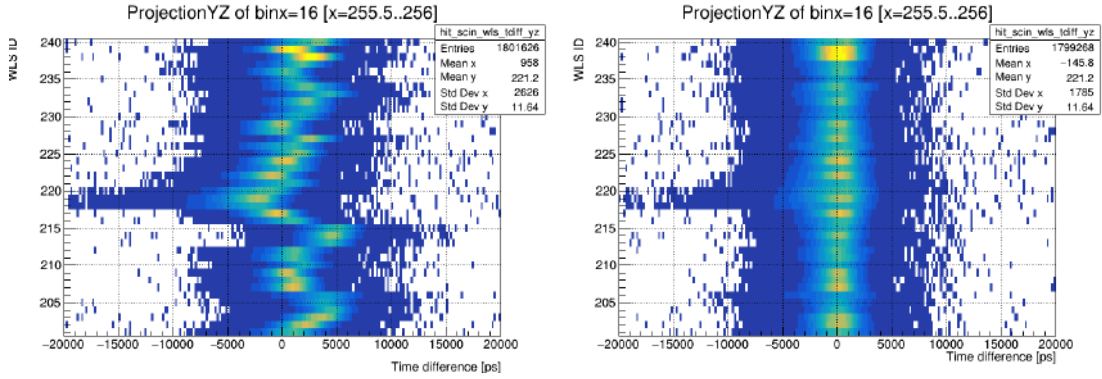
Figure 6.11: The example of time differences of scintillator hits and WLS signals in case of strip ID 255 and all the WLS. Time Difference (Left) - before the calibration, right - with applying the offsets obtained in calibration.

open source. All the results are put into the same file, which is later used during the reconstruction of other data or with the same measurement to check the correctness of the synchronization procedures.

6.4   Results

We selected data from nine different collimated positions (-22 cm, -16 cm, -10 cm, -4 cm, 0 cm, 4 cm, 10 cm, 16 cm, 22 cm) of the source to examine their influence on estimating the spatial resolution along the length of the scintillator. For each data-set, we performed the following optimization.

- DAQ time slot: 50 μs

- SiPM signal building: leading edge coincidence: 10 ns, lead-trail: 200 ns.

- SiPM Matrix signal coincidence: 10 ns

75

- Time window for the signals from both sides of the scintillator (A-B signals) is: 5 ns

- Scintillator hit-WLS signal coincidence: 4 ns

- Bin width used is 0.5 cm

- TOT cut being used only to select the annihilation: 6-7 ns

6.4.1 Z estimation

Three different methods were used to estimate the z resolution.

- Method 1: Axial position is calculated as the weighted sum position of the SiPM divided by the sum of all weights and weights calculated as TOT for a given SiPM divided by the sum of all SiPM who has a signal.

  $w_i = \frac{\text{TOT}_{\text{SiPM}_i}}{\sum_i \text{TOT}_{\text{SiPM}_i}}, \; z = \frac{\sum_i (w_i \cdot z_{\text{SiPM}_i})}{\sum_i w_i}$

  The results presented in Figure 6.12 display the distribution of reconstructed Z position obtained from all irradiated positions indicated in the legend with a bin width of 0.5 cm. The plots reveal certain empty bins, such as in the case of position -10 cm. This occurrence can be attributed to the gaps between the SiPMs that are connected to the WLS (Wavelength Shifter), as shown in Figure 6.7.

- Method 2: TOT weights squared, shown in Figure 6.13:

  $w_i = \frac{\text{TOT}_{\text{SiPM}_i}}{\sum_i \text{TOT}_{\text{SiPM}_i}}, \; z = \frac{\sum_i (w_i^2 \cdot z_{\text{SiPM}_i})}{\sum_i w_i^2}$

- Method 3: TOT and coverage weights, which means including the surface percentages and the coverage of the SiPM, shown in Figure 6.14.

  $w_i = c_{\text{SiPM}_i}^{\text{WLS}} \cdot \frac{\text{TOT}_{\text{SiPM}_i}}{\sum_i \text{TOT}_{\text{SiPM}_i}}, \; z = \frac{\sum_i (w_i \cdot z_{\text{SiPM}_i})}{\sum_i w_i}$

The results depicted in Figure 6.15 indicates that there is no statistically significant difference observed among the tested methods. Additionally, the Full Width at Half Maximum (FWHM) values were calculated for each position and compared for all methods, as shown in Table 6.1. Results for the positions -22 cm and 22 cm are omitted as WLS doesn't cover the whole length of the plastic scintillator. For a -4 cm position, the resolution is better than for 4 cm, and the same goes for positions -10 cm and 10 cm. However, for the -16 cm position, where a double peak structure is observed, the resolution is worse than 16 cm. This study concludes that the resolution on the optically covered WLS side is worse than the non-optically covered one.

Comparison between the resolution of estimation of hit position based on the three methods, which incorporate the information from WLS signals as explained above, and the estimating Z position based on the hit in the scintillator that was calculated based on the A-B time difference of signal from scintillator and velocity (equ 6.4), is shown in Figure 6.16, Figure 6.17 and Figure 6.18. Notably, the utilization of WLS signals leads to a noticeable improvement in resolution.
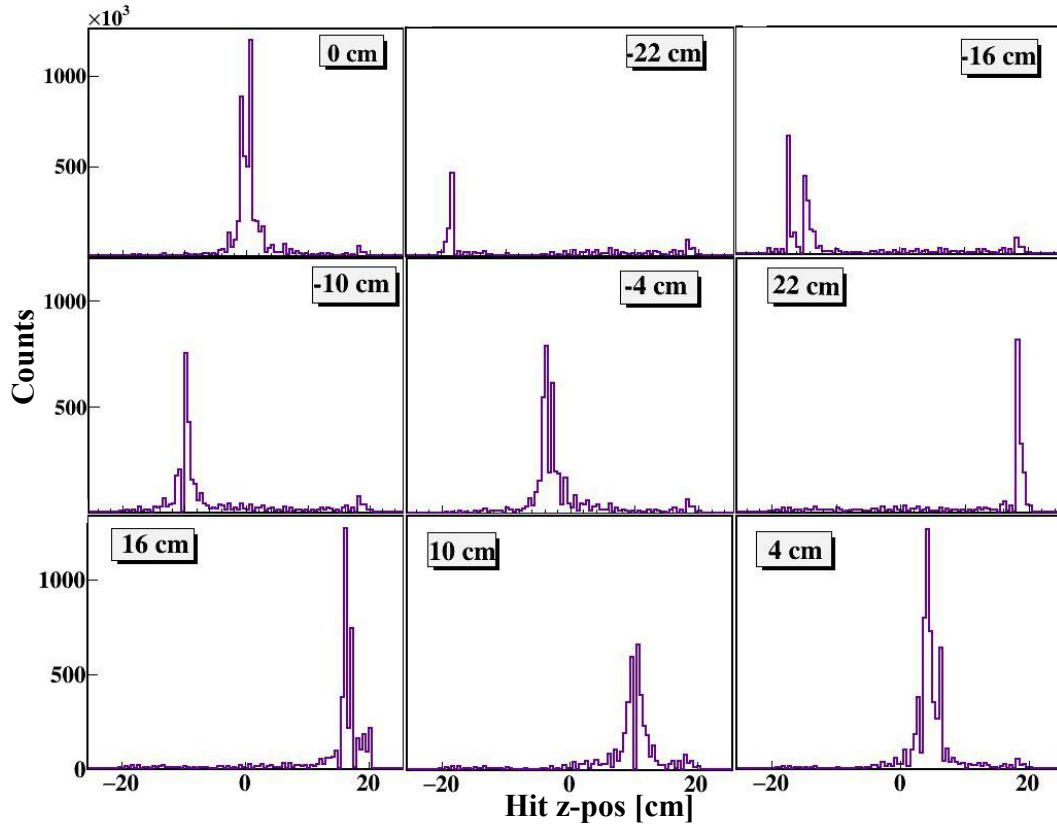
Figure 6.12: The distribution of the reconstructed Z position, derived using Method 1, for all specified irradiated positions mentioned in the legend. The bin width chosen for this representation is 0.5 cm.

Table 6.1: The Full Width at Half Maximum values were compared among the different methods. Results are presented here for all positions, and it's important to mention that for positions -16 cm, -10 cm and -4 cm, WLS were without any side reflective foils .

Position (cm)	Method 1 (cm)	Method 2 (cm)	Method 3 (cm)
-16	**2.5**	**2.5**	**2.5**
-10	**0.5**	**0.5**	**0.5**
-4	**1.5**	**1.5**	**1.0**
0	1.5	1.5	1.5
4	2.5	2.5	2.5
10	2.0	2.0	2.0
16	1.0	1.0	1.0

Comparison between the full-width half maximum between the methods estimating the z position along the J-PEM is shown in Table 6.2. The results clearly show that estimating the z position with WLS improves the resolution in compari-
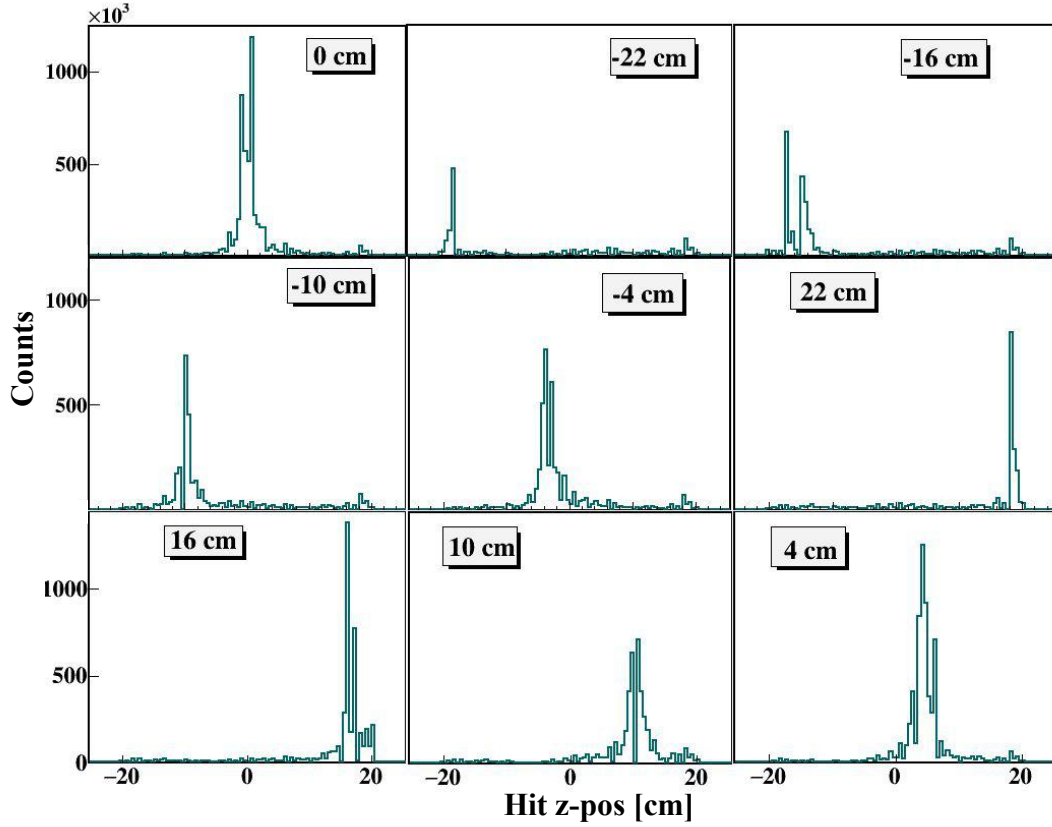
Figure 6.13: The distribution of the reconstructed Z position, derived using Method 2, for all specified irradiated positions mentioned in the legend. The bin width chosen for this representation is 0.5 cm.

son to estimating it by using the time difference information from both the end of the scintillator times the effective velocity.

Table 6.2 presents a comparison of the full-width half maximum (FWHM) between different methods for estimating the z position along the J-PEM. The results indicate that using the WLS signals for estimating the z position leads to improved resolution compared to estimating it solely based on the time difference information from both ends of the scintillator and the effective velocity.

Table 6.2: The Full Width at Half Maximum values were compared among the different methods, and the results are presented in the table.

Position (cm)	Method 1 (cm)	Method 2 (cm)	Method 3 (cm)	Plastic scintillator (cm)
-16	2.5	2.5	2.5	7.6
-10	0.5	0.5	0.5	7.6
-4	1.5	1.5	1	7.6
0	1.5	1.5	1.5	7.5
4	1.0	1.0	1.0	7.1
10	2.0	2.0	2.0	7.1
16	2.5	2.5	2.5	7.1
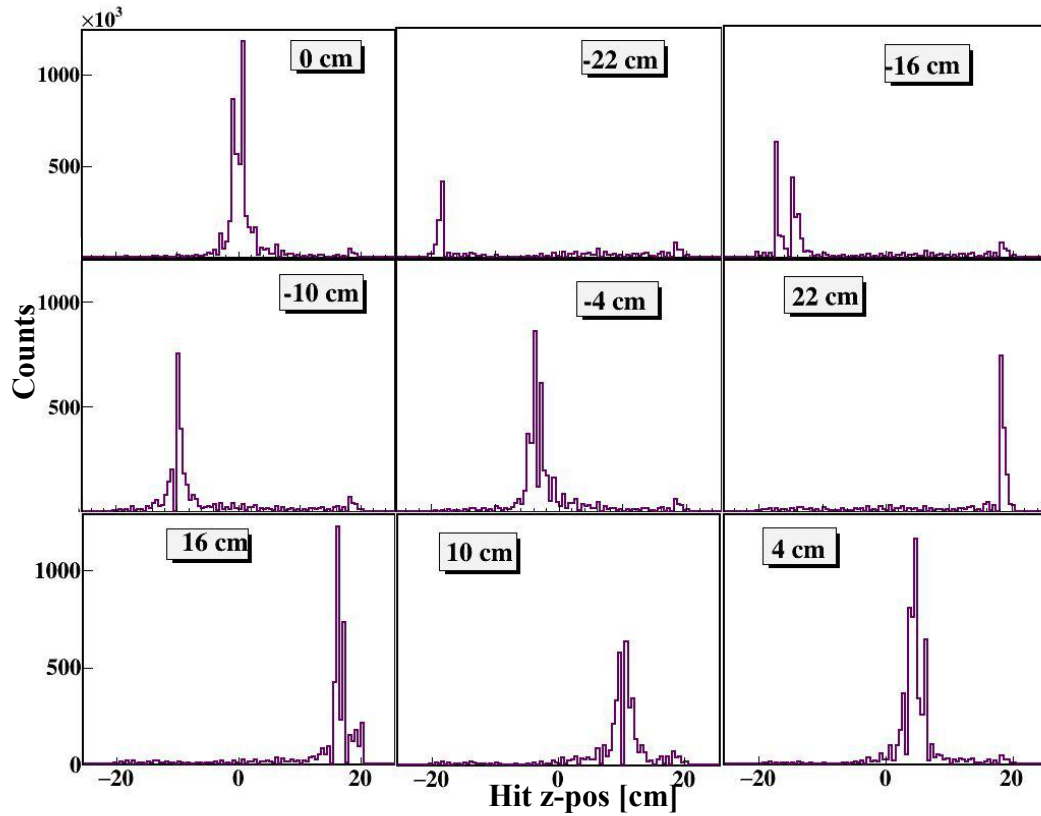
Figure 6.14: The distribution of the reconstructed Z position, derived using Method 3, for all specified irradiated positions mentioned in the legend. The bin width chosen for this representation is 0.5 cm..
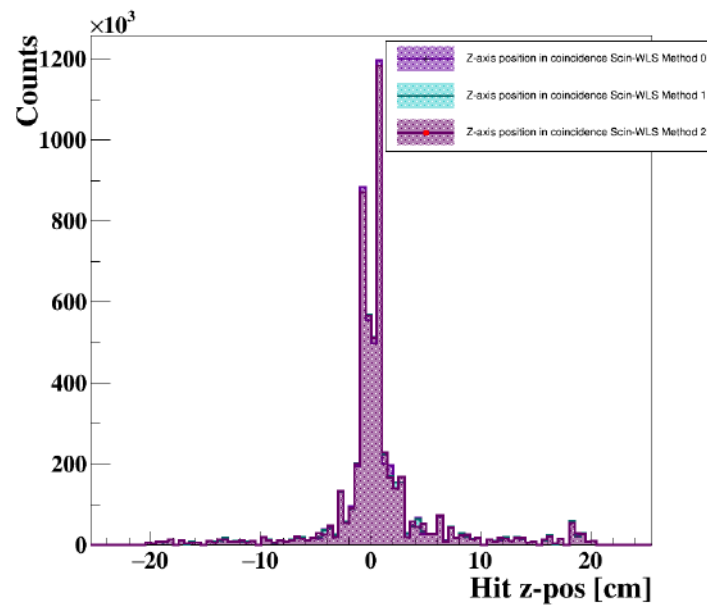
Figure 6.15: Depicted figure illustrates the comparison between all three methods when the source was placed at the centre.
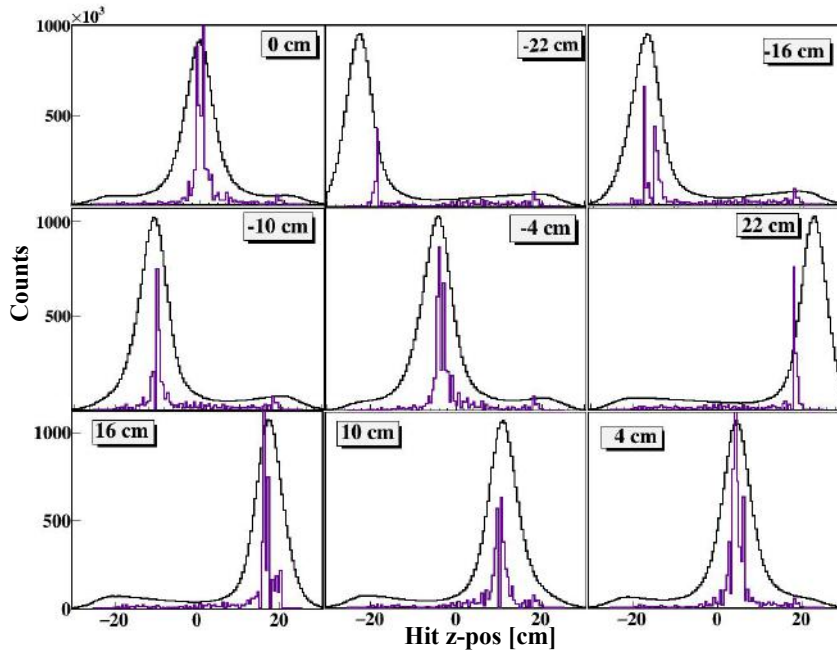
Figure 6.16: The presented figure provides a visual comparison between the distribution of the reconstructed Z position, obtained using Method 1 (represented by the purple histogram) and the distribution obtained using the time difference at scintillator strips (depicted by the black line) for all specified irradiated positions. It illustrates the contrast between the two methods in terms of their accuracy in estimating the z position.
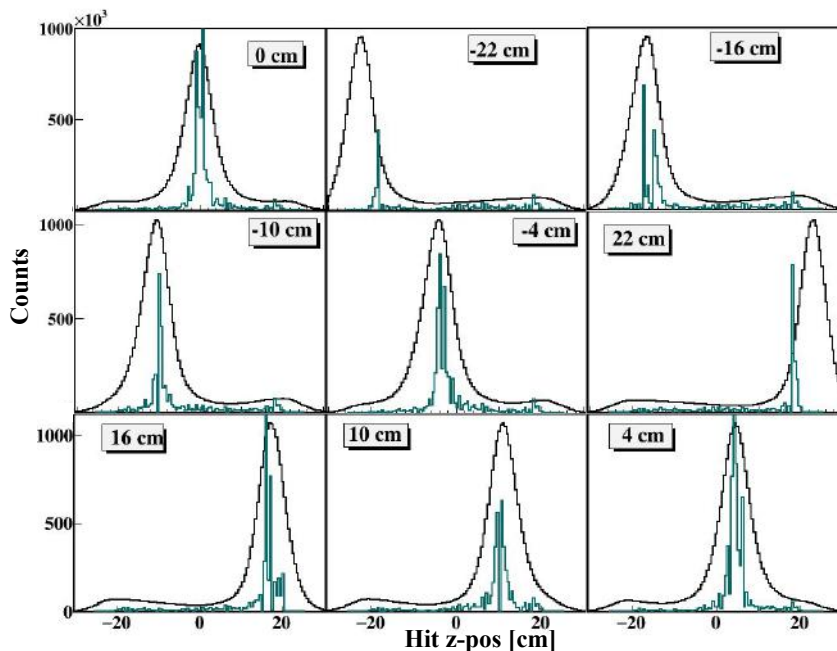
Figure 6.17: The presented figure provides a visual comparison between the distribution of the reconstructed Z position, obtained using Method 2 (represented by the cyan histogram) and the distribution obtained using the time difference at scintillator strips (depicted by the black line), for all specified irradiated positions. It illustrates the contrast between the two methods in terms of their accuracy in estimating the z position.
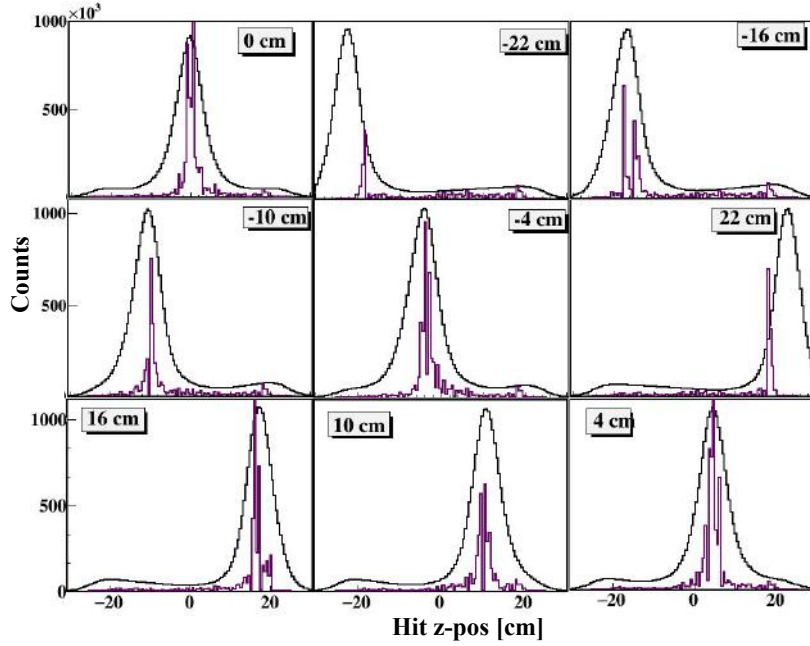
Figure 6.18: The presented figure provides a visual comparison between the distribution of the reconstructed Z position, obtained using Method 3 (represented by the magenta histogram) and the distribution obtained using the time difference at scintillator strips (depicted by the black line), for all specified irradiated positions. It illustrates the contrast between the two methods in terms of their accuracy in estimating the z position.

6.4.2 Depth of interaction (DOI)

DOI measurements were also performed to check the ability of a detector to determine the depth or location of interaction within the J-PEM detector volume of the annihilated gamma. The measurements are performed at three different positions, specifically 6 mm, 12 mm, and 18 mm from the bottom of the strip. In Figure 6.19, it is evident that the scintillator with ID 266 exhibits the highest number of entries, indicating the position of the irradiated source.

The analysis of the data reveals interesting trends. At the 6 mm position, the highest coincidence is observed with a multiplicity of 2, indicating that signals in two WLS are detected. However, when considering coincidences with a multiplicity of 4, the observed multiplicity is 35% lower compared to the highest coincidence with a multiplicity of 2. Similarly, at a position of 12 mm, the highest coincidence is observed with a multiplicity of 2, and it reduces to 40% in the case of multiplicity 4. And in the case of 18 mm, there is a 60% drop for multiplicity 4 compared to 2 multiplicity, as shown in Figure 6.20.

Table 6.3: The table presents a comparison of the mean values for all three positions.

Position	Mean	Standard deviation
6 mm	2.8	1.3
12 mm	2.7	1.2
18 mm	2.5	1.1
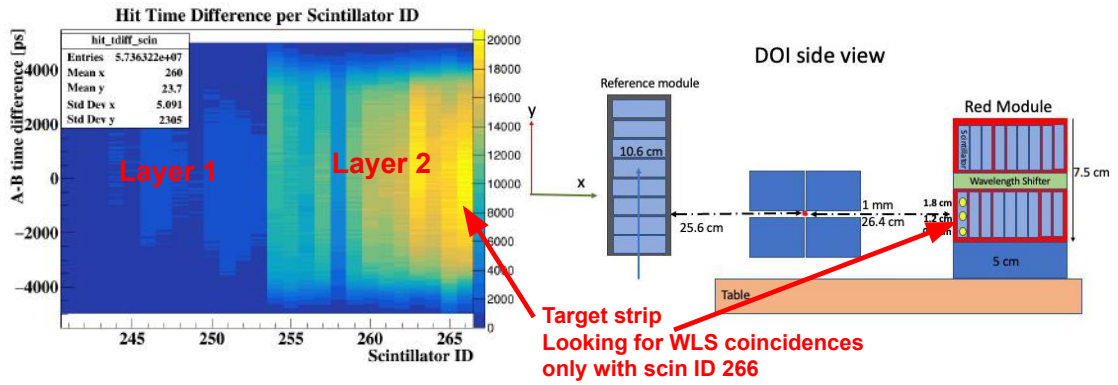
Figure 6.19: (Left) The figure shows the time difference between two layers of plastic scintillator when the source was positioned at 18 mm. (Right) Detection setup used for the studies of J-PEM abilities to determine the DOI.
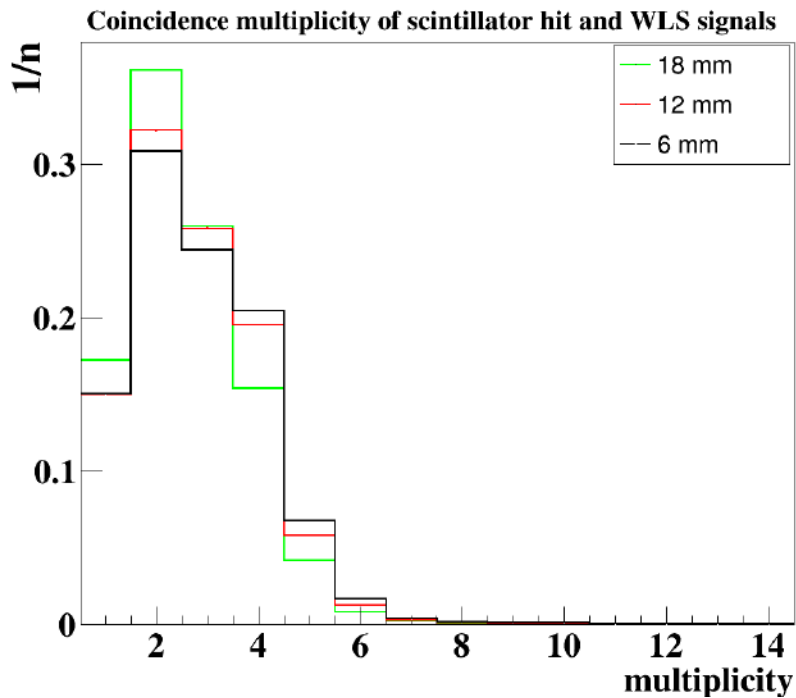
Figure 6.20: The distribution presented in the figure illustrates the DOI multiplicity of wavelength shifting (WLS) with scintillator ID 266 in coincidence. The multiplicity values are normalized to the number of entries, allowing for a relative comparison of the occurrence of different multiplicity levels.

The mean calculation for the multiplicity distribution at all three positions was done, as the differences in mean multiplicity across positions can provide information about the detector's ability to accurately determine the depth of interaction, highlighting variations in its DOI sensitivity at different locations within the detector, as shown in Table 6.3.

The observed differences in the mean multiplicity suggest a variation in the sensitivity of the detector for depth of interaction (DOI) measurements across different positions. While the sensitivity for DOI may not be particularly strong based on these variations, there is potential for improvement. One possible approach to enhance the DOI sensitivity is by constructing a detector with narrower WLS matched with the size of SiPM.

By considering these findings, it is evident that further development and optimization of the detector, specifically focusing on the dimension of WLS layers, hold promise for improving the DOI sensitivity and enhancing the overall performance of the detector in depth-of-interaction measurements.

Chapter 7

Conclusion and future perspective

The main objective of this thesis was to validate the hypothesis that plastic scintillators can be effectively utilized in positron emission mammography (PEM) to detect breast cancer. The ultimate goal was to develop a system that combines cost-effectiveness with high specificity in breast cancer detection. To achieve this aim, a prototype named J-PEM was developed, incorporating plastic scintillators and wavelength-shifting (WLS) technology. By leveraging the unique properties of plastic scintillators and WLS technology, the J-PEM system aimed to provide accurate and reliable detection capabilities while maintaining cost-effectiveness.

To achieve the stated objective, the following steps were undertaken in this study:

- First step was to investigate the currently employed methods and analyse the hospital data to compare the sensitivity, specificity, and AUC values for mammography, ultrasound, and MRI. The purpose was to evaluate the performance of each imaging modality in detecting breast cancer.

- Following a comprehensive understanding of the advantages and limitations of existing imaging modalities, a novel and innovative Positron Emission Mammography (PEM) detector, namely J-PEM, was designed. The design process incorporated insights obtained from an extensive review of the relevant literature. Various factors, including the selection of detector materials, configuration, photon detection techniques, and signal readout methods, were carefully considered while developing this new PEM detector.

- Prior to the physical construction of the J-PEM detector, simulations were conducted to optimize the detector's geometry and generate reconstructed images for the double-head J-PEM module. The purpose of these simulations was to fine-tune the configuration of the detector, enhancing its performance and attaining the highest possible image quality.

- After the completion of the design and simulation phase, the construction process commenced. This involved procuring the required materials, components, and equipment to assemble the detector. Special attention was given to incorporating plastic scintillators and wavelength-shifting (WLS) technology within the detector design. These elements aimed to improve spatial resolution, efficiency, and cost-effectiveness in breast cancer detection. Additionally, Silicon Photo-multipliers (SiPMs) were utilized for the readout of the signals generated by the detector. To ensure the reliability and performance of each

component used to construct the J-PEM detector, testing and validation were conducted for each of them individually.

- Data collection was conducted to assess the characteristic performance of the developed J-PEM detector. This involved performing measurements by irradiating the detector with ^{22}Na to evaluate its capabilities and effectiveness in detecting and diagnosing breast cancer. To ensure accurate and reliable measurements, calibration methods were developed for the J-PEM detector. During data collection, various aspects of the detector's performance were assessed. This included establishing the methods for estimating the spatial resolutions and overall performance in detecting and diagnosing breast cancer. And also, separate sets of measurements were performed to determine the depth of interaction sensitivity.

Results were presented from three different perspectives:

- Results from the medical study: This study aimed to provide insights and comparisons among various imaging modalities, including ultrasound (USG), mammography, and MRI, for breast cancer detection. In terms of diagnostic performance, magnetic resonance imaging (MRI) demonstrated the highest area under the curve (AUC), indicating its effectiveness as a diagnostic tool for breast cancer. Both MRI and mammography (SM) showed a sensitivity of 100%, meaning they correctly identified all positive cases. However, contrast-enhanced mammography (CM) and ultrasound (US) had lower sensitivity rates, indicating a higher likelihood of false negatives. When considering overall accuracy, SM exhibited the highest value among CM, US, and MRI, although the difference was not statistically significant. Both SM and MRI had a negative predictive value (NPV) of 100%, indicating their ability to accurately identify individuals without breast cancer. On the other hand, CM and US had lower NPV values, suggesting a higher chance of false positives. SM emerged as the most commonly utilized method in breast cancer diagnostics due to its high sensitivity, accuracy, positive predictive value (PPV), and negative predictive value (NPV). It effectively detected breast cancer cases and provided reliable results. However, it's worth noting that PET/CT has been reported to detect a higher number of breast lesions compared to other modalities, with sensitivity and specificity rates of 96% and 91%, respectively. PET/CT allows for simultaneous evaluation of both local and general stages of breast cancer. Nonetheless, its limited availability and high cost currently restrict its widespread application in primary breast cancer diagnostics.

- Results from simulations: The results highlight the benefits of increasing the number of iterations during the reconstruction process, improving image quality and spatial resolution. The simulation was able to reconstruct the point sources using the J-PEM setup successfully. This indicates that the J-PEM configuration and algorithm employed in the simulation are effective in accurately reconstructing the positions of the point sources. The successful reconstruction further demonstrates the potential and efficacy of the J-PEM setup for imaging and localization tasks. The calculated point spread function (PSF) indicated a spatial resolution of approximately 4 mm in the sagittal (along z) and coronal directions, while it was 10 mm along the tangential direction

(along y) achievable. These findings demonstrate the J-PEM setup's capability to accurately reconstruct and resolve point sources with a satisfactory level of spatial resolution.

- Results from the experiment: The presented results showcase a comparison between various methods for estimating the z position along the scintillator, utilizing wavelength-shifting (WLS) technology. The findings indicate that by incorporating WLS, it is possible to enhance the spatial resolution to approximately 5mm. This improvement in resolution signifies the potential of WLS-based techniques for accurately determining the z position within the scintillator. The investigation comparing WLS utilization with and without optical separation indicates that employing WLS without optical separation offers enhanced resolution compared to the alternative approach. Furthermore, the evaluation of DOI sensitivity has indicated that while its sensitivity may not be particularly strong, the potential for improvement lies in the introduction of narrower WLS during future advancements, which holds the promise of enhancing its overall performance. Table 7.1 compares the resolution between several commercially available breast imaging devices and J-PEM.

Table 7.1: Comparison of characteristics of some commercially available dedicated breast imaging devices with J-PEM [119, 120, 121, 122]

Device	Design	Detector type	FOV (cm)	Patient positioning	Breast compression	Resolution (FWHM) [mm]
Discovery NM750b (GE Healthcare)	Dual flat panel	CZT	24×16	Seated	Yes	4.8 to 5.6
LumaGEM 3200s (Gamma Medica)	Dual flat panel	CZT	20×16	Seated	Yes	1.6
PEM Flex Solo II (CMR Naviscan Corporation)	Dual flat panel	LYSO	24×16.4	Seated	Yes	1.5 to 2.0
Clear-PEM (Crystal clear collaboration)	Dual flat panel rotating	LYSO	16.2×14.1	Prone	Yes	1.2
MAMMI-PET (Oncovision)	Full ring	LYSO	17 diameter 4 axial length	Prone	No	1.9 to 2.6
J-PEM (Jagiellonian)	Dual flat panel	Plastic scintillator	12×50	Seated	No	∼5

This thesis opens up new perspectives for:

1. Improved breast cancer detection: The development of a novel J-PEM system utilizing plastic scintillators and wavelength-shifting technology offers the potential for enhanced breast cancer detection capabilities. By optimizing the detector design and leveraging these innovative techniques, the system may provide improved sensitivity and specificity in detecting breast cancer lesions.

2. Cost-effective diagnostic solutions: Incorporating plastic scintillators in the J-PEM system aims to provide a cost-effective alternative for breast cancer diagnostics. By utilizing readily available and cost-efficient materials, the J-PEM system may help reduce the economic burden associated with breast cancer detection and diagnosis.

3. Advancements in imaging technology: The research conducted in this thesis contributes to the advancement of imaging technology specifically tailored for

breast cancer detection. By exploring the use of plastic scintillators and innovative detector designs, the thesis lays the foundation for future developments and improvements in imaging techniques for breast cancer diagnosis.

4. Potential clinical applications: The successful implementation of the J-PEM system has the potential to find practical applications in clinical settings. The improved spatial resolution and accuracy offered by the system may aid in the early detection, precise localization, and characterization of breast cancer lesions, thereby facilitating more effective treatment planning and patient management.

5. Future research directions: The findings and insights obtained from this thesis can inspire further research in the field of breast cancer detection. Researchers can build upon the developed J-PEM system, refining its design, optimizing its performance, and exploring additional applications and potential advancements in breast cancer imaging technology. Furthermore, the J-PEM system's portability and non-invasiveness make it suitable in various clinical settings, including primary care centres, specialized breast clinics, and remote areas. It has the potential to offer real-time imaging and immediate results can help expedite the diagnostic process and improve patient management.

Appendix A

Silicon Photo-multipliers

A.1 Single-photon avalanche photodiode (SPAD)

When a photodiode absorbs light or photons, if the photon has enough energy, it strikes an atom within the device and releases an electron. This creates electron and hole pairs, where a hole is merely a "void" for an electron, as shown in Figure A.1. The reverse bias applied to the photodiode sets up the electric field that causes these charged particles to accelerate toward the terminal. Electrons will flow toward the positive potential on the Cathode, whereas holes will go toward the negative potential on the Anode. These moving charge carriers generate the current (photocurrent) in the photodiode [123, 124].
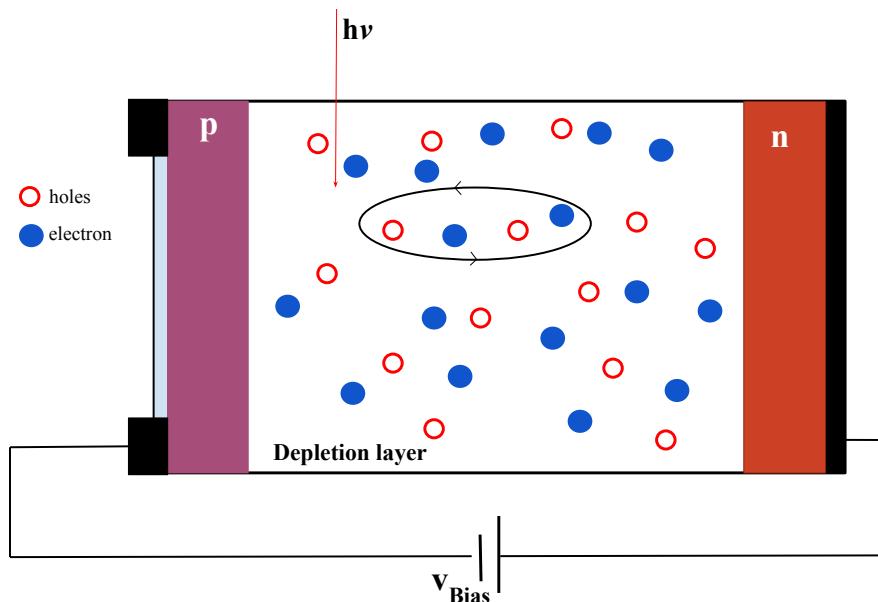
Figure A.1: Repersentaion of the p-n junction. Here is the case when the bias voltage is applied above the breakdown voltage, which initiates the self sustain avalanche, creating the electron (blue) and hole (red).

In the case of a single photon avalanche photodiode, If the applied reverse bias is beyond the breakdown voltage of the diode, the diode is said to be operating in Gieger mode. When a bias, excessive breakdown voltage is applied to the diode, an

avalanche region is created at the p-n junction. Any charge carriers in this region are then accelerated to such an extent that they generate secondary charge pairs through the impact of ionization. Each of these new charge carriers also causes further ionization creating a self-perpetuity avalanche that spreads throughout the silicon volume, subject to an electric field. The silicon breaks down and becomes conductive, amplifying the original electron-hole pairs to microscopic current [125]. The avalanche current rise so fast it's almost instantaneous, and the current is also so large that it can be detected in the range of milliamps. When the photon is detected, the photon's arrival time is indicated by the leading edge of the avalanche pulse current signal. This current continues to flow until the avalanche is quenched by an external circuit that reduces the bias voltage to or below the breakdown voltage (as a lower electric field cannot accelerate the carriers to impact the ionization with the lattice of an atom).

There are mainly two methods to quench an avalanche, either actively or passively. The simplest one is the passive quenching mechanism consists of placing a resistance R_Q in series with the p-n junction, Figure A.2. The quenching mechanism is all about the redistribution of voltages When the SPAD is metastable, switch S is open; however, when a photon strikes the SPAD or there is a thermally generated charge, the switch closes, and this is when the avalanche in the diode starts. In Figure A.2, the detailed circuit of SPAD with passive quenching is explained. In this circuit, two loops, coloured magenta and orange, are used to determine the current across the circuit, as shown in Figure A.2. Where the magenta loop represents the current that one can see (current pulse), and the orange loop represents the internal current to SPAD in this model At the start of an avalanche, the current is zero, but once the avalanche starts, the magenta current rapidly rises, which means the voltage at R_Q increases, whereas the voltage at SPAD decreases because one has to satisfy Kirchhoff's voltage rule. So as the current increases, at some point, the voltage at the SPAD starts to lower to a value around V_{BD}, and due to statistical fluctuation avalanche is going to stop because there is not enough overvoltage (The difference between the biasing voltage and the breakdown voltage) to maintain the avalanche, as shown in the bottom right of Figure A.2. At this point, quenching occurs, the switch effectively opens, and junction capacitance recharges. i.e. the voltage on each SPAD is now increased, but the current in the circuit decreases. The load resistor in the circuit is to convert the current into voltage. So the voltage waveform in the bottom left of Figure A.2 is typically observed on the load resistor. The total time required for quenching and recharge is called dead time, and this time interval typically lasts for at least 10 to 100 nanoseconds. Dead time varies depending on whether the diode is being quenched actively or passively, and during this time, the detector is inactive.

The drop in the voltage across the SPAD is usually converted to a digital pulse using a comparator, and as a result, SPADs can detect single photons. However, whilst the APD output voltage is below the comparator threshold, the comparator output voltage will not change if a second avalanche event occurs. This period is therefore referred to as the dead time of the SPAD. However, they can also be used to obtain the time of arrival of the incident photon due to the high speed that the avalanche builds up and the device's low timing jitter. The voltage output is directly linked to the number of photons the pixels absorb.
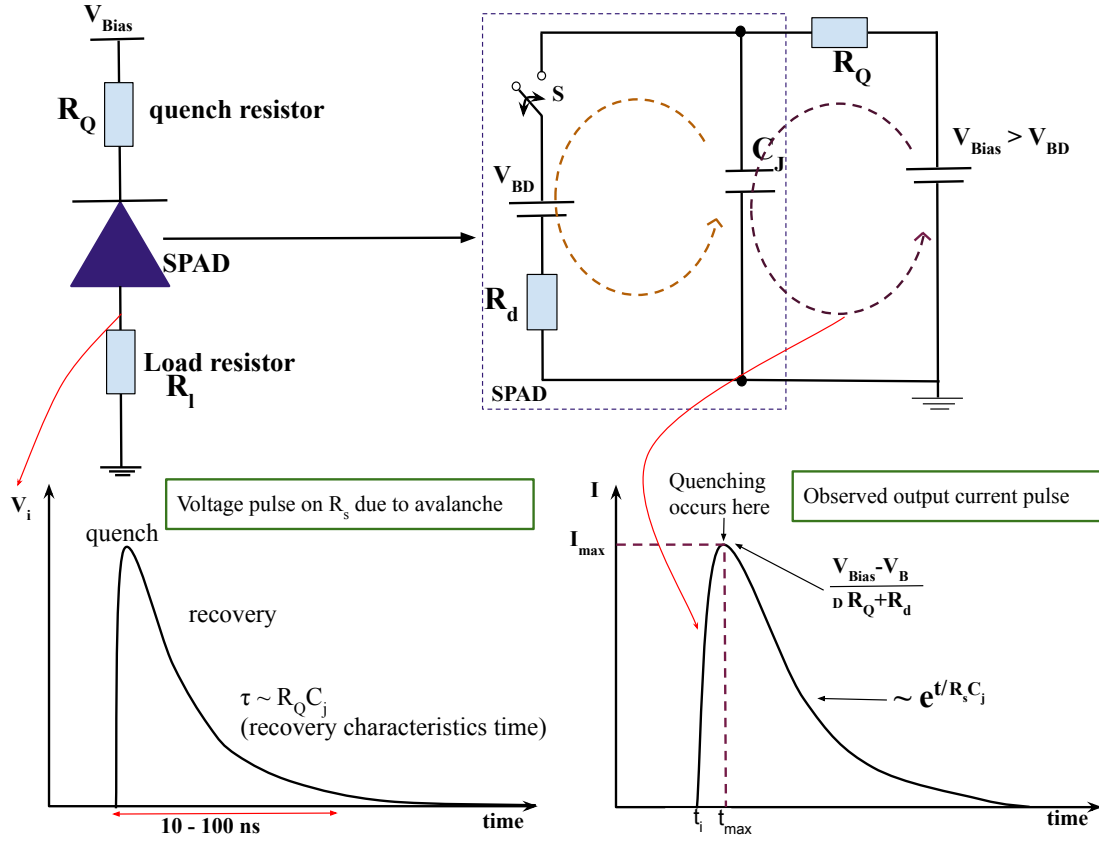
Figure A.2: The simplified electrical equivalent circuit of a microcell that is externally biased with VBIAS is shown in the top left figure. The microcell is in Geiger mode when there are no light or dark counts: the switch S is open, the voltage across the junction capacitance C_J is VBIAS, and no current flows via the quenching resistor R_Q or the series resistance Rd. When a charge carrier causes an avalanche, switch S closes, and C_J begins to discharge via R_d (shown in the image with the orange swirl), generating a voltage drop on R_Q and, as a result, a current through the SiPM terminals. In the bottom right figure, the current pulse begins at t_i and rapidly increases until it reaches the maximum value i_max at t_max, which is on the order of ~ 1 ns. At t_max, the voltage on the APD decreases to around V_BD, which is insufficient to maintain the avalanche. At this point, quenching occurs. The junction capacitance C_J begins recharging, causing the voltage across R_Q to be decreasing and, thus, the current through the terminals of the SiPM to also decrease exponentially with the characteristic time $\tau = R_Q \times C_J$. For typical values of R_Q and C_J, $\tau \approx 10$ ns. Image used courtesy of Hamamatsu.

A.1.1 Silicon photomultipliers

Silicon photomultipliers (SiPM) are solid-state single-photon-sensitive devices based on a single-photon avalanche diode (SPAD) constructed on a common silicon substrate, as shown in Figure A.3. SiPM consists of an array, also known as microcells or pixels, of SPAD connected in series to a quenching resistor, and a large number of these pixels are connected in parallel to form a SiPM structure, so therefore as two prongs, an anode, and a cathode [126, 127].
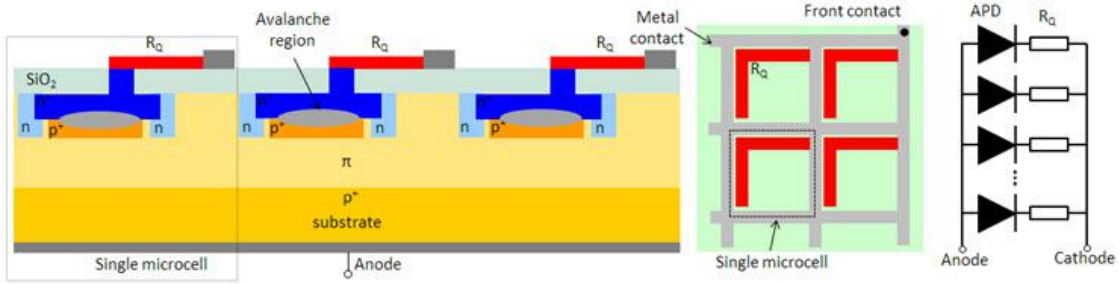
Figure A.3: This figure depicts a vertical cross-section of the single microcell. On the surface, we have a quenching resistor, R_Q, which is connected through silicon oxide through an insulator layer to the P-N structure below, which is the structure of the avalanche photodiode. The structure depicted here is n on p structure, which means n-type semiconductor silicon on a p-type substrate. It does not correspond to the actual structure of the Hamamatsu product. In a SiPM, each pixel or microcell comprises a series of avalanche photodiodes (APD) and a quenching resistor (RQ) [128]. A SiPM has two prongs, an anode and a cathode because all of the microcells are linked in parallel. The three panels in the picture above display an equivalent electrical circuit, a cross-section of three microcells in a potential architecture, and the device's top perspective (the side facing impinging light).

Each pixel in SiPM outputs a pulse at the same amplitude when struck by the photon, which is then converted into voltage pulses on a load resistor (explained in the previous section), as shown in Figure A.4 [129]. The resultant output is the chronological superimposition of the pulse, which means that if two microcells had struck at the same moment, the resultant pulse would have twice the amplitude.

In the case of SiPM, we have a pulse with a fast component due to the parasitic capacitance on the quench resistor. One may or may not see it depending on the bandwidth of the detection system. and the recovery time is about five time RC time constant where r is quenched resistor a C is junction capacitance.

- **Gain** A SiPM's gain is the amount of charge generated for each detected photon and is affected by overvoltage and microcell size, as shown in Figure A.5. Gain can be calculated from the overvoltage, microcell capacitance and electron charge [130].

$$Gain = \frac{Capacitance \times overvoltage}{electron_charge}$$

- **Photon detection efficiency (PDE)**
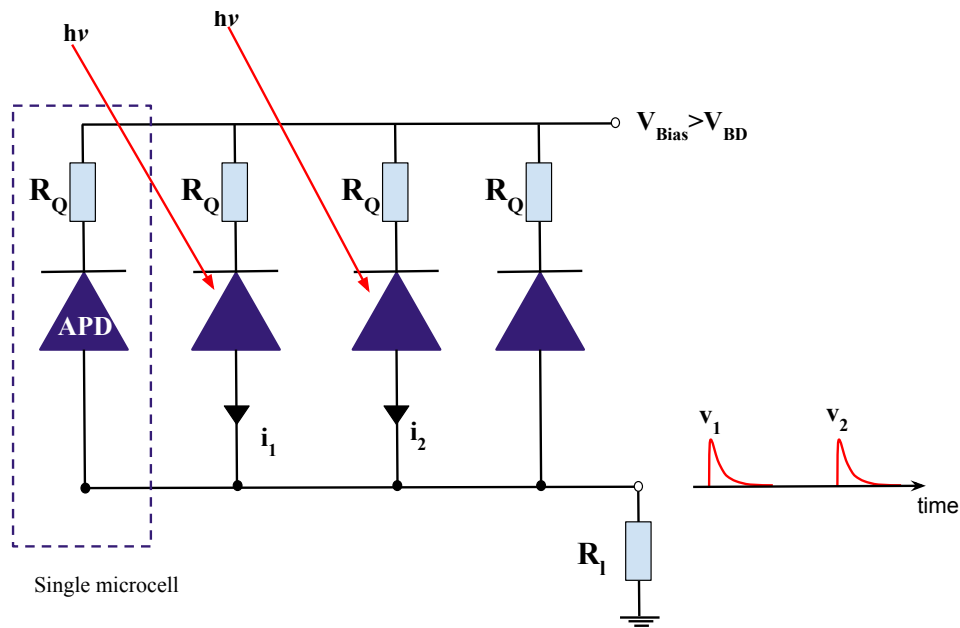
Figure A.4: Image used courtesy of Hamamatsu
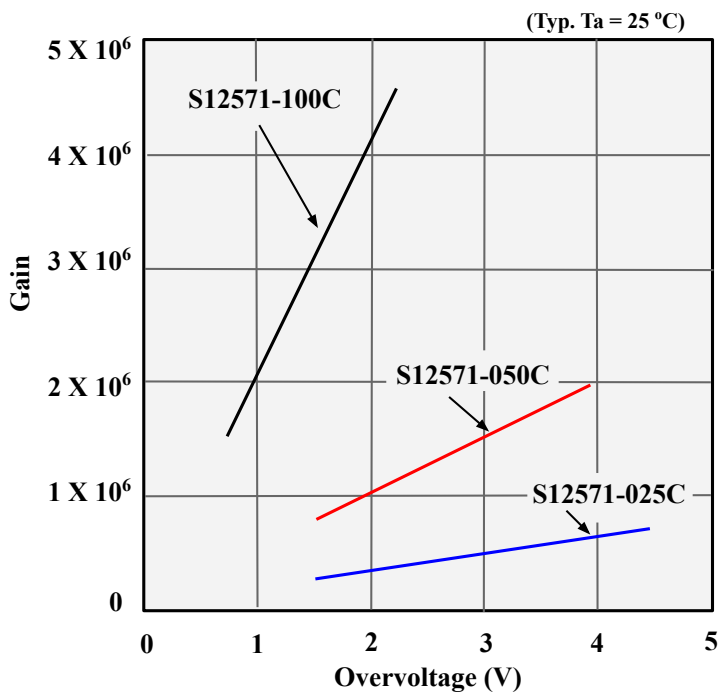
Figure A.5: The linear relationship between the gain and overvoltage for three SiPMs manufactured by Hamamatsu: S12571-100C, S12571-050C, and S12571-025C.In the linear relationship between the gain and overvoltage shown by Figure for three SiPMs, note that for a given ΔV, the gain increases with the size of a microcell and, thus, with CJ.

The photon detection efficiency (PDE), which measures how well a SiPM can sense photons, is one of the most crucial characteristics of SiPMs. It indicates the likelihood of a photon absorbing in silicon and producing an electron-hole pair (accounting for the loss of electrons or holes by recombination or capture at defects). The PDE is calculated as the product of quantum efficiency, fill factor and avalanche probability, as given in the equation below [127, 131].

$$PDE = QE \times CE$$

QE = silicon's quantum efficiency
CE = avalanche probability × fill factor
where the fill factor is the ratio of the SiPM pixel's photosensitive area to the pixel's total area.
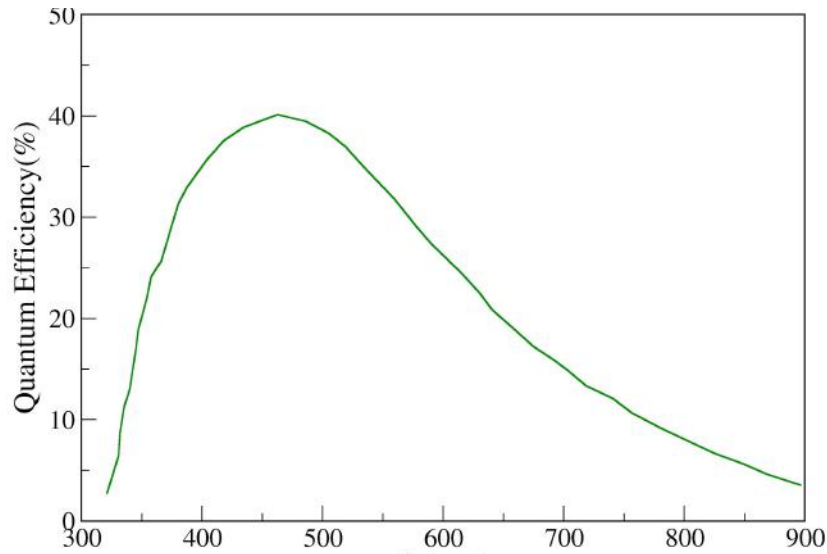
Figure A.6: This is the distribution of the quantum efficiency of SiPM used in the J-PEM detector. The PDE is generally a function of the overvoltage $V_o v$ (operational bias voltage minus the breakdown voltage) and the wavelength.

A.1.1.1 Noises in the SiPM

The primary disadvantages of SiPMs are their excessive noise, which is associated with the random SPAD multiplication process. In SiPM, there are three categories of noise, explained below:

- **Dark count**

In SiPM operation, carriers that are formed thermally (in the absence of light) can also produce pulses in addition to photon-generated carriers; these pulses are called dark pulses. The number of dark pulses observed is the dark count, and the number of dark pulses per second is termed the dark count rate.

The dark count rate in SiPM depends on overvoltage and temperature, as in SiPM, dark counts can originate from either band-to-band thermal excitation or band-to-band tunnelling, where the first process is very sensitive to temperature and the second one is to voltage. And the observed pulses are indistinguishable from

that resulting from the absorption of a photon and cause inaccuracy in detecting photon signal, as shown in Figure A.7. SiPM devices typically feature a limited active area to minimize the number of generations and recombinations and assure quick single-photon timing [132, 133].
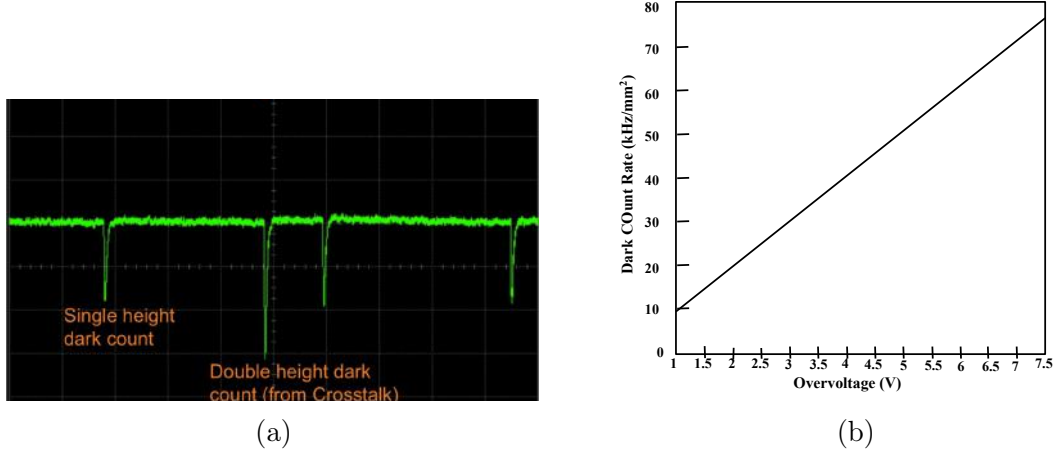
Figure A.7: (a) Showing the dark pulses from the oscilloscope. The centre dark count pulse in the figure has a pulse height double that of the other single photon dark counts, implying that it is caused by crosstalk. The dark count rate changes with the ambient temperature because dark pulses are created by carriers that are thermally generated. (b) Dark Count Rate vs Overvoltage for a 3 mm, 35-micrometre SiPM Microcell.

- **Cross talk :**

The so-called cross-talk is an additional noise source in SiPMs that is nonexistent in PMTs. When light penetrates a single SiPM pixel, there are instances when a pulse of 2 p.e or higher is observed, as shown in Figure A.8. This is because primary photons can trigger the secondary photons generated in the avalanche multiplication process of the SiPM pixel, and those photons are detected by other pixels. This phenomenon is called optical crosstalk. In essence, it is the output of the other pixels co-occurring with light detection [132, 134].

There are typically three types of cross-talk; Direct cross-talk: When secondary photons traverse directly to neighbouring cells after being triggered by primary photons. Delayed cross-talk: This is also caused by secondary avalanche photons, which are absorbed in the undepleted region of a neighbouring SPAD. This results in photon-generated minority carriers, which can reach the multiplication region of the SPAD by diffusion and trigger additional avalanches after some delay. The external cross-talk: It's the reflection of the secondary photons in the protective glass or epoxy window on top of the SiPM or in the coupled (glued) scintillator. The eradication of optical cross-talk in SiPMs is crucial to achieving the best timing and energy resolution. A high cross-talk probability can severely limit the highest bias voltage at which the SiPM is operational and, therefore, limits the SiPM gain, photon detection efficiency, and single-photon time resolution.

- **After pulsing**
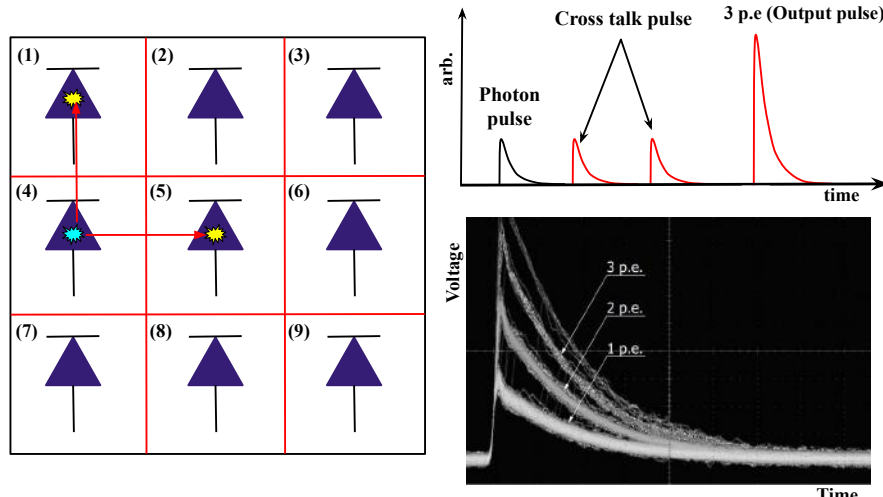
Figure A.8: Primary discharge (blue colour) can trigger the secondary discharge (yellow colour) in the neighbouring macrocell. Each pixel or microcell has its circuit and quenching resistor. For example, there is primary discharge in microcell 4; this discharge produces photons with enough energy to excite SPAD in the neighbouring sites. In these cases, it produces secondary discharge in SPAD numbers 1 and 5 (shown on the left). Since the SPADs are connected in parallel in the case of SiPM, the output signal will be the summation of all three pulses, i.e. 3 p.e waveforms coming from outputs 1, 4, and 5; this is cross-talk (shown on the top right). The bottom left is an example of crosstalk pulses (Image used courtesy of Hamamatsu).

when the carriers from the primary avalanche are trapped in impurity energy level (or lattice defects). These carriers are then released after the short delay (typically 1-10 ns) upon receiving the required energy, as shown in Figure A.9.
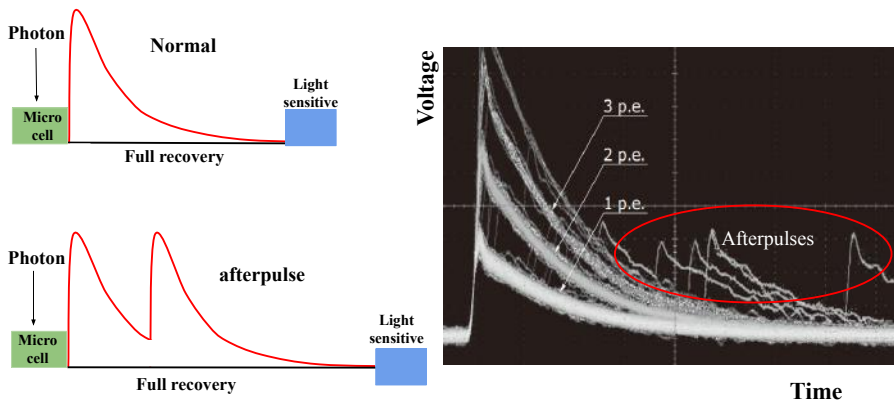
Figure A.9: Afterpulse observation example. Photon hits the microcell, in green colour, and goes into the discharge, resulting in waveform on the load resistor, and it takes some time to recover fully. In case of afterpulsing, in the recovery mode, the charge in this microcell is trapped, this charge gets released, and it can re-initiated the avalanche, so now one has a secondary avalanche, which effectively increases the time for this microcell to go back to the light-sensitive state.

After the release, these carriers trigger another avalanche process, which appears with delays along the photon-generated carriers and is observed as afterpulses. Afterpulses are produced at a time that is later than when the incident light is received [134, 135].

Appendix B

Hospital Data

A retrospective analysis was conducted on 131 patients who underwent mammography, ultrasound, spectral mammography (SM), and magnetic resonance imaging (MRI) before surgical procedures. The study received approval from the hospital's ethics committee, and all patients provided written informed consent. Pathological assessment of the breast lesions was performed through core needle biopsy or surgical excision. The medical records of the patients were reviewed to analyze key clinicopathological factors such as age, lesion site, tumor size [mm], grade, and histological type, as shown in Table B.1. Three radiologists independently reviewed all visible lesions in a blinded evaluation. Each radiologist interpreted a similar number of tests for conventional mammography (CM), spectral mammography (SM), ultrasound (US), and magnetic resonance imaging (MRI).

Table B.1: The table contains all the information required to calculate the sensitivity and specificity for a CM, SM, USG and MRI. It includes the size [mm] of the lesion, BI-RADS numbering and also the results from the histopathology (his-pat).

Patient no.	CM size [mm]	SM size [mm]	USG size [mm]	MRI size [mm]	BI-RADS CM	BI-RADS SM	BI-RADS USG	BI-RADS MRI	Hist-pat	hispat size [mm]
1	13	13	12	6	4	5	4	4	10	12
2	15	15		6	5	5	1	5	1	12
3	20	20	17	6	5	5	5	5	1+7	23
4	-	6	-	7	1	5	1	5	1+7	20
5	-	11	19	8	1	5	5	5	1+7	17
6	25	21	18	8	5	5	5	5	1	14
7	20	28	24	8	5	5	5	5	1	38
8	40	50	40	9	5	5	5	5	1	40
9	20	23	17	9	4	5	5	5	1	20
10	38	37	28	9	5	5	5	5	1	30
11	18	24	15	10	4	5	4	5	1	20
12	15	12	9	10	4	5	5	5	1	18
13	30	30	18	10	5	5	5	5	1	24
14	30	110	24	10	5	5	5	5	1	70
15	19	27	19	10	5	5	5	5	1	19
16	25	25	18	10	4	5	4	4	10	14
17	13	11	10	10	4	5	5	4	1	12
18	40	28	30	10	5	5	5	5	1	28
19	15	15	10	11	5	5	5	5	1+7	15
20	40	15	12	11	4	5	5	5	2	15

Patient no.	CM size [mm]	SM size [mm]	USG size [mm]	MRI size [mm]	BI-RADS CM	BI-RADS SM	BI-RADS USG	BI-RADS MRI	Hist-pat	hispat size [mm]
21	20	27	20	11	4	5	4	4	1	25
22	20	70	30	11	4	5	4	5	1	60
23	25	25	10	12	4	5	4	5	3	28
24	40	50	15	12	4	5	5	5	1	15
25	15	22	25	12	4	5	5	5	1+7	20
26	30	30	18	12	4	5	5	4	1	17
27	30	26	20	13	4	5	5	5	1+7	19
28	15	18	15	13	4	5	5	5	6	25
29	25	36	18	13	4	5	5	5	1	20
30	18	50	18	13	4	4	4	5	1+7	6
31	40	54	48	14	4	5	5	5	2+8	35
32	40	68	39	14	5	5	5	5	2	50
33	30	22	17	14	5	5	5	5	1	17
34	15	-	10	14	4	1	4	2	10	12
35	10	11	12	14	4	4	4	4	7	10
36	45	31	25	14	5	5	5	5	1	26
37	20	20	16	14	2	4	4	4	10	14
38	11		10	15	4	1	4	2	10	9
39	12	10	11	15	4	4	4	4	10	6
40	20	20	14	15	4	4	4	4	10	14
41	10	12	10	16	4	5	4	4	10	10
42	-	19	18	16	1	4	4	4	10	13
43	20	20	20	16	4	5	5	4	1	20
44	20	-	-	16	4	1	1	4	9	18
45	50	45	22	17	4	5	5	5	1	30
46	40	57	-	17	4	5	1	5	10	30
47	15	15	5	18	4	4	4	4	7	6
48	15	29	12	18	4	5	5	5	1	17
49	30	30	10	18	5	5	5	5	1	30
50	40	40	15	18	4	4	4	4	7	12
51	11	11	9	18	4	5	5	5	1	9
52	15	15	17	20	5	5	5	5	1	10
53	15	14	14	20	4	5	5	5	1	11
54	30	40	42	20	4	5	5	5	1+7	25
55	10	8	6	20	4	4	4	5	2	10
56	-	13	9	20	1	4	4	4	10	10
57	30	31	14	20	4	5	4	5	4	13
58	20	25	23	20	5	5	5	5	1	25
59	10	5	10	20	4	4	4	4	10	6
60	30	30	30	21	5	5	5	5	1	22
61	13	25	12	23	4	5	5	4	1	12

Patient no.	CM size [mm]	SM size [mm]	USG size [mm]	MRI size [mm]	BI-RADS CM	BI-RADS SM	BI-RADS USG	BI-RADS MRI	Hist-pat	hispat size [mm]
62	25	33	23	24	5	5	5	5	1	27
63	15	14	8	24	4	4	4	4	10	8
64		71	7	24	4	5	4	4	4	6
65	15	18	15	24	4	5	5	5	1	17
66	33	33	25	24	5	5	5	5	1	25
67	15	23	16	24	4	5	5	5	6	16
68	30	21	20	25	5	5	5	5	1	18
69	12	12	7	25	4	5	4	5	1	12
70	30	20	14	26	5	5	5	5	1	18
71	20	16	15	27	5	5	5	5	1+7	12
72	25	16	8	27	5	5	5	5	1	10
73	15	25	16	27	4	4	4	4	1+7	17
74	30	30	22	28	4	5	5	5	1	20
75		7		28	1	4	1	5	10	12
76	15	16	14	28	4	5	4	4	10	14
77	22	12	5	29	5	5	5	5	2	25
78	15	23	18	30	4	5	5	5	1	19
79	60		47	30	2	1	4	4	10	50
80	-	73	12	30	4	5	5	5	1	20
81	-	30	11	30	4	5	5	5	1	15
82	-	50	26	30	4	5	5	5	1	30
83	-	12	8	30	1	4	4	5	1	8
84	50	18	12	30	4	5	4	5	1	24
85	-	9	9	32	1	5	4	4	10	15
86	14	14	11	34	4	5	4	2	10	10
87	-	-	24	35	4	1	4	2	10	12
88	10	-	-	36	4	1	1	4	10	20
89	11		10	37	4	1	4	4	10	8
90	12	18	13	40	4	5	4	4	10	14
91	-	7	21	40	1	4	4	5	8	1
92	-	17	10	40	1	5	5	5	2	10
93	20	14	20	40	5	5	5	5	2	18
94	-	10	12	41	4	4	4	4	10	10
95	13	13	12	41	4	5	4	4	10	10
96	14	58	-	47	4	5	1	4	7	40
97	-	37	-	54	4	4	1	4	7	20
98	15	15		55	4	4	1	4	10	12
99	20	18	11	60	4	5	5	5	1	9
100	-	-	8	60	1	1	4	4	10	8
101	-	30	30	64	4	5	5	5	1	29
102	25	18	11	74	5	5	5	5	1	25

Patient no.	CM size [mm]	SM size [mm]	USG size [mm]	MRI size [mm]	BI-RADS CM	BI-RADS SM	BI-RADS USG	BI-RADS MRI	Hist-pat	hispat size [mm]
103		9	9	90	1	5	5	5	1	8
104	25	50	32	-	5	5	5	5	1	37
105	25	27	22	-	4	5	4	5	1+7	20
106	25	30	26	-	4	4	4	4	10	24
107	32	36	26	-	4	5	4	4	10	30
108	35	20	12	-	5	5	5	5	1	15
109	63	48	32	-	4	4	4	4	10	10
110	20	15	16	-	4	4	4	4	10	12
111	40	22	20	-	5	5	5	5	1+7	9
112	10	8	10	-	2	4	4	2	10	8
113	17	12	12	-	5	4	4	4	6	12
114	18	18	25	-	4	5	5	4	1	15
115	18	14	14	-	4	5	4	4	2	12
116	35		21	-	4	1	4	2	10	27
117	20	35	23	-	4	5	5	5	1	18
118	9	12	7	-	4	4	4	5	7	10
119	12		10	-	4	1	4	4	10	10
120	20	16	10	-	5	5	5	4	1	16
121		6	-	-	4	4	1	4	10	6
122	20	62	-	-	4	5	1	4	2	24
123		28	-	-	5	5	1	5	7	27
124	22	22	27	-	4	4	2	2	10	25
125		12	30	-	1	4	4	4	10	-
126	63	65	10	-	4	5	5	5	7	21
127	-	5	-	-	1	4	1	4	10	5
128	-	20		-	1	4	1	2	10	-
129	20	22	20	-	5	5	5	5	2	14
130	20	20	12	-	2	6	5	5	1	1
131	-	10	12	18	1	4	4	4	4	10

Bibliography

[1] Paweł Moskal et al. "Test of a single module of the J-PET scanner based on plastic scintillators". In: *Nuclear Instruments and Methods in Physics Research Section A: Accelerators, Spectrometers, Detectors and Associated Equipment* 764 (2014), pp. 317–321.

[2] Paweł Moskal et al. "Time resolution of the plastic scintillator strips with matrix photomultiplier readout for J-PET tomograph". In: *Physics in Medicine & Biology* 61.5 (2016), p. 2025.

[3] Szymon Niedźwiecki et al. "J-PET: a new technology for the whole-body PET imaging". In: *Acta Physica Polnoica B* 48.10 (2017), p. 1567.

[4] Paweł Moskal et al. "Positronium imaging with the novel multiphoton PET scanner". In: *Science advances* 7.42 (2021), eabh4394.

[5] Paweł Moskal et al. "Testing CPT symmetry in ortho-positronium decays with positronium annihilation tomography". In: *Nature communications* 12.1 (2021), p. 5658.

[6] Paweł Moskal and Ewa Stępień. "Prospects and clinical perspectives of total-body PET imaging using plastic scintillators". In: *PET clinics* 15.4 (2020), pp. 439–452.

[7] Paweł Moskal et al. "Simulating NEMA characteristics of the modular total-body J-PET scanner—an economic total-body PET from plastic scintillators". In: *Physics in Medicine & Biology* 66.17 (2021), p. 175015.

[8] Ferlay J et al. "Cancer incidence and mortality worldwide: sources, methods and major patterns in GLOBOCAN 2012". In: *International journal of cancer* 136 (2015), E359–E386.

[9] Servick K. "Breast cancer: a world of differences". In: *Science* 343 (2014), pp. 1452–1453.

[10] Torre LA et al. "Global cancer statistics". In: *CA: a cancer journal for clinicians* 65 (2015), pp. 87–108.

[11] Robert D Rosenberg et al. "Effects of age, breast density, ethnicity, and estrogen replacement therapy on screening mammographic sensitivity and cancer stage at diagnosis: review of 183,134 screening mammograms in Albuquerque, New Mexico." In: *Radiology* 209.2 (1998), pp. 511–518.

[12] Rajul Parikh et al. "Understanding and using sensitivity, specificity and predictive values". In: *Indian journal of ophthalmology* 56.1 (2008), p. 45.

[13] Anne Marie Kavanagh et al. "The sensitivity, specificity, and positive predictive value of screening mammography and symptomatic status". In: *Journal of medical screening* 7.2 (2000), pp. 105–110.

[14] Na Young Sung et al. "Estimating age group-dependent sensitivity and mean sojourn time in colorectal cancer screening". In: *Journal of medical screening* 26.1 (2019), pp. 19–25.

[15] Stefaan Vandenberghe, Pawel Moskal, and Joel S Karp. "State of the art in total body PET". In: *EJNMMI physics* 7 (2020), pp. 1–33.

[16] Shannon B Glass and Zeeshan A Shah. "Clinical utility of positron emission mammography". In: *Baylor University Medical Center Proceedings*. Vol. 26. 3. Taylor & Francis. 2013, pp. 314–319.

[17] Jae Seon Eo et al. "Imaging sensitivity of dedicated positron emission mammography in relation to tumor size". In: *The Breast* 21.1 (2012), pp. 66–71.

[18] Patricia K Ravert and Crystal Huffaker. "Breast cancer screening in women: An integrative literature review". In: *Journal of the American Academy of Nurse Practitioners* 22.12 (2010), pp. 668–673.

[19] Huong T Le-Petross and Mahesh K Shetty. "Magnetic resonance imaging and breast ultrasonography as an adjunct to mammographic screening in high-risk patients". In: *Seminars in Ultrasound, CT and MRI*. Vol. 32. 4. Elsevier. 2011, pp. 266–272.

[20] Mohammad Esmaeil Akbari et al. "Mammography and ultrasonography reports compared with tissue diagnosis-an evidence based study in Iran, 2010". In: *Asian Pacific Journal of Cancer Prevention* 13.5 (2012), pp. 1907–1910.

[21] Rosa Di Micco et al. "PET/MRI for staging the axilla in breast cancer: current evidence and the rationale for SNB vs. PET/MRI trials". In: *Cancers* 13.14 (2021), p. 3571.

[22] Christopher NH Lim et al. "Recent advances in breast cancer diagnosis entering an era of precision medicine". In: *Borneo Journal of Medical Sciences (BJMS)* 13.1 (2019), pp. 3–3.

[23] Khosro Keshavarz et al. "Positron Emission Mammography (PEM) in the diagnosis of breast cancer: A systematic review and economic evaluation". In: *Medical Journal of the Islamic Republic of Iran* 34 (2020), p. 100.

[24] Jerzy Smyrski et al. "Application of WLS strips for position determination in strip PET tomograph based on plastic scintillators". In: *Bio-Algorithms and Med-Systems* 10.2 (2014), pp. 59–63.

[25] J Smyrski et al. "Measurement of gamma quantum interaction point in plastic scintillator with WLS strips". In: *Nuclear Instruments and Methods in Physics Research Section A: Accelerators, Spectrometers, Detectors and Associated Equipment* 851 (2017), pp. 39–42.

[26] Paweł Moskal et al. "Positronium in medicine and biology". In: *Nature Reviews Physics* 1.9 (2019), pp. 527–529.

[27] Dulski et al. "Commissioning of the J-PET detector in view of the positron annihilation lifetime spectroscopy". In: *Hyperfine Interactions* 239.1 (2018), pp. 1–6.

[28] Hyuna Sung et al. "Global cancer statistics 2020: GLOBOCAN estimates of incidence and mortality worldwide for 36 cancers in 185 countries". In: *CA: a cancer journal for clinicians* 71.3 (2021), pp. 209–249.

[29]   *Breast cancer.* https://www.who.int/news-room/fact-sheets/detail/breast-cancer/.

[30]   *Poland Breast cancer cases.* https://gco.iarc.fr/today/data/factsheets/populations/616-poland-fact-sheets.pdf/.

[31]   Mandana Vahabi. "Breast cancer screening methods: a review of the evidence". In: *Health care for women international* 24.9 (2003), pp. 773–793.

[32]   Virginia L Ernster et al. "Detection of ductal carcinoma in situ in women undergoing screening mammography". In: *Journal of the National Cancer Institute* 94.20 (2002), pp. 1546–1554.

[33]   Elzbieta Luczyńska et al. "Comparison of the mammography, contrast-enhanced spectral mammography and ultrasonography in a group of 116 patients". In: *Anticancer research* 36.8 (2016), pp. 4359–4366.

[34]   Sara M Durfee et al. "Sonographic evaluation of clinically palpable breast cancers invisible on mammography". In: *The breast journal* 6.4 (2000), pp. 247–251.

[35]   Thomas G Frazier, J Thomas Murphy, and Ayn Furlong. "The selected use of ultrasound mammography to improve diagnostic accuracy in carcinoma of the breast". In: *Journal of surgical oncology* 29.4 (1985), pp. 231–232.

[36]   Paula B Gordon. "Ultrasound for breast cancer screening and staging". In: *Radiologic Clinics* 40.3 (2002), pp. 431–441.

[37]   Galit Shmueli. "To explain or to predict?" In: *Statistical science* 25.3 (2010), pp. 289–310.

[38]   Kristin L Sainani. "Explanatory versus predictive modeling". In: *PM&R* 6.9 (2014), pp. 841–844.

[39]   Janneke MT Hendriksen et al. "Diagnostic and prognostic prediction models". In: *Journal of Thrombosis and Haemostasis* 11 (2013), pp. 129–141.

[40]   Przemyslaw Biecek and Tomasz Burzykowski. *Explanatory model analysis: explore, explain, and examine predictive models.* CRC Press, 2021.

[41]   Amelia Swift, Roberta Heale, and Alison Twycross. "What are sensitivity and specificity?" In: *Evidence-Based Nursing* 23.1 (2020), pp. 2–4.

[42]   Jacob Yerushalmy. "Statistical problems in assessing methods of medical diagnosis, with special reference to X-ray techniques". In: *Public Health Reports (1896-1970)* (1947), pp. 1432–1449.

[43]   Abdul Ghaaliq Lalkhen and Anthony McCluskey. "Clinical tests: sensitivity and specificity". In: *Continuing education in anaesthesia critical care & pain* 8.6 (2008), pp. 221–223.

[44]   Rajul Parikh et al. "Understanding and using sensitivity, specificity and predictive values". In: *Indian journal of ophthalmology* 56.1 (2008), p. 45.

[45]   Robert Susmaga. "Confusion matrix visualization". In: *Intelligent Information Processing and Web Mining: Proceedings of the International IIS: IIPWM '04 Conference held in Zakopane, Poland, May 17–20, 2004.* Springer. 2004, pp. 107–116.

[46] Sofia Visa et al. "Confusion matrix-based feature selection." In: *Maics* 710.1 (2011), pp. 120–127.

[47] Rajeev Kumar and Abhaya Indrayan. "Receiver operating characteristic (ROC) curve for medical researchers". In: *Indian pediatrics* 48 (2011), pp. 277–287.

[48] Jerome Fan, Suneel Upadhye, and Andrew Worster. "Understanding receiver operating characteristic (ROC) curves". In: *Canadian Journal of Emergency Medicine* 8.1 (2006), pp. 19–20.

[49] Bhavika K Patel et al. "Contrast-enhanced spectral mammography is comparable to MRI in the assessment of residual breast cancer following neoadjuvant systemic therapy". In: *Annals of surgical oncology* 25 (2018), pp. 1350–1356.

[50] Dong Xing et al. "Diagnostic value of contrast-enhanced spectral mammography in comparison to magnetic resonance imaging in breast lesions". In: *Journal of Computer Assisted Tomography* 43.2 (2019), p. 245.

[51] Edward W Lee, Jonathan D Grant, and Carina Mari. "Incidental PET/CT Detection of Breast Cancer in a Patient with Negative Mammogram and Breast Sonogram". In: *Radiology case reports* 2.3 (2007), p. 84.

[52] Chen-Pin Chou et al. "Clinical roles of breast 3T MRI, FDG PET/CT, and breast ultrasound for asymptomatic women with an abnormal screening mammogram". In: *Journal of the Chinese Medical Association* 78.12 (2015), pp. 719–725.

[53] CJ Thompson et al. "Feasibility study for positron emission mammography". In: *Medical physics* 21.4 (1994), pp. 529–538.

[54] Ingo Lütkebohle. *healthcare-in-europe*. https://healthcare-in-europe.com/en/news/europe-s-first-positron-emission-mammography.html/. [Online; accessed 27.02.2012]. 2012.

[55] Irving Weinberg et al. "Preliminary results for positron emission mammography: real-time functional breast imaging in a conventional mammography gantry". In: *European journal of nuclear medicine* 23.7 (1996), pp. 804–806.

[56] Alanah M Bergman et al. "Technique to obtain positron emission mammography images in registration with x-ray mammograms". In: *Medical physics* 25.11 (1998), pp. 2119–2129.

[57] Wendie A Berg et al. "High-resolution fluorodeoxyglucose positron emission tomography with compression ("positron emission mammography") is highly accurate in depicting primary breast cancer". In: *The breast journal* 12.4 (2006), pp. 309–323.

[58] Szymon Niedwiecki. "Studies of detection of γ radiation with use of organic scintillator detectors in view of positron emission tomography". PhD thesis. master thesis, 2011.

[59] Monika Pawlik Niedwiecki. "Studies of changes of signals shapes in plastic scintillator strips". PhD thesis. master thesis, 2014.

[60] Szymon Witold Niedwiecki. "Double-strip prototype of polymer time-of-flight positron emission tomograph based on multi-level analog electronics". PhD thesis. Phd thesis, 2019.

[61] L Kaplon. "Synthesis and Characterization of Polystyrene Scintillators and Their Application in Positron Emission Tomography". PhD thesis. Jagiellonian University Krakow, 2017.

[62] Łukasz Kapłon. "Technical attenuation length measurement of plastic scintillator strips for the total-body J-PET scanner". In: *IEEE Transactions on Nuclear Science* 67.10 (2020), pp. 2286–2289.

[63] J Baran et al. "Comparative studies of plastic scintillator strips with high technical attenuation length for the total-body J-PET scanner". In: *Nuclear Instruments and Methods in Physics Research Section A: Accelerators, Spectrometers, Detectors and Associated Equipment* 1051 (2023), p. 168186.

[64] AP Ivashkin et al. "Scintillation ring hodoscope with WLS fiber readout". In: *Nuclear Instruments and Methods in Physics Research Section A: Accelerators, Spectrometers, Detectors and Associated Equipment* 394.3 (1997), pp. 321–331.

[65] Huini Du, Yongfeng Yang, and Simon R Cherry. "Measurements of wavelength shifting (WLS) fibre readout for a highly multiplexed, depth-encoding PET detector". In: *Physics in Medicine & Biology* 52.9 (2007), p. 2499.

[66] Jiri A Mares et al. "Scintillation Characteristics of the Single-Crystalline Film and Composite Film-Crystal Scintillators Based on the Ce3+-Doped (Lu, Gd) 3 (Ga, Al) 5O12 Mixed Garnets under Alpha and Beta Particles, and Gamma Ray Excitations". In: *Materials* 15.22 (2022), p. 7925.

[67] Syed Naeem Ahmed. *Physics and engineering of radiation detection*. Academic Press, 2007.

[68] Anna Wieczorek. "Development of novel plastic scintillators based on polyvinyltoluene for the hybrid J-PET/MR tomograph". In: *arXiv preprint arXiv:1710.08136* (2017).

[69] Susana Margarida Vieira da Silva. "Study of compton scattering in PET". PhD thesis. 2011.

[70] P Lecoq. "Scintillation detectors for charged particles and photons". In: *Particle Physics Reference Library: Volume 2: Detectors for Particles and Radiation* (2020), pp. 45–89.

[71] S Surti, JS Karp, and G Muehllehner. "Image quality assessment of LaBr3-based whole-body 3D PET scanners: a Monte Carlo evaluation". In: *Physics in Medicine & Biology* 49.19 (2004), p. 4593.

[72] W Chewpraditkul et al. "Scintillation properties of LuAG: Ce, YAG: Ce and LYSO: Ce crystals for gamma-ray detection". In: *IEEE Transactions on Nuclear Science* 56.6 (2009), pp. 3800–3805.

[73] HS Byun. "Radioisotopes and Radiation Methodology Lecture Notes". In: *Med Phys 4R06/6R03* (2016).

[74] Pawel Sibczynski et al. "Characterization of some modern scintillators recommended for use on large fusion facilities in γ-ray spectroscopy and tomographic measurements of γ-emission profiles". In: *Nukleonika* 62.3 (2017), pp. 223–228.

[75] Paul A Cahill. "Toward red-emitting, radiation tolerant chromophores". In: *Radiation Physics and Chemistry* 41.1-2 (1993), pp. 351–363.

[76] Tibor Jacob Hajagos et al. "High-Z sensitized plastic scintillators: a review". In: *Advanced Materials* 30.27 (2018), p. 1706956.

[77] Robley Dunglison Evans and RD Evans. *The atomic nucleus*. Vol. 582. McGraw-Hill New York, 1955.

[78] S Hartmann, D Weidlich, and D Klostermeier. "Single-molecule confocal FRET microscopy to dissect conformational changes in the catalytic cycle of DNA topoisomerases". In: *Methods in enzymology*. Vol. 581. Elsevier, 2016, pp. 317–351.

[79] Carel WE van Eijk. "Inorganic scintillators in medical imaging detectors". In: *Nuclear Instruments and Methods in Physics Research Section A: Accelerators, Spectrometers, Detectors and Associated Equipment* 509.1-3 (2003), pp. 17–25.

[80] Dominique Thers et al. "A proposal for a high performance $\gamma-$camera based on liquid Xenon converter and gaseous photomultiplier for PET". In: *Applications of Rare Gas Xenon to Science And Technology (XeSAT 2005)*. 2005, pp. 1–8.

[81] Glenn F Knoll. *Radiation detection and measurement*. John Wiley & Sons, 2010.

[82] Joao Jose De Lima. *Nuclear medicine physics*. CRC Press, 2016.

[83] Gopal B Saha. *Basics of PET imaging: physics, chemistry, and regulations*. Springer, 2015.

[84] Claude Leroy and Pier-Giorgio Rancoita. *Principles of radiation interaction in matter and detection*. World Scientific, 2011.

[85] L Eriksson et al. "The NEC dependence of different scintillators for positron emission tomography". In: *IEEE Symposium Conference Record Nuclear Science 2004*. Vol. 6. IEEE. 2004, pp. 3785–3788.

[86] S Surti et al. "Investigation of lanthanum scintillators for 3D PET". In: *2002 IEEE Nuclear Science Symposium Conference Record*. Vol. 2. IEEE. 2002, pp. 1177–1181.

[87] Christopher CM Kyba et al. "Timing measurements from a TOF-PET scanner using local PMT triggering". In: *2007 IEEE Nuclear Science Symposium Conference Record*. Vol. 6. IEEE. 2007, pp. 4123–4128.

[88] S Surti, JS Karp, and G Muehllehner. "Image quality assessment of LaBr3-based whole-body 3D PET scanners: a Monte Carlo evaluation". In: *Physics in Medicine & Biology* 49.19 (2004), p. 4593.

[89] R Wojcik et al. "Embedded waveshifting fiber readout of long scintillators". In: *Nuclear Instruments and Methods in Physics Research Section A: Accelerators, Spectrometers, Detectors and Associated Equipment* 342.2-3 (1994), pp. 416–435.

[90] Valery Evdokimov. "Light collection from scintillation counters using WLS fibers and bars". In: *AIP Conference Proceedings*. Vol. 450. 1. American Institute of Physics. 1998, pp. 300–311.

[91] Miquel Nebot. "Development of wavelength shifter coated reflectors for the NEXT experiment". In: *Universitat de València, December* 2 (2011).

[92] Melvin Lax. "The Franck-Condon principle and its application to crystals". In: *The Journal of chemical physics* 20.11 (1952), pp. 1752–1760.

[93] CH Lally et al. "UV quantum efficiencies of organic fluors". In: *Nuclear Instruments and Methods in Physics Research Section B: Beam Interactions with Materials and Atoms* 117.4 (1996), pp. 421–427.

[94] JB Coon, RE DeWames, and CM Loyd. "The Franck-Condon principle and the structures of excited electronic states of molecules". In: *Journal of Molecular Spectroscopy* 8.1-6 (1962), pp. 285–299.

[95] VP Gupta. "Interaction of Radiation and Matter and Electronic Spectra". In: *Principles and Applications of Quantum Chemistry* (2016), pp. 291–337.

[96] Eljen Technology. *BC-482 Wavelength shifter.* https://eljentechnology.com/products/wavelength-shifting-plastics/.

[97] Eljen Technology. *Wavelength shifting plastic.* https://eljentechnology.com/products/wavelength-shifting-plastics/ej-280-ej-282-ej-284-ej-286/.

[98] Wojciech Krzemien et al. "J-PET Framework: Software platform for PET tomography data reconstruction and analysis". In: *SoftwareX* 11 (2020), p. 100487.

[99] *FTAB - combining front-end, TDC and readout into small and compact board.* http://koza.if.uj.edu.pl/jpet-bnct-2018/file/talks/Palka.pdf.

[100] *FTAB - small form factor and versatile board for J-PET detector.* http://koza.if.uj.edu.pl/jpet-bnct-2018/file/talks/Palka.pdf.

[101] M Pałka et al. "Multichannel FPGA based MVT system for high precision time (20 ps RMS) and charge measurement". In: *Journal of Instrumentation* 12.08 (2017), P08001.

[102] Grzegorz Korcyl et al. "Evaluation of single-chip, real-time tomographic data processing on FPGA SoC devices". In: *IEEE transactions on medical imaging* 37.11 (2018), pp. 2526–2535.

[103] Paweł Moskal et al. "A novel method based solely on field programmable gate array (FPGA) units enabling measurement of time and charge of analog signals in positron emission tomography (PET)". In: *Bio-Algorithms and Med-Systems* 10.1 (2014), pp. 41–45.

[104] David Sarrut et al. "The OpenGATE ecosystem for Monte Carlo simulation in medical physics". In: *Physics in Medicine & Biology* (2022).

[105] Michael S Hansen and Peter Kellman. "Image reconstruction: an overview for clinicians". In: *Journal of Magnetic Resonance Imaging* 41.3 (2015), pp. 573–585.

[106] Michel Defrise and Grant T Gullberg. "Image reconstruction". In: *Physics in Medicine & Biology* 51.13 (2006), R139.

[107] Shrinivas D Desai and Linganagouda Kulkarni. "A quantitative comparative study of analytical and iterative reconstruction techniques". In: *International Journal Of Image Processing (IJIP)* 4.4 (2010), p. 307.

[108] Artur Słomski et al. "3D PET image reconstruction based on the maximum likelihood estimation method (MLEM) algorithm". In: *Bio-Algorithms and Med-Systems* 10.1 (2014), pp. 1–7.

[109] Gengsheng Lawrence Zeng. "Image reconstruction—a tutorial". In: *Computerized medical imaging and graphics* 25.2 (2001), pp. 97–103.

[110] Luca Caucci et al. "List-mode MLEM image reconstruction from 3D ML position estimates". In: *IEEE Nuclear Science Symposium & Medical Imaging Conference.* IEEE. 2010, pp. 2643–2647.

[111] Arthur P Dempster, Nan M Laird, and Donald B Rubin. "Maximum likelihood from incomplete data via the EM algorithm". In: *Journal of the royal statistical society: series B (methodological)* 39.1 (1977), pp. 1–22.

[112] Yehuda Vardi, Larry A Shepp, and Linda Kaufman. "A statistical model for positron emission tomography". In: *Journal of the American statistical Association* 80.389 (1985), pp. 8–20.

[113] Thibaut Merlin et al. "CASToR: a generic data organization and processing code framework for multi-modal and multi-dimensional tomographic reconstruction". In: *Physics in Medicine & Biology* 63.18 (2018), p. 185005.

[114] *Development of the innovative positron emission tomography for beam range monitoring in proton radiotherapy.* https://koza.if.uj.edu.pl/petwiki/images/f/ff/PhD_Thesis_Jakub_Baran.pdf.

[115] Robert L Siddon. "Fast calculation of the exact radiological path for a three-dimensional CT array". In: *Medical physics* 12.2 (1985), pp. 252–255.

[116] Steven R Meikle and Ramsey D Badawi. "Quantitative techniques in PET". In: *Positron emission tomography: basic sciences* (2005), pp. 93–126.

[117] Wojciech Krzemień et al. "Analysis framework for the J-PET scanner". In: *Acta Physica Polonica A* 127.5 (2015), p. 1491.

[118] Wojciech Krzemień et al. "J-PET analysis framework for the prototype TOF-PET detector". In: *Bio-Algorithms and Med-Systems* 10.1 (2014), pp. 33–36.

[119] Angela Collarino et al. "Novel frontiers of dedicated molecular imaging in breast cancer diagnosis". In: *Translational cancer research* 7 (2018), S295–S306.

[120] Carrie B Hruska, Amanda L Weinmann, and Michael K O'Connor. "Proof of concept for low-dose molecular breast imaging with a dual-head CZT gamma camera. Part I. Evaluation in phantoms". In: *Medical physics* 39.6Part1 (2012), pp. 3466–3475.

[121] E Albuquerque et al. "An overview of the Clear-PEM breast imaging scanner". In: *2008 IEEE Nuclear Science Symposium Conference Record.* IEEE. 2008, pp. 5616–5618.

[122] Lawrence MacDonald et al. "Clinical imaging characteristics of the positron emission mammography camera: PEM Flex Solo II". In: *Journal of Nuclear Medicine* 50.10 (2009), pp. 1666–1675.

[123] P Lecoq and S Gundacker. "SiPM applications in positron emission tomography: toward ultimate PET time-of-flight resolution". In: *The European Physical Journal Plus* 136.3 (2021), p. 292.

[124] Edward MD Fisher. "Single-photon avalanche diodes in CMOS technologies for optical communications". In: *Optical Communication Technology*. IntechOpen, 2017.

[125] Edoardo Charbon et al. "Design rules for quantum imaging devices: experimental progress using CMOS single-photon detectors". In: *Quantum Communications and Quantum Imaging IV*. Vol. 6305. SPIE. 2006, pp. 133–143.

[126] Koei Yamamoto. "Newly developed semiconductor detectors by Hamamatsu". In: *International Workshop on New Photon-Detectors*. Vol. 51. SISSA Medialab. 2008, p. 004.

[127] K Yamamoto et al. "Development of multi-pixel photon counter (MPPC)". In: *2006 IEEE Nuclear Science Symposium Conference Record*. Vol. 2. IEEE. 2006, pp. 1094–1097.

[128] Amos Kingatua. *Silicon Photomultiplier (SiPM) Structure, Characteristics, and Applications*. https://www.allaboutcircuits.com/technical-articles/silicon-photomultiplier-structure-characteristics-and-applications/. [Online; accessed November 21, 2019]. 2019.

[129] Slawomir Piatek. *SiPM and SPAD*. https://www.hamamatsu.com/content/dam/hamamatsu-photonics/sites/static/hc/resources/SiPM_SPAD_20Emerging_Applications.pdf/.

[130] G Eigen et al. "Gain stabilization of SiPMs with an adaptive power supply". In: *Journal of Instrumentation* 14.05 (2019), P05006.

[131] Wei Jiang, Yamn Chalich, and M Jamal Deen. "Sensors for positron emission tomography applications". In: *Sensors* 19.22 (2019), p. 5019.

[132] Valeri Saveliev. "Silicon photomultiplier-new era of photon detection". In: *Ed. Ki Young Kim, Advances Optical and Photonic Devices: Intech* (2010), pp. 249–272.

[133] ON Semiconductor. *Biasing and Readout of ON Semiconductor SiPM Sensors*.

[134] ON Semiconductor. *Introduction to the silicon photomultiplier (SiPM)*.

[135] Giovanni Maira et al. "Crucial aspects for the use of silicon photomultiplier devices in continuous wave functional near-infrared spectroscopy". In: *Biomedical Optics Express* 9.10 (2018), pp. 4679–4688.